

GLUON FUSION PROCESSES AT ONE-LOOP WITHIN THE STANDARD MODEL AND BEYOND

By

Ambresh Kumar Shivaji

PHYS07200604037

Institute of Physics, Bhubaneswar

A thesis submitted to the

Board of Studies in Physical Sciences

In partial fulfillment of requirements

For the Degree of

DOCTOR OF PHILOSOPHY

of

HOMI BHABHA NATIONAL INSTITUTE



April, 2013

STATEMENT BY AUTHOR

This dissertation has been submitted in partial fulfillment of requirements for an advanced degree at Homi Bhabha National Institute (HBNI) and is deposited in the Library to be made available to borrowers under rules of the HBNI. Brief quotations from this dissertation are allowable without special permission, provided that accurate acknowledgement of source is made. Requests for permission for extended quotation from or reproduction of this manuscript in whole or in part may be granted by the Competent Authority of HBNI when in his or her judgment the proposed use of the material is in the interests of scholarship. In all other instances, however, permission must be obtained from the author.

(Ambresh Kumar Shivaji)

DECLARATION

I, Ambresh Kumar Shivaji, hereby declare that the investigations presented in the thesis have been carried out by me. The matter embodied in the thesis is original and has not been submitted earlier as a whole or in part for a degree/diploma at this or any other Institution/University.

(Ambresh Kumar Shivaji)

To My Brother

ACKNOWLEDGEMENTS

I would like to acknowledge the direct financial support, in the form of my fellowship, from the Department of Atomic Energy, Government of India. The financial support from other funding agencies for attending various schools and conferences in India and abroad, including short academic visits, is also greatly acknowledged. I would also like to thank all the active members of the Indian high energy physics community for continuing the effort of making it one of the most organized research communities in India. Special thanks to the organizers and participants of the *SERC Schools in Theoretical High Energy Physics* which I attended as a beginning graduate student. I should also thank the countable members of Indian RADCOR group for organizing an *Advanced School on Radiative Corrections* and the *RADCOR 2011 Symposium* first time in India and fortunately during my PhD career.

Although Pankaj is my official supervisor, I have always seen him as a good friend and collaborator. I would like to thank him for whatever academic and non-academic support he could provide me in last five years. I wish to thank other supporting members of the Institute also. I have extensively used the small cluster-computing facility of the Institute computer centre. I give special thanks to all those who kept the facility alive during my crucial PhD projects. I have gone through many wonderful experiences during my stay in the campus, and I wish to thank all the people who were responsible for them.

During my PhD career, I have been greatly benefited by interacting with many individuals. I must thank my all such teachers which include friends, professional teachers and professional researchers for showing great patience with me and helping me out in difficult situations. The unconditional love and support of my family members; my parents, my brother, my sisters and their lovely kids have continuously helped in reaching this milestone.

Date:

Ambresh Kumar Shivaji

Contents

Synopsis	ix
List of Publications/Preprints	xiv
List of Figures	xv
List of Tables	xix
1 Introduction	1
1.1 The Standard Model	4
1.2 The ADD Model: An Example of New Physics	10
1.3 Physics at Hadron Colliders	14
2 One-loop Tensor Reduction	17
2.1 Reduction of Standard Three and Four-point Tensor Integrals	20
2.1.1 Projection operators for tensor reduction	20
2.1.2 Passarino-Veltman (PV) reduction	23
2.1.3 Oldenborgh-Vermaseren (OV) reduction	28
2.2 Reduction of Five-point Tensor Integrals	31
2.3 Fermion Loop Amplitudes	33
2.3.1 IR finiteness of fermion loop diagrams	33
2.3.2 Rational terms, Gauge invariance, Anomaly & Decoupling in fermion loop amplitudes	39
3 Gluon-Gluon Contribution to Di-vector Boson + Jet Production	42
3.1 The Amplitudes	44

3.2	Calculation and Numerical Checks	46
3.3	Numerical Results	50
3.3.1	Numerical results for $VV'g$	51
3.3.2	Numerical results for γZg	54
3.4	The Issue of Numerical Instability	58
4	Production of KK-gravitons with a Boson via Gluon Fusion	64
4.1	The Structure of Amplitudes	65
4.2	Details of Calculation and Checks	68
4.3	$gg \rightarrow HG_{\text{KK}}$ Calculation in the Effective theory of Gluon-Higgs coupling	71
4.4	Numerical Results	72
4.5	A Discussion on ZG_{KK} Calculation	76
5	Summary	78
	Appendix A	82
A.1	Units, Conventions, Notations & Definitions	82
A.2	Logs and Di-Logs	85
	Appendix B	88
B.1	Simple analysis of infrared singularities at one-loop	88
B.1.1	Soft singularity	89
B.1.2	Collinear singularity	91
B.1.3	Overlapping regions	92
B.2	One-loop scalar integrals	93
B.3	Derivation of pentagon scalar integral, E_0	98
	Appendix C	101
C.1	Examples of fermion loop triangle amplitudes	101
C.1.1	ggH amplitude; $p_1^2 \neq 0, p_2^2 \neq 0$	101
C.1.2	ggZ amplitude; $p_1^2 \neq 0, p_2^2 \neq 0$	103
C.2	γ^5 in n dimensions	105

Appendix D	107
D.1 Feynman rules	107
Bibliography	110

Synopsis

The *Standard Model* (SM) of particle physics is our present understanding of Nature. It is a framework in which properties and behavior of the fundamental particles and forces can be studied. It offers a unified description of the electromagnetic and weak forces along with the strong force in the microscopic domain. At the fundamental level, these forces act among *quarks* and *leptons* (the matter particles) through *gauge bosons* (the mediator particles). The model has been remarkably successful in explaining a huge amount of data collected so far at various high energy particle collider experiments throughout the world. Despite its success, there are direct as well as indirect evidences which indicate that the SM cannot be a complete story of the Universe. It does not include the fourth force of Nature, the Gravity. It does not account correctly for the dominance of matter over antimatter as observed in the Universe. It does not have any suitable candidate for the proposed *Dark matter* particles.

Apart from these direct evidences, there are certain theoretical inconsistencies associated with the model. It predicts the existence of a fundamental scalar, the *Higgs boson* as a result of the *electroweak symmetry breaking* (EWSB) through the SU(2) doublet of scalar fields. The recent discovery of a fundamental boson ($\simeq 125$ GeV) at the *Large Hadron Collider* (LHC) experiments might confirm the existence of this last missing piece of the SM particle jungle soon. Within the model, the quantum correction to the Higgs mass is not stable; it is quadratically divergent and requires a very fine tuning of parameters. This is known as a *fine tuning* or *naturalness problem* in the literature. Another problem, more of a philosophical nature and closely related to the naturalness problem, is the unexplained hierarchy between the electroweak symmetry breaking scale (~ 100 GeV) and the fundamental scale of Gravity

in 4 dimensions, the *Planck scale* ($\sim 10^{19}$ GeV). The desirable unification of the fundamental forces is also not feasible within the model. All these lead us to believe that the SM is only a low energy description of a deeper reality. We expect new physics and new particles to appear at higher energy scales (\sim TeV), where the SM predictions are not yet tested.

There are many candidates for new physics, with their own merits and demerits, which address many of the above mentioned problems. Models based on *supersymmetry*, models of *new forces* and models of *extra dimensions* are few among many. Their predictions can be tested at the present day high energy colliders such as the LHC and this requires calculations to be done in both the SM and new physics models. Any deviation from the SM predictions is a signature of new physics. The problem of large hierarchy between the electroweak and the Planck scales can be addressed within the models of extra space dimensions. Among various models of extra dimensions, the ADD model of large extra dimensions is one of the very first successful attempts in this direction. In the ADD model, the number of space-time dimensions is taken $4 + \delta$. The SM degrees of freedom live on a $(3 + 1)$ -dimensional *brane*, while the Gravity can access the full $4 + \delta$ dimensions. The extra space dimensions are supposed to be compact. In this model, the 4-dimensional Planck scale is only an effective scale and the fundamental scale of Gravity, M_S can be near TeV scale. In $4 + \delta$ dimensions, the $4 + \delta$ dimensional graviton appears as an infinite tower of *Kaluza-Klein* (KK) modes and it couples to the energy-momentum tensor ($\mathcal{T}_{\mu\nu}$) of the SM fields. The direct production of the KK-gravitons gives rise to missing energy signals in the detector.

At *hadron colliders* the fundamental interactions take place among its constituents, the quarks and the gluons. Collectively these are called *partons* and they carry a certain momentum fraction of the parent hadron. Although the coupling of the strong interaction (α_s) acting among the partons is quite large at low energies, due to the property of *asymptotic freedom* it is possible to apply perturbative methods at the parton level at higher energies. The *color confinement* forces the partons not to be seen as free particles and therefore, perturbative calculations at the parton level may appear meaningless. The *factorization theorem* provides a means to calculate

hadronic cross sections in terms of partonic ones. Predictions obtained this way have been verified at the hadron colliders such as the *Tevatron* and the LHC. The $p\bar{p}$ collider facility at the Tevatron has been recently shutdown. The LHC is a *proton-proton* collider with the centre-of-mass (c.m.) energy in the multi-TeV range. It is presently running at 8 TeV c.m. energy and more than $10fb^{-1}$ of data has been collected so far at the two general purpose detectors, the ATLAS (*A Toroidal LHC Apparatus*) and the CMS (*Compact Muon Solenoid*). At higher energies the gluon distribution functions are quite important, and therefore, gluon fusion processes can contribute significantly towards the SM as well as new physics predictions.

In this thesis, I have studied certain gluon fusion processes at the hadron colliders. We have considered the *di-vector boson production in association with a jet via gluon fusion* within the SM. We have also considered *the direct production of the KK-gravitons in association with a boson via gluon fusion* in the ADD model. All these processes share a common feature that they proceed via the *quark loop diagrams* at the leading order (LO) itself and being LO contributions these are expected to be finite. Total cross sections and phenomenologically relevant kinematic distributions constitute the main results of these studies. The amplitude calculation is done at the parton level. One of the most difficult parts of the calculation is the reduction of one-loop *tensor integrals* into a suitable set of one-loop *scalar integrals*. In our projects, we have one-loop five-point tensor integrals of rank five as the most complicated tensor structures. We have worked with two different codes for the one-loop tensor reduction in n dimensions. An analytical tensor reduction code in FORM was developed during the ADD model projects. It is based on the reduction method suggested by Denner-Dittmaier, and the reduction of any one-loop tensor integral up to four-rank, four-point function can be performed using it. We have used it successfully in our ADD model projects to make various checks on amplitudes. For actual numerical calculations we have used a numerical code written in FORTRAN following the one-loop tensor reduction method of Oldenborgh-Vermaseren. Any one-loop amplitude in 4 dimensions, after the tensor reduction, can be expressed in terms of the scalar integrals of *box*, *triangle*, *bubble* and *tadpole* types and an additional piece called the *Rational part*. Thus the singularity structure of any one-loop amplitude is dictated

by those of the scalar integrals. The rational part is an artifact of the regularization of *ultra-violet* (UV) divergences of one-loop tensor integrals. We have derived the one-loop scalar integrals, required in this thesis, following the method of 't Hooft-Veltman. UV singularities are regularized in $4 - 2\epsilon$ dimensions while *infra-red* (IR) singularities are regularized by giving a small mass to the quarks in the loop. Due to the numerical instability these scalar integrals are used only for making finiteness checks on amplitudes. Actual numerical results are obtained using the scalar integrals from the LoopTools and the OneLOop packages.

In the ADD model, the process $gg \rightarrow BG_{KK}$ contributes to $pp \rightarrow BG_{KK} + X$ at the next-to-leading order (NLO) in α_s . These processes proceed via quark loop diagrams of the triangle and the box types. We work with all the six quark flavors and except the top quark all others are treated as massless. We find that the amplitude for $gg \rightarrow \gamma G_{KK}$ vanishes at the LO. This can be shown using *Furry's Theorem* and the charge conjugation property of the graviton. Due to the same reason the vector part of the $gg \rightarrow ZG_{KK}$ amplitude does not contribute. Since the axial part of the amplitude is proportional to the T_q^3 value, it does not receive any contribution from the first two generations. We find that due to the nature of the graviton coupling with the quarks, both the triangle and box diagrams are linearly divergent and give rise to the *anomaly*. We have studied the intricate relationship between the anomaly and the rational terms in linearly divergent fermion loop amplitudes. We find that in fermion loop amplitudes (including those plagued with the chiral anomaly), correct rational terms can be obtained utilizing the *Decoupling theorem*. The process $gg \rightarrow HG_{KK}$ receives dominant contribution from the top quark in the loop. It is a leading non-zero contribution to $pp \rightarrow HG_{KK} + X$, if we neglect the bottom quark mass. In all these cases, we have studied the variation of the total cross section with respect to the collider c.m. energy. We observe a significant cancellation between the triangle and the box contributions at the amplitude level. We find that at the typical LHC energy the cross section is only few fb. We give the transverse momentum (p_T) and the rapidity (η) distributions of the bosons (Z/H) and examine the effect of changing the *renormalization* and the *factorization* scales. In the direct production processes of the KK-gravitons, all the kinematically allowed modes are produced and

therefore we also discuss their distribution. We have studied changes in our results as the ADD model parameters δ and M_S are varied. We have also checked the effect of choosing different sets of the *parton distribution functions* (PDFs).

In the SM, the process $gg \rightarrow VV'g$ contributes to $pp \rightarrow VV'j + X$ at the next-to-next-to-leading order in α_s . Like the corresponding di-vector boson production cases, these are important backgrounds to the Higgs boson production as well as new physics scenarios. In particular, we have considered the production of $\gamma\gamma g$, γZg , ZZg and W^+W^-g at the LHC. The process $gg \rightarrow \gamma\gamma g$ has been calculated in the past. We have updated its cross section and have reconfirmed the importance of this processes at the LHC. In the ZZg and W^+W^-g cases, we have ignored the Higgs boson interference effects. These proceed via the quark loop diagrams of the box and the pentagon types. The box diagrams give only the vector contribution while the pentagon diagrams give both the vector and the axial-vector contributions. We work in the limit of the decoupling of the top quark. We have studied the variation of the hadronic cross section with respect to the collider c.m. energy for all the four processes. We find that these one-loop contributions are in the range of 4 – 15% of the corresponding tree-level contributions. We also give some important kinematic distributions common to all the four processes.

In a more complete study of the γZg production process, we explicitly check the decoupling of the top quark at the amplitude level as well as at the level of the total cross section. We have quantified the contributions of the vector and the axial-vector parts of the amplitude towards the total cross section. We also study the effects of changing the renormalization and the factorization scales and the effect of choosing the PDF sets. We have considered the decay of the Z boson, and a comparison with the corresponding LO and NLO calculation is also made. We briefly discuss the method adopted to deal with the numerical instabilities in our calculations.

List of Publications/Preprints

1. Simple Analysis of IR Singularities at One-Loop, [A. Shivaji](#), arXiv:1008.4375 [hep-ph].
2. IR Finiteness of Fermion Loop Diagrams, [A. Shivaji](#), arXiv:1008.4792 [hep-ph].
3. [‡] Associated Production of a KK-graviton with a Higgs Boson via Gluon Fusion at the LHC, [A. Shivaji](#), S. Mitra and P. Agrawal, Eur. Phys. J. C 72, 1922 (2012)
4. [‡] Production of a KK-graviton and a Vector Boson in ADD Model via Gluon Fusion, [A. Shivaji](#), V. Ravindran and P. Agrawal, JHEP 1202, 057 (2012)
5. [‡] Di-vector Boson + Jet Production via Gluon Fusion at Hadron Colliders, P. Agrawal and [A. Shivaji](#), Phys. Rev. D 86, 073013 (2012)
6. [‡] Production of γZg and associated processes via gluon fusion at hadron colliders, P. Agrawal and [A. Shivaji](#), JHEP 1301, 071 (2013)

Conference Proceedings

1. Production of a KK-graviton in association with a boson via gluon fusion at the LHC, S. Mitra, [A. Shivaji](#) and P. Agrawal, PoS RADCOR 2011, 045 (2011)
2. Multi Vector Boson Production via Gluon Fusion at the LHC, P. Agrawal and [A. Shivaji](#), PoS RADCOR 2011, 010 (2011)
3. Multi-Vector Boson Production via Gluon-Gluon Fusion, P. Agrawal and [A. Shivaji](#), PLHC 2012, To be published in SLAC econf system

A ([‡]) indicates papers on which this thesis is based.

List of Figures

1.1	Running of QCD coupling with the scale.	15
1.2	Parton Distribution Functions of quark and gluon.	15
1.3	Gluon Distribution Functions at LO and NLO.	16
1.4	Gluon Distribution Functions at various scales.	16
2.1	Standard one-loop scalar integrals.	18
2.2	Massless fermion loop diagram. Dotted external lines represent any suitable massless particle.	34
2.3	Feynman rules: (a) scalar-fermion-fermion vertex (b) vector boson- fermion-fermion vertex (c) graviton-fermion-fermion vertex	35
2.4	Interaction of 4 scalars in the Yukawa theory of scalars and fermions.	38
3.1	The prototype diagrams for the processes $gg \rightarrow VV'g$. The wavy lines represent the appropriate combination of the γ , Z or W boson. The last two classes (c) and (d) are relevant to WWg production only. We do not consider diagrams involving Higgs boson for the ZZg and WWg cases.	44
3.2	Ward identities for $gg \rightarrow \gamma\gamma g$ pentagon and box diagrams. All the momenta are taken incoming. The dotted lines take care of momentum insertion at relevant vertices.	47
3.3	Decoupling of the top quark in $gg \rightarrow \gamma Zg$ amplitude. The vector and axial-vector contributions are shown separately.	50
3.4	Variation of the cross sections with the collider centre-of-mass energy for $gg \rightarrow VV'g$	51

3.5	Variation of the cross sections with the collider centre-of-mass energy for $gg \rightarrow VV'$	51
3.6	Invariant mass distributions of the pair of vector boson at 8 TeV, for $gg \rightarrow VV'g$	52
3.7	Transverse momentum distributions of the gluon jet at 8 TeV, for $gg \rightarrow VV'g$	52
3.8	The collider energy dependence of the cross section for $gg \rightarrow \gamma\gamma g$. . .	53
3.9	Transverse momentum distributions of the photon in $gg \rightarrow \gamma\gamma g$	53
3.10	Transverse momentum distribution of the gluon jet in $gg \rightarrow \gamma\gamma g$. . .	54
3.11	Invariant mass distribution of the two photons in $gg \rightarrow \gamma\gamma g$	54
3.12	Decoupling of the top quark in the cross section calculation of $gg \rightarrow \gamma Zg$. .	55
3.13	The vector and axial-vector contributions of the hadronic cross section for $gg \rightarrow \gamma Zg$	61
3.14	Contribution of the box-amplitude towards the hadronic cross section for $gg \rightarrow \gamma Zg$	61
3.15	Variation of the cross section for $gg \rightarrow \gamma Zg$ with the scale, $\mu = \mu_r = \mu_f$ at 14 TeV.	61
3.16	Dependence of the cross section on the collider energy, for $gg \rightarrow \gamma Z(\rightarrow l^+l^-)g$	61
3.17	Transverse momentum distribution of the photon at 8 TeV centre-of-mass energy in $gg \rightarrow \gamma Z(\rightarrow l^+l^-)g$	62
3.18	Rapidity distribution of the photon at 8 TeV centre-of-mass energy in $gg \rightarrow \gamma Z(\rightarrow l^+l^-)g$	62
3.19	Transverse momentum distribution of the gluon jet at 8 TeV centre-of-mass energy in $gg \rightarrow \gamma Z(\rightarrow l^+l^-)g$	62
3.20	Rapidity distribution of the gluon jet at 8 TeV centre-of-mass energy in $gg \rightarrow \gamma Z(\rightarrow l^+l^-)g$	62
3.21	Transverse momentum distribution of lepton at 8 TeV centre-of-mass energy in $gg \rightarrow \gamma Z(\rightarrow l^+l^-)g$	63
3.22	Rapidity distribution of lepton at 8 TeV centre-of-mass energy in $gg \rightarrow \gamma Z(\rightarrow l^+l^-)g$	63

3.23	A comparison of the normalized p_T -distributions of γ at NLO and NNLO. The NLO distribution is obtained using MCFM.	63
3.24	Dependence of the total cross section on GI test cut-parameter (δ) for $gg \rightarrow \gamma\gamma g$ at 14 TeV. The error bars are shown explicitly.	63
4.1	Prototype Feynman diagrams for $gg \rightarrow H/\gamma/Z + G_{KK}$ in the ADD model.	66
4.2	Decoupling of the top quark as $m_t \rightarrow \infty$, in $gg \rightarrow ZG_{KK}$	70
4.3	Non-decoupling of the top quark as $m_t \rightarrow \infty$, in $gg \rightarrow HG_{KK}$	70
4.4	Feynman diagrams for $gg \rightarrow HG_{KK}$ in the heavy top quark limit.	71
4.5	Collider energy dependence of the hadronic cross sections for $gg \rightarrow H/ZG_{KK}$ at the LHC.	73
4.6	Dependence of the cross sections on the number of extra dimensions δ , for the scale $M_S = 2$ TeV.	73
4.7	Dependence of the cross sections on the scale M_S , for the number of extra dimension $\delta = 2$	73
4.8	Transverse momentum distribution of the Higgs boson for $M_S = 2$ TeV and $\delta = 2$	74
4.9	Transverse momentum distribution of the Z boson for $M_S = 2$ TeV and $\delta = 2$	74
4.10	KK-graviton mass distribution in HG_{KK} case, for $M_S = 2$ TeV and $\delta = 2$	75
4.11	KK-graviton mass distribution in ZG_{KK} case, for $M_S = 2$ TeV and $\delta = 2$	75
4.12	A comparison of $gg \rightarrow HG_{KK}$ cross sections calculated in full theory and in the effective theory.	76
B.1	General scalar one-loop diagram with momentum assignment	89
B.2	One-loop correction to QED vertex	90
C.1	Feynman diagrams for $gg \rightarrow H/Z$. The dashed line may represent the Higgs boson or the Z boson. The 4-vector index ρ is applicable in the $gg \rightarrow Z$ case only.	101

D.1	Feynman rules for 3-point vertices in the ADD model. The zig-zag line denotes the KK-graviton. The dashed line is for the Higgs boson while the curly line may denote any gauge boson with mass M_A . $\kappa = \sqrt{16\pi G_N} = \sqrt{2}/M_P$, and ξ is the gauge-fixing parameter.	108
D.2	Feynman rules for some of the 4-point vertices in the ADD model. The Yukawa coupling, $y_f = \frac{1}{2}g_w(m_f/M_W)$. The last vertex is derived in an effective theory of ggH coupling.	109

List of Tables

1.1	Quantum numbers of leptons and quarks of the first generation. The Y value of fields is decided using the Gell-Mann–Nishijima relation, $Q = T^3 + Y$. This relation naturally arises in the theory. Each quark field is threefold degenerate in electroweak interactions due to its color content.	6
3.1	Cross sections for the production of $pp \rightarrow \gamma Z j + X$ at various collider centre-of-mass energies. We use CTEQ6l1 PDF set at the LO and CTEQ6M PDF set at the NLO. The NNLO predictions are with CTEQ6l1(CTEQ6M) parton distribution. The factorization and renormalization scales are set to, $\mu_f = \mu_r = \mu_0 = M_Z$	57

Chapter 1

Introduction

It is an exciting period for all of us who have been looking beyond the well established fundamental laws of Nature. Our current understanding of fundamental particles and their interactions is dubbed as the Standard Model (SM) of particle physics. In the past four decades or so, its predictions have been tested time and again in a wide-variety of experiments, and the model has become a paradigm. However, the story does not end here. We now know that the SM, despite its success, does not address many of the important issues about which we have become aware over the years. We do not have a satisfactory quantum theory of Gravity, the fourth fundamental force of Nature. Although the SM has ingredients to generate matter-antimatter asymmetry, the amount of asymmetry predicted by it does not explain the asymmetry observed in the Universe. We know that the SM particle spectrum describes only 4 % of the Universe. Investigating the nature of dark matter and dark energy, which make up 96 % of the Universe, remains a big challenge. Few experimental measurements like the forward-backward asymmetry of the top quark pair production at the Tevatron, and the muon $g - 2$ measurement at the BNL, seem to be inconsistent with the SM calculations [1, 2]. The well known hierarchy between the Planck scale and the scale of electroweak symmetry breaking also seeks a natural explanation. All these and many other issues suggest the existence of new physics beyond the SM. There have been many proposals such as supersymmetric models, extra-dimensional models and models of grand unification to address some of these questions, but their confirmation can come only from the experiments. For a review on the topics related to the SM

and possible new physics, one may refer to [3].

The discovery of new physics (a signal) is always complemented by the knowledge of known physics (the background). Every new discovery in an experiment becomes a background for future experiments. To find a signal, a precise knowledge of the background is essential. The Tevatron, a proton-antiproton collider at the Fermilab, was in service for almost 28 years before it was shut down on September 30, 2011. It has tested and refined the SM through many fundamental discoveries and measurements, such as the discovery of the top quark, the observation of direct CP violation in the decay of neutral kaons, the direct observation of the tau neutrino, precision measurements of weak interaction parameters, the observation of single top quark production and the discovery of many mesons and baryons [4]. It also played a crucial role in narrowing down the mass range for the SM Higgs boson, discovery of which is expected to be confirmed soon at the Large Hadron Collider (LHC) [5]. The collider delivered more than 10 fb^{-1} of data before going for a full stop. The data analysis will keep experimentalists engaged for several years. After the Tevatron, in a collider type experiment, the LHC is the next big step in achieving the goal of testing the SM predictions at higher energies and uncovering new physics.

The LHC, a proton-proton collider at CERN, seems to have achieved a lot within a short span of its ongoing career. It is a fact of amusement and amazement that the whole SM of particle physics was rediscovered at the LHC within a year of its full operation [6]. Very recently, the discovery of a Higgs-like particle at both the general purpose LHC experiments, the CMS and the ATLAS, was announced [7–9]. It is believed that this Higgs-like particle could be the very Higgs boson of the SM. Further analysis is going on in this direction. Before the discovery of this Higgs-like particle, the observation of a new quarkonium state and the observation of a new bottom baryon was also reported [10, 11]. Although their discovery is not as crucial as that of the Higgs boson, their existence and measured properties are definitely consistent with our beloved SM. So far, we do not have a conclusive evidence of any new physics [12–15]. However, with ever growing data and its ongoing analysis, a large parameter space in many potential candidates of new physics, has already been ruled out.

At the LHC, two beams of protons are collided with an unprecedented amount of

energy. At present the collider is operating at 8 TeV centre-of-mass energy. Future plans to upgrade it to 14 TeV and beyond are already under considerations. The proton is a composite particle and at very high energy it can be seen as a collection of quarks, antiquarks and gluons. For a given set of final state particles, any process at the proton-proton collider may proceed through various channels like quark-quark, quark-gluon and gluon-gluon channels. Due to the possibility of a large gluon flux at high energy hadron colliders, we have considered a specific class of processes which are initiated by the gluon-gluon channel. We have divided our study of gluon fusion processes into two parts – the background processes and the signal processes. We have considered di-vector boson and a jet production via gluon fusion within the SM. These processes have never been seen earlier, so it will be a test for the SM itself. They may have significant cross sections at the LHC and therefore are important backgrounds to the Higgs boson and many new physics signals. We have also considered the gluon-gluon contribution to the associated production of an electroweak boson with the KK-gravitons in the ADD (Arkani-Hamed, Dimopoulos and Dvali) model. The model offers an explanation to the SM hierarchy problem. All these gluon fusion processes proceed via quark loop diagrams at the leading order (LO). Unlike in the case of radiative corrections to a tree-level process, there is no issue of renormalization/factorization because these LO one-loop processes are finite. However, the calculation of multiparticle one-loop amplitudes itself is quite difficult. Although the method of calculating one-loop amplitudes has evolved quite a lot lately, we have taken the traditional route of one-loop tensor reduction to calculate them. In addition, the fermion loop amplitudes, due to their special properties, provide a unique opportunity to understand the structure of one-loop amplitudes in general.

This thesis is organized as follows. Within this chapter, in the next few sections we will give a brief overview of the Standard Model and the ADD model. We will also argue that the gluon fusion processes at high energy hadron colliders are important. In chapter 2, we will describe the general structure of one-loop amplitudes using the methods of tensor reduction. Some special properties of fermion loop amplitudes will also be discussed. The production of a pair of electroweak vector bosons in association with a jet via gluon fusion will be studied in chapter 3. We will present the cross section calculations and important kinematic distributions at the LHC. Next,

in chapter 4, we will consider the associated production of an electroweak boson and KK-gravitons via gluon fusion at the LHC. The dependence of cross sections and various kinematic distributions on the ADD model parameters will also be studied. We will summarize the thesis in chapter 5. Many complementary topics are included in the appendix.

1.1 The Standard Model

The SM is a renormalizable local quantum field theory, based on the gauge group $SU(2)_L \times U(1)_Y \times SU(3)_c$. It is a gauge theory meaning that the allowed interactions among fundamental particles are fixed by demanding the invariance of the free field Lagrangian under the local gauge transformation of fields [16, 17]. The (spin-1/2) matter particles, leptons and quarks, live in the fundamental representation while the (spin-1) mediator particles, gauge bosons, live in the adjoint representation of the gauge groups. The $SU(2)_L \times U(1)_Y$ component of the SM can be considered a unified description of the electromagnetic and weak interactions. The electroweak classical Lagrangian consistent with the local gauge invariance is given by

$$\mathcal{L}_{EW} = -\frac{1}{4}(W_{\mu\nu}^a)^2 - \frac{1}{4}(B_{\mu\nu})^2 + i\bar{\psi}\not{D}\psi, \quad (1.1)$$

where the field strength tensor of the $SU(2)$ gauge fields $W_\mu^a(x)$ ($a = 1, 2, 3$) and that of the $U(1)_Y$ gauge field $B_\mu(x)$ are

$$W_{\mu\nu}^a = \partial_\mu W_\nu^a - \partial_\nu W_\mu^a + g_w \varepsilon^{abc} W_\mu^b W_\nu^c, \quad (1.2)$$

$$B_{\mu\nu} = \partial_\mu B_\nu - \partial_\nu B_\mu. \quad (1.3)$$

Here g_w is the $SU(2)$ gauge coupling parameter. Physical fields of the electroweak interaction are linear combinations of the above fields,

$$W_\mu^\pm = \frac{1}{\sqrt{2}}(W_\mu^1 \mp iW_\mu^2), \quad (1.4)$$

$$\begin{pmatrix} Z_\mu \\ A_\mu \end{pmatrix} = \begin{pmatrix} \cos\theta_w & -\sin\theta_w \\ \sin\theta_w & \cos\theta_w \end{pmatrix} \begin{pmatrix} W_\mu^3 \\ B_\mu \end{pmatrix}. \quad (1.5)$$

The angle θ_w is known as the *weak mixing angle* and it is defined by

$$\cos\theta_w = \frac{g_w}{\sqrt{g_w^2 + g'^2}}, \quad \sin\theta_w = \frac{g'}{\sqrt{g_w^2 + g'^2}}, \quad (1.6)$$

where g' is the $U(1)_Y$ gauge coupling parameter. Though all the gauge fields are massless at this stage, their triple and quartic couplings are already present in the Lagrangian; a hallmark of non-Abelian gauge theories. The coupling of the fermions with the gauge bosons is defined through the covariant derivative,

$$D_\mu \equiv \partial_\mu - ig_w W_\mu^a T^a - ig' B_\mu Y \quad (1.7)$$

$$= \partial_\mu - i \frac{g_w}{\sqrt{2}} (W_\mu^+ T^+ + W_\mu^- T^-) - i \frac{g_w}{\cos\theta_w} Z_\mu (T^3 - \sin^2\theta_w Q) - ie A_\mu Q, \quad (1.8)$$

$$\text{with } T^\pm = T^1 \pm iT^2, \quad Q = T^3 + Y \quad \text{and} \quad e = g_w \sin\theta_w = g' \cos\theta_w. \quad (1.9)$$

Q and e are the charge and the coupling parameter of the electromagnetic interaction, respectively. Y is the $U(1)_Y$ charge called the *hypercharge*. The $\{T^a\}$ are the generators of the $SU(2)$ gauge group and their algebra is given by,

$$[T^a, T^b] = i\epsilon^{abc} T^c \quad \text{and} \quad [T^a, Y] = 0. \quad (1.10)$$

In Eq. 1.7, these generators appear in the fundamental representation. We see here that all the couplings of the electroweak vector bosons are described by two parameters, e and θ_w . However, a shift from the set $\{g_w, g'\} \rightarrow \{e, \theta_w\}$, does not imply true unification of the weak and the electromagnetic interactions. Existence of the Z boson, and therefore the existence of weak neutral currents was a very successful prediction of the model. The fact that weak interactions differentiate left and right-handed fermions, is implemented in the theory by grouping left-handed fermions into $SU(2)$ doublets and taking right-handed fermions as $SU(2)$ singlets. That explains the subscript ' L ' in the $SU(2)_L$. For the first generation of fermions, the ψ field in Eq. 1.1, represents the following set of fermion fields:

$$\begin{pmatrix} \nu_e \\ e \end{pmatrix}_L, \quad e_R, \quad \begin{pmatrix} u \\ d \end{pmatrix}_L, \quad u_R, \quad d_R.$$

Quantum numbers of these fermion fields are shown in Table 1.1. There are two more copies of the above set in the SM and all of them have been observed experimentally. Fermions of the first generation are sufficient for this brief introduction. Due to historical reasons, the ν_{eR} field is not included in the above set.

It is clear that mass terms for both the gauge bosons and fermions violate gauge invariance. But in Nature, we do see massive fermions and massive gauge bosons

of weak interaction. This implies that the electroweak symmetry must be broken to meet the reality. In the standard electroweak model, this symmetry breaking is achieved by introducing a $SU(2)$ doublet of complex scalar fields with $Y = 1/2$,

$$\Phi(x) = \begin{pmatrix} \phi^+(x) \\ \phi^0(x) \end{pmatrix}. \quad (1.11)$$

The idea here is to couple the complex scalar doublet with the gauge fields and

Fermions	T^3	Y	Q
ν_{eL}	$+\frac{1}{2}$	$-\frac{1}{2}$	0
e_L	$-\frac{1}{2}$	$-\frac{1}{2}$	-1
e_R	0	-1	-1
u_L	$+\frac{1}{2}$	$+\frac{1}{6}$	$+\frac{2}{3}$
d_L	$-\frac{1}{2}$	$+\frac{1}{6}$	$-\frac{1}{3}$
u_R	0	$+\frac{2}{3}$	$+\frac{2}{3}$
d_R	0	$-\frac{1}{3}$	$-\frac{1}{3}$

Table 1.1: Quantum numbers of leptons and quarks of the first generation. The Y value of fields is decided using the Gell-Mann–Nishijima relation, $Q = T^3 + Y$. This relation naturally arises in the theory. Each quark field is threefold degenerate in electroweak interactions due to its color content.

with the fermions in a gauge invariant manner. The scalar doublet couples with the gauge fields through the covariant derivative given in Eq. 1.7, and it couples with the fermion fields through Yukawa interactions,

$$\mathcal{L}_{scalar} = |D_\mu \Phi|^2 - V(\Phi) - y_d \bar{\psi}_L \cdot \Phi \psi_R - y_u \bar{\psi}_L \cdot \tilde{\Phi} \psi_R + h.c., \quad (1.12)$$

$$V(\Phi) = -\mu^2(\Phi^\dagger \Phi) + \lambda(\Phi^\dagger \Phi)^2, \quad (1.13)$$

$$\text{and } \tilde{\Phi} = i\sigma_2 \Phi^\dagger = \begin{pmatrix} \phi^0 \\ -\phi^- \end{pmatrix}. \quad (1.14)$$

ψ_L and ψ_R represent, respectively, the set of doublets and singlets of fermion fields introduced above. Only gauge invariant combinations of these fields can appear in

Eq. 1.12. y_u and y_d are Yukawa couplings and they are related to the upper and lower components of the left-handed fermion doublets. In Eq. 1.14, σ_2 is a Pauli matrix. Note that, no new coupling parameter is introduced for the interaction of scalars with the gauge bosons. The first term in the Lagrangian includes gauge invariant terms, quadratic in gauge fields and coupled with the scalar doublet. Now the electroweak symmetry is broken spontaneously in the scalar sector, which then propagates into the gauge and fermion sector through its couplings with them, by giving a non-zero vacuum expectation value to the scalar doublet, *i.e.*,

$$\langle \Phi \rangle_0 = \frac{1}{\sqrt{2}} \begin{pmatrix} 0 \\ v \end{pmatrix}. \quad (1.15)$$

Here $v = \sqrt{\mu^2/\lambda}$ is obtained by minimizing the scalar potential in Eq. 1.13, provided $\lambda, \mu^2 > 0$. A comparison with the effective theory of weak interactions at low energy implies $v = (G_F \sqrt{2})^{-1/2} \simeq 246$ GeV, G_F being the Fermi constant. Remember that the μ^2 -term in the potential is not the mass term as it appears with the incorrect sign in the Lagrangian. As a result of the spontaneous symmetry breaking, the quadratic gauge field terms become the mass term of the corresponding gauge bosons and the fermions become massive through the Yukawa terms. The masses of the electroweak bosons and fermions, in this model, are given by

$$M_W = g_w \frac{v}{2}, \quad M_Z = \sqrt{g_w^2 + g'^2} \frac{v}{2} = \frac{M_W}{\cos \theta_w}, \quad (1.16)$$

$$M_\gamma = 0 \quad \text{and} \quad m_f = \lambda_f \frac{v}{\sqrt{2}}. \quad (1.17)$$

Taking the experimental inputs for v and θ_w ($\sin \theta_w \simeq 0.23$), the correct masses for the W^\pm and Z bosons were predicted by the model. On the other hand, fermion masses are parameterized in terms of unknown Yukawa couplings. The observed hierarchy of fermion masses does not find a natural explanation in this model. The above mechanism of mass generation for fermions and gauge bosons is known as the *Higgs mechanism* [18–23]. The fact that the photon remains massless implies that the subgroup $U(1)_{em}$ is unbroken. Note that neutrinos are massless in the SM as defined above. The neutrino oscillation experiments suggest that neutrinos are massive, however, whether they are Dirac particles or Majorana particles is not yet clear [3, 24, 25]. In the SM, a Dirac mass term for neutrinos can be generated via Higgs mechanism by introducing a ν_{eR} field.

Since the true vacuum is defined by a non-zero expectation value, we must reparametrize the complex scalar doublet taken in Eq. 1.11. In the *unitary gauge*, there are no unphysical degrees of freedom and the scalar doublet can be taken as

$$\Phi(x) = \frac{1}{\sqrt{2}} \begin{pmatrix} 0 \\ v + H(x) \end{pmatrix}. \quad (1.18)$$

The real scalar field $H(x)$, also called the Higgs field, is the only physical scalar field left after the symmetry breaking has taken place. The other three real scalar fields of the scalar doublet are the goldstone bosons resulting from the spontaneous symmetry breaking. They provide longitudinal degrees of freedom to weak bosons making them massive. Replacing $\Phi(x)$ in Eq. 1.12 with the above choice, we not only generate masses of various fields as described above, we also obtain interactions of the Higgs field with the gauge and fermion fields. The scalar potential contains the Higgs boson mass term, with the mass given by

$$M_H = \sqrt{2\mu^2} = \sqrt{2\lambda} v, \quad (1.19)$$

along with its self interactions. The SM does not provide any direct information on the value of M_H because the parameter μ^2 of the scalar potential is *a priori* unknown. Direct search experiments and various theoretical studies advocate a light Higgs boson [3]. The recent discovery of a fundamental boson at the LHC, in the mass range 125-126 GeV, might confirm this last missing piece of the SM [8,9]. The electroweak model of $SU(2)_L \times U(1)_Y$ gauge group supplemented with the spontaneous electroweak symmetry breaking, through a complex scalar doublet, is also known as the Glashow-Weinberg-Salam (GWS) model [26–28]. The renormalizability of the GWS model was proved by 't Hooft [29].

The SM does not put any constraint on the number of fermion generations n_g , but to avoid *anomalies* (violation of gauge symmetries of classical Lagrangian due to quantum effects), it does require that the number of quark generations must be equal to the number of lepton generations. Introduction of more than one generation of fermions in the model leads to the mixing of fields in the quark sector. This is related to the fact that weak interaction eigenstates are different from the mass eigenstates. If the number of fermion generations is greater than two, which is the case in the SM

($n_g = 3$), CP violation can occur in weak interactions [30]. A very small CP violation (1 part in 1000) has been observed in kaon and B-meson decays [3, 31]. CP violation is necessary to explain the matter-antimatter asymmetry in the Universe, but the amount of CP violation present in the SM is not enough to quantify the observed asymmetry. A primer on the electroweak sector of the SM can be found in Ref. [32].

The $SU(3)_c$ sector of the SM represents the strong interaction among colored fields, the quarks and the gluons. Leptons are immune to the color force. The interactions of quarks and gluons are governed by the classical Lagrangian

$$\mathcal{L}_{QCD} = -\frac{1}{4}(G_{\mu\nu}^a)^2 + \bar{q}_i(i\not{D} - m_q)_{ij}q_j, \quad (1.20)$$

where the field strength of massless gluon fields G_{μ}^a ($a = 1 \rightarrow 8$), and the covariant derivative acting on the quark fields q_i ($i = 1, 2, 3$), are

$$G_{\mu\nu}^a = \partial_{\mu}G_{\nu}^a - \partial_{\nu}G_{\mu}^a + g_s f^{abc}G_{\mu}^b G_{\nu}^c, \quad (1.21)$$

$$(D_{\mu})_{ij} = \delta_{ij}\partial_{\mu} - ig_s G_{\mu}^a t_{ij}^a. \quad (1.22)$$

Here g_s is the coupling parameter of the strong interaction and f^{abc} are the structure constants of the $SU(3)$ group. The generators $\{t^a\}$ of the group satisfy, $[t^a, t^b] = if^{abc} t^c$. In Eq. 1.22, they are in the fundamental representation. Like the photon in QED, gluons – the force carriers of the strong interaction, remain massless due to the local gauge invariance. On the other hand, the quark mass term is gauge invariant. Unlike the photon, the gluons are charged under the gauge group and they interact among themselves. The quantization of massless gauge field theories also require a gauge-fixing term in the Lagrangian [33]. It is not possible to define the propagator for massless gauge fields without making a gauge choice. A class of covariant gauges can be introduced in Eq. 1.20, to fix the gauge

$$\mathcal{L}_{GF} = -\frac{1}{2\xi}(\partial^{\mu}G_{\mu}^a)^2, \quad (1.23)$$

where ξ is the gauge-fixing parameter. In non-Abelian massless gauge theories, to cancel the effects of the unphysical timelike and longitudinal polarization states of the gauge bosons, the covariant gauge-fixing term must be supplemented with the

Faddeev-Popov ghost Lagrangian

$$\mathcal{L}_{FP} = \bar{\eta}^a (-\partial^\mu D_\mu^{ab}) \eta^b, \quad (1.24)$$

$$\text{with } (D_\mu)^{ab} = \delta^{ab} \partial_\mu - g f^{abc} G_\mu^c. \quad (1.25)$$

The ghost fields η^a are complex scalar fields which obey Fermi-Dirac statistics. Independence of physical amplitudes on the gauge-fixing parameter ξ , provides a powerful check on calculations. For practical reasons, the gauge fixing principle is also useful in the quantization of electroweak Lagrangian.

An essential feature of a renormalizable QFT is the scale dependence of parameters of the theory. The scale variation of coupling parameter $\alpha_s = g_s^2/4\pi$, is determined by the renormalization group equation [34, 35],

$$Q^2 \frac{\partial}{\partial Q^2} \alpha_s(Q^2) = \beta(\alpha_s). \quad (1.26)$$

The β function has a perturbative expansion in α_s

$$\beta(\alpha_s) = -\alpha_s^2 (b_0 + b_1 \alpha_s + b_2 \alpha_s^2 + \dots), \quad (1.27)$$

where b_i is the $(i+1)$ -loop contribution to the β function. At one-loop, the solution to the renormalization group equation is

$$\alpha_s(Q^2) = \frac{\alpha_s(\mu_r^2)}{1 + b_0 \alpha_s(\mu_r^2) \ln(Q^2/\mu_r^2)}, \quad (1.28)$$

where μ_r is the renormalization scale and $b_0 = (33 - 2n_f)/12\pi$ with n_f , the number of light quark flavours. For $n_f < 16$, $b_0 > 0$ and therefore, unlike QED, in QCD the coupling parameter decreases with increasing Q . This is the property of *asymptotic freedom* which makes perturbative methods useful in strong interactions at high energy [36, 37]. The fact that isolated quarks and gluons are not observed and the only finite energy asymptotic states of the theory are color singlets, is known as *color confinement*. This can be seen as a consequence of the growth of the coupling at low Q ($\lesssim 1$ GeV). A formal discussion on perturbative QCD can be found in Refs. [38, 39].

1.2 The ADD Model: An Example of New Physics

The SM of particle physics, although very successful, is conceptually incomplete. In absence of any new physics, the most fundamental scale in Nature is the 4-dimensional

Planck scale, $M_P (= \frac{1}{\sqrt{8\pi G_N}}) \sim 10^{19}$ GeV. It is the scale around which the quantum effects of 4-dimensional Gravity can no longer be ignored. On the other hand, the electroweak symmetry breaking required to generate masses for fermions and gauge bosons takes place at the scale of about 246 GeV. In the SM, the unexplained hierarchy between the electroweak scale and the 4-dimensional Planck scale is considered unnatural. The evolution of gauge couplings of the SM at higher energy scales ($\sim 10^{16}$ GeV) provides a hint of a true unification (in the sense of a single coupling parameter) of strong, weak and electromagnetic interactions. This scale, also known as the *Grand Unification* scale, may be considered a natural scale of new physics but it does not resolve the hierarchy problem. The Higgs boson mass is not stable against the quantum corrections. Unlike fermions and gauge bosons, the Higgs boson mass is not protected by any symmetry present in the SM. The one-loop quantum correction to the Higgs mass is quadratically divergent and therefore, it strongly depends on the new physics scale. Provided there is no new physics scale between the electroweak and the Grand Unification scales, the Higgs boson mass cannot be kept low (around the electroweak symmetry breaking scale) naturally. In other words, for a stable and natural mass of the SM Higgs boson, a very fine tuning of various parameters in the theory would be required. This is known as the *naturalness* or *fine tuning* problem of the SM. These, so to speak problems of the SM, are central to many beyond the SM physics proposals [40]. Various studies suggest that any new physics beyond the SM might be operative around TeV scale. The LHC is fully capable of testing the SM predictions very accurately at the TeV scale; therefore, it can find out signatures of possible new physics.

There are many models of new physics which have been proposed in the last 30 years, and they come with their own set of pros and cons. Supersymmetric models and extra-dimensional models are among many which have been studied extensively in the literature [3]. Both the supersymmetry and the extra space dimensions are important ingredients in the construction of the String theory, a promising theory of the quantum Gravity. In the supersymmetric models, the quadratic divergence of the Higgs mass is smoothened by introducing a symmetry between fermions and bosons. In models of extra dimensions, Gravity plays a direct role in fixing the TeV scale physics. In this thesis, we will consider a particular model of large extra dimensions,

as an example of new physics scenario beyond the SM.

The problem of large hierarchy between the electroweak and Planck scales can be addressed within the models of extra space dimensions. Among various models of extra dimensions the model of *large* extra dimensions, proposed by Arkani-Hamed, Dimopoulos and Dvali (ADD), is one of the very first successful attempts in this direction [41–44]¹. The predictions of this model can be probed at present day high energy colliders. In the ADD model, the number of space-time dimensions is assumed to be $4 + \delta$. The SM degrees of freedom live on a $(3 + 1)$ -dimensional brane, while Gravity is allowed to propagate in full $4 + \delta$ dimensions. To avoid any direct conflict with the present day observations, these extra dimensions are assumed to be compact. For simplicity, we consider compactification of these extra dimensions on a δ -dimensional torus (T^δ) with radius $R/2\pi$. The space is thus factorized meaning that the 4-dimensional part of the metric does not depend on the extra-dimensional coordinates. We assume that the energy density on the brane does not affect the space-time curvature and the extra space dimensions are flat. The fundamental scale of Gravity M_S , *i.e.*, the $(4+\delta)$ -dimensional Planck scale is related to the 4-dimensional Planck scale by,

$$M_P^2 \approx M_S^{\delta+2} R^\delta. \quad (1.29)$$

From this relation one can argue that if R (in general the volume of the compact extra dimensions, V_δ) is large enough, the fundamental scale of Gravity in $4 + \delta$ dimensions can be as small as few TeV. The ADD model thus resolves the hierarchy problem of the SM by proposing the fundamental scale of Gravity in the TeV range. However, it introduces another hierarchy (unexplained within the model) between the scale for the size of the extra dimensions ($1/R$) and the fundamental scale of Gravity (M_S).

¹Another very popular model of extra dimensions, in the context of the SM hierarchy problem, is the model of *warped* extra dimensions, first proposed by Randall and Sundrum (RS) [45]. The model considers 5-dimensional space-time where the fifth dimension is curved. In this model, the size of the extra dimension can be very small and the fundamental scale of Gravity (the 5-dimensional Planck scale) can be close to the 4-dimensional Planck scale. Warping of the fifth dimension plays the trick of resolving the hierarchy problem. For a review on various other models of extra dimensions, one may refer to [46].

Even then it stands as a good phenomenological model to study. In 4 dimensions, the $(4+\delta)$ -dimensional graviton appears as an infinite tower of KK-modes which includes one spin-2 state, $(n-1)$ spin-1 states and $n(n-1)/2$ spin-0 states. All these states are mass-degenerate and mass of the n^{th} mode is given by,

$$m_{\vec{n}}^2 = \frac{4\pi^2 \vec{n}^2}{R^2}. \quad (1.30)$$

This mass spectrum is cutoff at the scale M_S . The $\vec{n} = 0$ mode corresponds to the 4-dimensional massless graviton, $U(1)$ gauge bosons and scalars. The vector KK-modes ($A_{\mu i}^{\vec{n}}$) decouple from the theory and the scalar KK-modes ($\phi_{ij}^{\vec{n}}$) couple through their trace. In this thesis, we are interested in the interaction of KK-gravitons. The interaction of spin-2 component of these KK-modes ($h_{\mu\nu}^{(\vec{n})}$) with the SM is given by an effective Lagrangian

$$\mathcal{L}_{int} \sim \frac{1}{M_P} \sum_{\vec{n}} h_{\mu\nu}^{(\vec{n})}(x) T^{\mu\nu}(x), \quad (1.31)$$

where $T^{\mu\nu}$ is the energy-momentum tensor for the SM fields. M_S plays the role of an ultraviolet (UV) cutoff of the effective theory. The Feynman rules of the model are derived in [47, 48]. We have followed Han et al. [48] and the ADD model Feynman rules, required in this thesis, are listed in the appendix D.1.

The collider signatures of the model can be studied by looking at processes in which KK-gravitons may appear as virtual states, or they may be produced directly in the final state [47]. In this thesis, we will be interested in the direct production of KK-gravitons. The effective interaction in Eq. 1.31, suggests that the coupling of a single KK-graviton with the SM particles is suppressed by the 4-dimensional Planck scale. In the direct production processes, all the kinematically allowed KK-modes are produced and their contributions should be added up to obtain the inclusive cross sections. Since each KK-graviton mode is degenerate and the mass separation between modes is very small ($\sim 1/R$), we can work in the continuum limit to sum the contributions of kinematically allowed KK-modes. In the continuum limit, the inclusive cross section is

$$\sigma = \int dm \rho(m) \frac{d\sigma_m}{dm}. \quad (1.32)$$

Here $\rho(m)$ is the density of KK states and it is given by,

$$\rho(m) = 2 \frac{R^\delta m^{\delta-1}}{(4\pi)^{\delta/2} \Gamma(\delta/2)}. \quad (1.33)$$

From Eqs. 1.29 and 1.33, we can see that although the cross section for the production of a single KK-graviton (σ_m) is proportional to $1/M_P^2$, the inclusive cross section, obtained by summing over all KK-mode contributions, is only $1/M_S^{\delta+2}$ suppressed. Thus, if M_S is in the TeV range, it can have observable effects at the LHC. Since the coupling of each KK-mode with the SM particles is very small, the direct production of KK-gravitons gives rise to missing energy signal in the detector. More details on the model and its phenomenology can be found in [47–49].

1.3 Physics at Hadron Colliders

High energy particle colliders are powerful microscopes which help us in revealing the secrets of Nature at the very small length scales ($\sim 10^{-19}$ m). We have come a long way since the first collider ADA (*Anello Di Accumulazione*) collided e^+ and e^- beams at 500 MeV centre-of-mass energy and recorded single photon production². We have already entered into an era of multi-TeV hadron colliders such as the Tevatron and the LHC, and have seen some of the very important discoveries in particle physics in recent times.

Deep inelastic lepton-hadron scatterings, performed at SLAC³ and HERA⁴, did confirm the parton model picture of hadrons [50]. According to the parton model, hadrons are composite objects and they are made up of partons, the quarks and the gluons. At hadron colliders, the fundamental interactions take place among these partons and they carry a certain momentum fraction of the parent hadron. The coupling of the strong interaction, $\alpha_s(Q^2)$ is quite large at hadronic mass scales. However, due to the property of *asymptotic freedom*, it is possible to apply perturbative methods at the parton level at higher energies. In Fig. 1.1, we can see the running of the strong coupling parameter with the scale of interaction at the LO and the next-to-leading order (NLO). In hadronic collisions, the partons undergo many soft subprocesses (processes involving low momentum transfer) before reaching the interaction point of a hard scattering. These subprocesses do affect the cross section predictions but they cannot be calculated perturbatively due to a large $\alpha_s(Q^2)$ value at low Q . These

²<http://www.lnf.infn.it/acceleratori/ada/>

³Stanford Linear Accelerator Center

⁴Hadron Electron Ring Accelerator

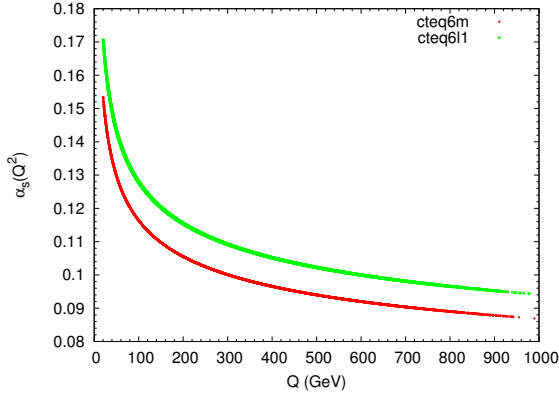


Figure 1.1: Running of QCD coupling with the scale.

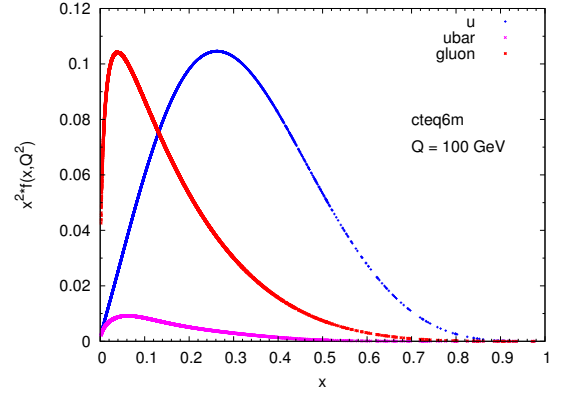


Figure 1.2: Parton Distribution Functions of quark and gluon.

contributions can be factorized into parton distribution functions (PDFs) at the level of cross section. Hadronic cross sections can be obtained in terms of partonic ones using the *factorization theorem* to all orders in perturbation theory [51]. At the LHC for a $2 \rightarrow n$ process, the hadronic cross section is given by

$$\sigma(p + p \rightarrow k_1 + k_2 + \dots + k_n + X) = \int_0^1 dx_1 dx_2 \sum_{a,b} f_a(x_1, Q^2) \times f_b(x_2, Q^2) \times \hat{\sigma}(a + b \rightarrow k_1 + k_2 + \dots + k_n; Q^2). \quad (1.34)$$

The quantity $f_{a/b}(x, Q^2)$, known as a parton distribution function (PDF), defines the probability that the parton ‘ a/b ’ inside a proton carries a momentum fraction x . The scale dependence in the partonic cross section ($\hat{\sigma}$) may enter through higher order corrections due to the renormalization of the ultraviolet singularities and/or due to the factorization of the collinear singularities. The scale dependence of the parton distribution function is a prediction of perturbative QCD and it has been verified, experimentally. The parton distribution functions contain the information on the soft/nonperturbative part of the hadronic interaction and they are universal. Although they cannot be calculated from the first principle, their evolution with the scale is governed by the perturbative QCD. Their evolution equation, known as the *Dokshitzer-Gribov-Lipatov-Altarelli-Parisi* (DGLAP) equation, is analogous to the QCD β function [52, 53].

In this thesis, we will be interested in gluon-gluon initiated processes at hadron colliders. In Fig. 1.2, we have plotted quark and gluon distribution functions at

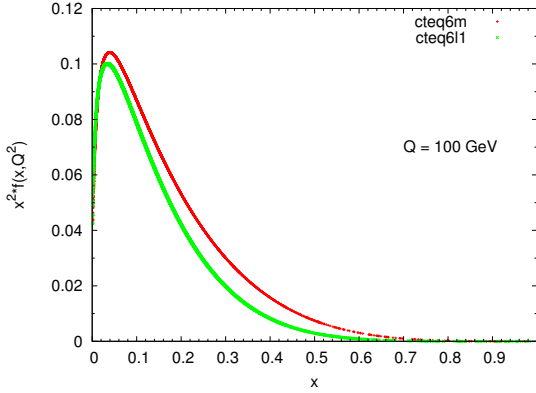


Figure 1.3: Gluon Distribution Functions at LO and NLO.

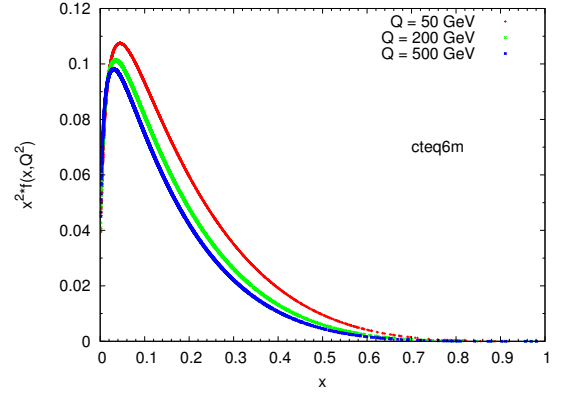


Figure 1.4: Gluon Distribution Functions at various scales.

$Q = 100$ GeV using the CTEQ6M PDF set. Note that we have multiplied the distributions by the momentum fraction squared to reduce the large variation. It can be seen that the gluon distribution function dominates over the quark distribution function in the low- x region. As the collider centre-of-mass energy increases, partons with smaller x values may also contribute towards a physical process. Therefore, at the hadron collider such as the LHC, the gluon-gluon fusion processes are quite important. The amplitudes of gluon fusion processes considered in this thesis are finite, therefore, no renormalization and/or factorization procedure is required. Thus the scale dependence in the cross section predictions enters only through the QCD coupling parameter, $\alpha_s(Q^2)$ and the PDFs, $f_a(x, Q^2)$. In Fig. 1.3, we have plotted the gluon distributions at the LO and NLO using CTEQ6L1 and CTEQ6M PDF sets. The scale dependence of gluon distributions can be seen in Fig. 1.4. A comprehensive introduction of particle phenomenology at hadron colliders can be referred to [53–55].

Chapter 2

One-loop Tensor Reduction

We will now describe the reduction of one-loop tensor integrals, a very important ingredient in the calculation of any one-loop amplitude. Calculation of scattering amplitudes at one-loop level involves *ill-defined* integration over loop momentum. The simplest example of loop integrals appear in ϕ^3 -theory. These are called *scalar integrals*. Depending upon the number of propagators in the loop, these integrals can be classified into various classes. Basic one-loop scalar integrals are shown in Fig. 2.1¹. Following the nomenclature of 't Hooft and Veltman [57], these integrals are

$$A_0 \equiv I_0^1(m_0) = (\mu^2)^{2-n/2} \int \frac{d^n l}{(2\pi)^n} \frac{1}{d_0}, \quad (2.1)$$

$$B_0 \equiv I_0^2(p_1; m_0, m_1) = (\mu^2)^{2-n/2} \int \frac{d^n l}{(2\pi)^n} \frac{1}{d_0 d_1}, \quad (2.2)$$

$$C_0 \equiv I_0^3(p_1, p_2; m_0, m_1, m_2) = (\mu^2)^{2-n/2} \int \frac{d^n l}{(2\pi)^n} \frac{1}{d_0 d_1 d_2}, \quad (2.3)$$

$$D_0 \equiv I_0^4(p_1, p_2, p_3; m_0, m_1, m_2, m_3) = (\mu^2)^{2-n/2} \int \frac{d^n l}{(2\pi)^n} \frac{1}{d_0 d_1 d_2 d_3}. \quad (2.4)$$

Here, $d_i = (l + q_i)^2 - m_i^2 + i\epsilon$ with $q_i = \sum_{j=1}^i p_j$ and $q_0 = 0$. We take all the external momenta as incoming. We have introduced a mass scale μ to keep the natural mass-dimension of scalar integrals intact in n dimensions. Hereafter, we will not show this scale dependence explicitly in n -dimensional loop integrals. In this thesis, we will be

¹ In this thesis, all the Feynman diagrams are drawn using Jaxodraw package [56].

interested in one-loop diagrams with all internal lines of equal masses, *i.e.*, $m_i^2 = m^2$.

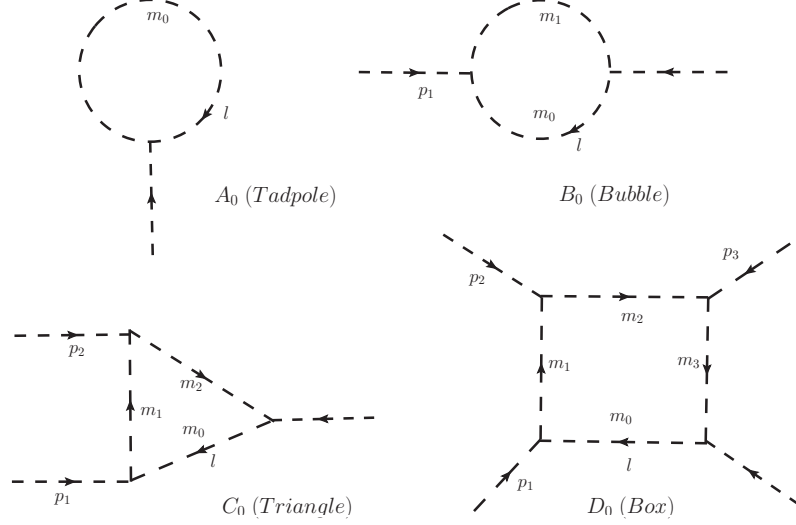


Figure 2.1: Standard one-loop scalar integrals.

Thus, a general N -point scalar integral will have N such denominators. In 4 dimensions, any $N \geq 5$ -point scalar integral can be always written in terms of box scalar integrals. In particular, a 5-point (pentagon) scalar integral can be reduced to a sum of five box scalar integrals [58–60],

$$E_0 = \sum_{i=0}^4 c_i D_0(i), \quad (2.5)$$

where $D_0(i)$ is the box scalar integral obtained after removing the i^{th} propagator in E_0 . This derivation is included in the appendix B.3. These scalar integrals are well known in the literature [61]. We have derived all the scalar integrals for the case of massless internal lines, required in this thesis, using the method of 't Hooft and Veltman [57], and they are listed in the appendix B.2.

In gauge theories, one generally comes across loop integrals with loop momentum appearing in the numerator. These are called *tensor integrals*. To set our notation, we write down an N -point tensor integral of rank- m ,

$$I_{\mu_1, \mu_2, \dots, \mu_m}^N(p_1, \dots, p_{N-1}; m_0, \dots, m_{N-1}) = \int \frac{d^n l}{(2\pi)^n} \frac{l_{\mu_1} l_{\mu_2} \dots l_{\mu_m}}{d_0 d_1 d_2 \dots d_{N-1}}. \quad (2.6)$$

In renormalizable gauge theories, $m \leq N$. Tensor integrals can also be evaluated in the manner of scalar integrals. However, with increasing power of loop momentum in the numerator, the straightforward evaluation of tensor integrals is not very appealing. A systematic approach towards the reduction of tensor integrals into the scalar integrals was presented by Passarion and Veltman (PV) [62]. It is based on writing down the most general tensor structure possible using the set of external momenta $\{p_i\}$ and the metric tensor $g_{\mu\nu}$. For example, the two-point (bubble) tensor integrals of the rank one and two, which appear in the self-energy correction to photon, are given by

$$B_\mu = p_\mu B_1, \quad (2.7)$$

$$B_{\mu\nu} = g_{\mu\nu} B_{00} + p_\mu p_\nu B_{11}. \quad (2.8)$$

The tensor coefficients B_1, B_{00} and B_{11} can be written in terms of the tadpole and bubble scalar integrals. For the case of $p^2 \neq 0$,

$$B_1 = -\frac{1}{2} B_0, \quad (2.9)$$

$$B_{00} = \frac{1}{(n-1)} \left[\frac{1}{2} A_0(0) + m^2 B_0 + \frac{1}{2} p^2 B_1 \right], \quad (2.10)$$

$$B_{11} = \frac{1}{p^2} \left[\frac{(n-2)}{2(n-1)} A_0(0) - \frac{1}{(n-1)} m^2 B_0 - \frac{n}{2(n-1)} p^2 B_1 \right]. \quad (2.11)$$

Here $A_0(0)$ is obtained from B_0 , dropping the d_0 propagator. We will use this *missing propagator notation* extensively, in the reduction of tensor integrals. Except for the special case of $m^2 = 0$, the above expression for B_{11} cannot be used if $p^2=0$. In that case, we can evaluate the integral separately and the result is,

$$B_{\mu\nu}(p^2 = 0; m^2) = \left[\frac{1}{(n-2)} m^2 g_{\mu\nu} + \frac{1}{3} p_\mu p_\nu \right] B_0(p^2 = 0; m^2). \quad (2.12)$$

The reduction of higher point and higher rank tensor integrals can be carried out in a similar manner. Note that we have performed this reduction in n dimensions. The reduction can of course be done in 4 dimensions, but then one has to be very careful in shifting the loop momentum in UV divergent integrals. In linearly (or worse) divergent loop integrals, any shift in the loop momentum leads to a finite contribution. It is convenient, therefore, to perform the reduction in $n = 4 - 2\epsilon$ dimensions. A detailed discussion on the reduction of higher point tensor integrals

is given in the next section. The upshot is that any one-loop amplitude, regularized properly in 4 dimensions, can be written in the basis of tadpole, bubble, triangle and box scalar integrals, *i.e.*,

$$\mathcal{M}^{1-loop} = \sum_i (d_i D_0^i) + \sum_i (c_i C_0^i) + \sum_i (b_i B_0^i) + \sum_i (a_i A_0^i) + \mathcal{R}. \quad (2.13)$$

In this equation, \mathcal{R} is known as the *rational part* and it is an artifact of the UV regularization of tensor integrals. It is clear from the above relation that singularities of one-loop amplitudes are encoded in a set of basic scalar integrals. In this thesis, numerical results are presented using a FORTRAN implementation of the tensor reduction method developed by Oldenborgh and Vermaseren (OV) [63]. We have also implemented an analytic PV reduction of tensor integrals in FORM [64], following Denner and Dittmaier [65]. The analytic reduction code has been extremely useful in understanding the structure of one-loop amplitudes. We have used it to make various checks on our amplitudes in the ADD model projects. In recent times, there have been many new developments in the direction of one-loop calculations. A good review on the subject of one-loop calculations can be found in Ref. [66].

2.1 Reduction of Standard Three and Four-point Tensor Integrals

In this section, we will describe important features of the two reduction methods that we have worked with in our projects. Before considering the actual reduction of tensor integrals we would like to construct some useful objects and study their properties.

2.1.1 Projection operators for tensor reduction

For given two linearly independent vectors p_1 and p_2 , we can always construct their *dual vectors* v_1 and v_2 such that,

$$v_i \cdot p_j = \delta_{ij}. \quad (2.14)$$

Clearly, v_i s are linear combinations of p_1 and p_2 . Let $v_1^\mu = a p_1^\mu + b p_2^\mu$, then the coefficients a and b can be obtained by solving the following matrix equation,

$$\begin{pmatrix} 1 \\ 0 \end{pmatrix} = \begin{pmatrix} p_1 \cdot p_1 & p_1 \cdot p_2 \\ p_1 \cdot p_2 & p_2 \cdot p_2 \end{pmatrix} \begin{pmatrix} a \\ b \end{pmatrix}. \quad (2.15)$$

The 2×2 symmetric matrix on the right hand side is known as the *Gram matrix* of p_1 and p_2 and we will denote it by $X_2[p_1, p_2]$. The solution for a and b , and therefore the existence of v_1 is related to the existence of the inverse of the Gram matrix. For that, the determinant of the Gram matrix, *i.e.*, the *Gram determinant* $\Delta_2(p_1, p_2)$, should not vanish and this will always be the case as long as p_1 and p_2 are linearly independent. The inverse of the Gram matrix of p_1 and p_2 is given by

$$X_2^{-1}[p_1, p_2] = \frac{1}{\Delta_2(p_1, p_2)} \begin{pmatrix} p_2 \cdot p_2 & -p_1 \cdot p_2 \\ -p_1 \cdot p_2 & p_1 \cdot p_1 \end{pmatrix}, \quad (2.16)$$

with, $\Delta_2 = p_1^2 p_2^2 - (p_1 \cdot p_2)^2$. Solving for a and b we get,

$$v_1^\mu = \frac{p_2 \cdot p_2}{\Delta_2} p_1^\mu - \frac{p_1 \cdot p_2}{\Delta_2} p_2^\mu = \delta_{p_1 p_2}^{\mu p_2} / \Delta_2. \quad (2.17)$$

Here we have introduced the *generalized Kronecker delta notation* given in [58]. In this notation,

$$\begin{aligned} \delta_{\nu_1 \nu_2}^{\mu_1 \mu_2} &= \begin{vmatrix} \delta_{\nu_1}^{\mu_1} & \delta_{\nu_2}^{\mu_1} \\ \delta_{\nu_1}^{\mu_2} & \delta_{\nu_2}^{\mu_2} \end{vmatrix} \\ \text{and } \delta_{q_1 q_2}^{p_1 p_2} &= \delta_{\nu_1 \nu_2}^{\mu_1 \mu_2} p_{1\mu_1} p_{2\mu_2} q_1^{\nu_1} q_2^{\nu_2}. \end{aligned} \quad (2.18)$$

Therefore, the Gram determinant $\Delta_2 = \delta_{p_1 p_2}^{p_1 p_2}$. Similarly we can write,

$$v_2^\mu = -\frac{p_1 \cdot p_2}{\Delta_2} p_1^\mu + \frac{p_1 \cdot p_1}{\Delta_2} p_2^\mu = \delta_{p_1 p_2}^{p_1 \mu} / \Delta_2. \quad (2.19)$$

Note that the inverse of the Gram matrix of p_1 and p_2 , shown in Eq. 2.16, is the Gram matrix of v_1 and v_2 , *i.e.*,

$$X_2^{-1}[p_1, p_2] = X_2[v_1, v_2]. \quad (2.20)$$

This analysis can now easily be extended for constructing the duals of three and four linearly independent vectors. For three linearly independent vectors p_1, p_2 and p_3 , the duals are

$$v_1^\mu = \delta_{p_1 p_2 p_3}^{\mu p_2 p_3} / \Delta_3, \quad v_2^\mu = \delta_{p_1 p_2 p_3}^{p_1 \mu p_3} / \Delta_3 \quad \text{and} \quad v_3^\mu = \delta_{p_1 p_2 p_3}^{p_1 p_2 \mu} / \Delta_3, \quad (2.21)$$

with, $\Delta_3 = \delta_{p_1 p_2 p_3}^{p_1 p_2 p_3}$. In the case of four linearly independent vectors p_1, p_2, p_3 and p_4 , the duals are

$$\begin{aligned} v_1^\mu &= \delta_{p_1 p_2 p_3 p_4}^{\mu p_2 p_3 p_4} / \Delta_4, \quad v_2^\mu = \delta_{p_1 p_2 p_3 p_4}^{p_1 \mu p_3 p_4} / \Delta_4, \\ v_3^\mu &= \delta_{p_1 p_2 p_3 p_4}^{p_1 p_2 \mu p_4} / \Delta_4 \text{ and } v_4^\mu = \delta_{p_1 p_2 p_3 p_4}^{p_1 p_2 p_3 \mu} / \Delta_4, \end{aligned} \quad (2.22)$$

with, $\Delta_4 = \delta_{p_1 p_2 p_3 p_4}^{p_1 p_2 p_3 p_4}$. In general, we have

$$v_i^\mu = \sum_j (v_i \cdot v_j) p_j^\mu \text{ and } p_i^\mu = \sum_j (p_i \cdot p_j) v_j^\mu \quad (2.23)$$

$$\Rightarrow \delta_{ik} = \sum_j (v_i \cdot v_j) (p_j \cdot p_k). \quad (2.24)$$

In integer space-time dimensions where we can define the antisymmetric ε -tensors, these dual vectors can be rewritten using,

$$\delta_{q_1 q_2 \dots q_m}^{p_1 p_2 \dots p_m} = \varepsilon^{p_1 p_2 \dots p_m} \varepsilon_{q_1 q_2 \dots q_m}. \quad (2.25)$$

For example, in the case of two linearly independent vectors p_1 and p_2 , the dual vectors become

$$v_1^\mu = \frac{\varepsilon^{\mu p_2}}{\varepsilon^{p_1 p_2}} \text{ and } v_2^\mu = \frac{\varepsilon^{p_1 \mu}}{\varepsilon^{p_1 p_2}}. \quad (2.26)$$

In the context of one-loop tensor reduction, the set of dual vectors is known as *van Neerven-Vermaseren basis vectors*. To regulate the UV singularity of tensor integrals, we will be carrying out the reduction in $n = 4 - 2\epsilon$ dimensions and therefore the Kronecker delta representation of dual vectors will be more useful. It is easy to show that in n dimensions,

$$\delta_{q_1 q_2 \dots q_m \mu}^{p_1 p_2 \dots p_m \mu} = (n - m) \delta_{q_1 q_2 \dots q_m}^{p_1 p_2 \dots p_m}. \quad (2.27)$$

Now we consider an another very useful object required in the reduction of tensor integrals, the *projective tensor*

$$\begin{aligned} \omega_\nu^\mu &= \delta_{p_1 p_2 \dots p_m \nu}^{p_1 p_2 \dots p_m \mu} / \Delta_m \\ &= \left(\delta_\nu^\mu - \sum_{i=1}^m v_i^\mu p_{i\nu} \right) = \left(\delta_\nu^\mu - \sum_{i=1}^m v_{i\nu} p_i^\mu \right), \end{aligned} \quad (2.28)$$

for m linearly independent vectors defined in n dimensions. The projective tensor satisfies following identities

$$\omega_\mu^\mu = n - m; \quad \omega_\nu^\mu p_{i\mu} = \omega_\nu^\mu p_i^\nu = 0; \quad \omega_\nu^\mu v_{i\mu} = \omega_\nu^\mu v_i^\nu = 0 \quad \text{and} \quad \omega_\nu^\mu \omega_\rho^\nu = \omega_\rho^\mu. \quad (2.29)$$

Therefore, it is a projection operator into the space orthogonal to the vector space of p_i s (the transverse space). The defining equation of the projective tensor can be seen as a decomposition of the full metric tensor into two orthogonal spaces, *i.e.*,

$$g^{\mu\nu} = \hat{g}^{\mu\nu} + \omega^{\mu\nu}, \quad (2.30)$$

where $\hat{g}^{\mu\nu} = \sum_{i=1}^m v_i^\mu p_i^\nu$, is the metric tensor of the vector space of p_i s and it satisfies $\hat{g}_\mu^\mu = m$; $\hat{g}^{\mu\nu} p_{i\mu} = p_{i\nu}$ & $\hat{g}^{\mu\nu} v_{i\mu} = v_{i\nu}$. Note that $(n - m)$ is the dimensionality of the transverse space and therefore the projective tensor exists only for $m < n$. Like $\hat{g}^{\mu\nu}$, $\omega^{\mu\nu}$ can also be written in terms of orthonormal basis vectors of the transverse space, say \tilde{p}_i s. Thus any vector in n dimensions can be completely expressed in terms of p_i s and \tilde{p}_i s. This is particularly useful in decomposing the loop momentum appearing in the numerator of tensor integrals. From Eq. 2.28,

$$\begin{aligned} l^\mu &= \sum_{i=1}^m (l \cdot v_i) p_i^\mu + \omega_l^\mu \quad (\text{Conventional decomposition}) \\ &= \sum_{i=1}^m (l \cdot p_i) v_i^\mu + \omega_l^\mu \quad (\text{van Neerven - Vermaseren decomposition}). \end{aligned} \quad (2.31)$$

For the particular case of $n = m + 1$, the transverse space is one dimensional and

$$\omega_\nu^\mu = \delta_{p_1 p_2 \dots p_m \nu}^{p_1 p_2 \dots p_m \mu} / \Delta_m = \tilde{p}^\mu \tilde{p}_\nu, \quad (2.32)$$

where $\tilde{p}^\mu = \varepsilon^{p_1 p_2 \dots p_m \mu} / \varepsilon^{p_1 p_2 \dots p_m}$, is the one and only basis vector in the transverse space. The explicit form of \tilde{p}^μ can be used in the reduction of box tensor integrals ($m = 3$) in 4 dimensions. Clearly for $m \geq n$, $\omega_\nu^\mu = 0$ and the loop momentum is completely expressible in p_i s. We have used this fact to reduce the pentagon scalar and tensor integrals ($m = 4$) in 4 dimensions. We will heavily use the ideas developed here in the reduction of tensor integrals [67].

2.1.2 Passarino-Veltman (PV) reduction

Let's first consider the PV method of reducing tensor integrals. The 3-point functions have two linearly independent momenta, p_1 and p_2 . We can either use p_i s (the p -basis)

or their linear combinations q_i s (the q -basis), to decompose the tensor integrals into Lorentz-covariant structures. In the q -basis,

$$C^\mu = \sum_{i=1}^2 q_i^\mu C_i, \quad C^{\mu\nu} = g^{\mu\nu} C_{00} + \sum_{i,j=1}^2 q_i^\mu q_j^\nu C_{ij}, \quad (2.33)$$

$$C^{\mu\nu\rho} = \sum_{i=1}^2 g^{[\mu\nu} q_i^{\rho]} C_{00i} + \sum_{i,j,k=1}^2 q_i^\mu q_j^\nu q_k^\rho C_{ijk}. \quad (2.34)$$

The Lorentz indices within the square bracket represent a sum of all tensor structures with a cyclic permutation of these indices. Note that the tensor coefficients are symmetric under the permutation of all indices. We can extract tensor coefficients by multiplying these expressions with appropriate combinations of the projection operators u_i (see Eq. A.10) and $\omega^{\mu\nu}$ defined above. The tensor coefficients of rank-1, 3-point function are given by,

$$C_i = u_i^\mu C_\mu = \overline{l \cdot u_i} \quad (2.35)$$

$$\begin{aligned} &= \sum_{n=1}^2 (u_i \cdot u_n) \overline{l \cdot q_n} \\ &= \sum_{n=1}^2 (X_2^{-1})_{in} R_n^1, \end{aligned} \quad (2.36)$$

where

$$\begin{aligned} R_n^1 &= \overline{l \cdot q_n} = \frac{1}{2} \overline{(d_n - d_0 - q_n^2)} \\ &= \frac{1}{2} [B_0(n) - B_0(0) - r_n C_0]; \quad r_n = q_n^2. \end{aligned} \quad (2.37)$$

The overline notation implies a division by $d_0 d_1 d_2$ and the n -dimensional loop integration consistent with Eq. 2.6. The tensor coefficients of rank-2, 3-point function

are given by,

$$C_{00} = \frac{1}{(n-2)} \omega^{\mu\nu} C_{\mu\nu} = \frac{1}{(n-2)} \overline{\omega^{ll}} \quad (2.38)$$

$$\begin{aligned} &= \frac{1}{(n-2)} \left[\overline{l^2} - \sum_{i=1}^2 \overline{l \cdot q_i l \cdot u_i} \right] \\ &= \frac{1}{(n-2)} \left[B_0(0) + m^2 C_0 - \frac{1}{2} \sum_{i=1}^2 \overline{(d_i - d_0 - q_i^2) l \cdot u_i} \right] \\ &= \frac{1}{(n-2)} \left[B_0(0) + m^2 C_0 - \frac{1}{2} \left(B_0(0) - \sum_{i=1}^2 q_i^2 C_i \right) \right] \\ \Rightarrow C_{00} &= \frac{1}{(n-2)} \left[m^2 C_0 + \frac{1}{2} B_0(0) + \frac{1}{2} \sum_{i=1}^2 r_i C_i \right]. \end{aligned} \quad (2.39)$$

Note that, $\overline{d_i l \cdot u_i} = 0$ and $\overline{d_0 \sum_{i=1}^2 l \cdot u_i} = -\overline{d_0} = -B_0(0)$.

$$C_{ij} = (u_i^\mu u_j^\nu - \frac{u_i \cdot u_j}{(n-2)} \omega^{\mu\nu}) C_{\mu\nu} = \overline{l \cdot u_i l \cdot u_j} - u_i \cdot u_j C_{00} \quad (2.40)$$

$$\begin{aligned} &= \sum_{n=1}^2 u_i \cdot u_n \overline{l \cdot q_n l \cdot u_j} - u_i \cdot u_j C_{00} \\ &= \sum_{n=1}^2 u_i \cdot u_n [\overline{l \cdot q_n l \cdot u_j} - \delta_{nj} C_{00}] \\ &= \sum_{n=1}^2 (X_2^{-1})_{in} [R_{nj}^2 - \delta_{nj} C_{00}], \end{aligned} \quad (2.41)$$

where

$$\begin{aligned} R_{nj}^2 &= \overline{l \cdot q_n l \cdot u_j} = \frac{1}{2} \overline{(d_n - d_0 - q_n^2) l \cdot u_j} \\ &= \frac{1}{2} [B_\mu(n) - B_\mu(0) - r_n C_\mu] u_j^\mu \\ &= \frac{1}{2} [B_1(n) \delta_{nj}^- - B_j(0) - r_n C_j], \end{aligned} \quad (2.42)$$

with $\delta_{nj}^- = (1 - \delta_{nj})$. $B_j(0)$ are the coefficients of,

$$B^\mu(0) = \overline{l^\mu} = B_1(0) q_1^\mu + B_2(0) q_2^\mu. \quad (2.43)$$

The overline notation used here includes only the propagators d_1 and d_2 . The tensor coefficients of rank-3, 3-point function are given by,

$$C_{00i} = \frac{1}{(n-2)} \omega^{\mu\nu} u_i^\rho C_{\mu\nu\rho} = \frac{1}{(n-2)} \overline{\omega^{ll} l \cdot u_i} \quad (2.44)$$

$$\begin{aligned} &= \frac{1}{(n-2)} \sum_{n=1}^2 (u_i \cdot u_n) \overline{\omega^{ll} l \cdot q_n} \\ &= \sum_{n=1}^2 (X_2^{-1})_{in} R_{n00}^3, \end{aligned} \quad (2.45)$$

where

$$\begin{aligned} R_{n00}^3 &= \frac{1}{(n-2)} \overline{l \cdot q_n \omega^{ll}} = \frac{1}{2(n-2)} \overline{(d_n - d_0 - q_n^2) \omega^{ll}} \\ &= \frac{1}{2} [B_{\mu\nu}(n) - B_{\mu\nu}(0) - r_n C_{\mu\nu}] \frac{\omega^{\mu\nu}}{(n-2)} \\ &= \frac{1}{2} [B_{00}(n) - B_{00}(0) - r_n C_{00}]. \end{aligned} \quad (2.46)$$

Instead of expanding $l \cdot q_i$ if we expand ω^{ll} and use the above result, we get an alternative expression for C_{00i} ,

$$C_{00i} = \frac{1}{(n-1)} \left[m^2 C_i + \frac{1}{2} B_i(0) + \frac{1}{2} \sum_{j=1}^2 r_j C_{ij} \right]. \quad (2.47)$$

$$C_{ijk} = u_i^\mu (u_j^\nu u_k^\rho - \frac{u_j \cdot u_k}{(n-2)} \omega^{\nu\rho}) C_{\mu\nu\rho} - u_i \cdot u_j C_{00k} - u_i \cdot u_k C_{00j} \quad (2.48)$$

$$\begin{aligned} &= \overline{l \cdot u_i (l \cdot u_j l \cdot u_k - \frac{u_j \cdot u_k}{(n-2)} \omega^{ll})} - u_i \cdot u_j C_{00k} - u_i \cdot u_k C_{00j} \\ &= \sum_{n=1}^2 (u_i \cdot u_n) \overline{l \cdot q_n (l \cdot u_j l \cdot u_k - \frac{u_j \cdot u_k}{(n-2)} \omega^{ll})} - u_i \cdot u_j C_{00k} - u_i \cdot u_k C_{00j} \\ &= \sum_{n=1}^2 (X_2^{-1})_{in} [R_{njk}^3 - \delta_{nj} C_{00k} - \delta_{nk} C_{00j}], \end{aligned} \quad (2.49)$$

where

$$\begin{aligned} R_{njk}^3 &= \frac{1}{2} \overline{(d_n - d_0 - q_n^2) (l \cdot u_j l \cdot u_k - \frac{u_j \cdot u_k}{(n-2)} \omega^{ll})} \\ &= \frac{1}{2} [B_{\mu\nu}(n) - B_{\mu\nu}(0) - r_n C_{\mu\nu}] (u_j^\mu u_k^\nu - \frac{u_j \cdot u_k}{(n-2)} \omega^{\mu\nu}) \\ &= \frac{1}{2} [B_{11}(n) \delta_{nj}^- \delta_{nk}^- - B_{jk}(0) - r_n C_{jk}]. \end{aligned} \quad (2.50)$$

$B_{00}(0)$ and $B_{ij}(0)$ are the coefficients of,

$$B^{\mu\nu}(0) = \overline{l^\mu l^\nu} = B_{00}(0)g^{\mu\nu} + \sum_{i,j=1}^2 q_i^\mu q_j^\nu B_{ij}(0). \quad (2.51)$$

Notice that we required at maximum one $l.u_i$ to be written in terms of $l.q_n$. Thus a higher point tensor coefficient is expressed in terms of lower point tensor and scalar coefficients. The same analysis can be extended to the reduction of 4-point functions up to rank-3 ($D_{\mu\nu\rho}$) with appropriate definitions of u_i and $\omega_{\mu\nu}$. For completeness, we give here the reduction of rank-4, 4-point function,

$$\begin{aligned} D^{\mu\nu\rho\sigma} &= g^{[\mu\nu} g^{\rho]\sigma} D_{0000} + \sum_{i,j=1}^3 \left(g^{[\mu\nu} q_i^{\rho]} q_j^\sigma + g^{\sigma[\mu} q_i^\nu q_j^{\rho]} \right) D_{00ij} \\ &+ \sum_{i,j,k,m=1}^3 q_i^\mu q_j^\nu q_k^\rho q_m^\sigma D_{ijklm}. \end{aligned} \quad (2.52)$$

The tensor coefficients are again extracted using suitable combinations of u_i and $\omega_{\mu\nu}$,

$$D_{0000} = \frac{1}{(n-1)(n-3)} \omega^{\mu\nu} \omega^{\rho\sigma} D_{\mu\nu\rho\sigma} \quad (2.53)$$

$$= \frac{1}{(n-1)} \left[m^2 D_{00} + \frac{1}{2} C_{00}(0) + \frac{1}{2} \sum_{i=1}^3 r_i D_{00i} \right]. \quad (2.54)$$

$$D_{00ij} = \frac{\omega^{\mu\nu}}{(n-3)} \left[u_i^\rho u_j^\sigma - u_i \cdot u_j \frac{\omega^{\rho\sigma}}{(n-1)} \right] D_{\mu\nu\rho\sigma} \quad (2.55)$$

$$= \sum_{n=1}^3 (X_2^{-1})_{in} [S_{n00j}^4 - \delta_{nj} D_{0000}], \quad (2.56)$$

where

$$\begin{aligned} S_{n00j}^4 &= \frac{1}{2} [C_{\mu\nu\rho}(n) - C_{\mu\nu\rho}(0) - r_n D_{\mu\nu\rho}] \frac{\omega^{\mu\nu}}{(n-3)} u_j^\rho \\ &= \frac{1}{2} [C_{00jn}(n) \delta_{nj}^- - C_{00j}(0) - r_n D_{00j}]. \end{aligned} \quad (2.57)$$

with $j_n = j \Theta(n-j) + (j-1) \Theta(j-n)$. Noting that,

$$D_{00ij} = \frac{\omega^{\mu\nu}}{(n-3)} \left[u_i^\rho u_j^\sigma - u_i \cdot u_j \frac{\omega^{\rho\sigma}}{(n-3)} \right] D_{\mu\nu\rho\sigma} + 2u_i \cdot u_j D_{0000}, \quad (2.58)$$

an another equivalent form can be obtained,

$$D_{00ij} = \frac{1}{(n-1)} \left[m^2 D_{ij} + \frac{1}{2} C_{ij}(0) + \frac{1}{2} \sum_{n=1}^3 r_n D_{ijn} \right]. \quad (2.59)$$

$$D_{ijkm} = u_i^\mu \left[u_j^\nu u_k^\rho u_m^\sigma - u_j \cdot u_k \frac{\omega^{\nu\rho}}{(n-3)} u_m^\sigma - u_j \cdot u_m \frac{\omega^{\nu\sigma}}{(n-3)} u_k^\rho - u_k \cdot u_m \frac{\omega^{\rho\sigma}}{(n-3)} u_j^\nu \right] \times \\ D_{\mu\nu\rho\sigma} - u_i \cdot u_j D_{00km} - u_i \cdot u_k D_{00jm} - u_i \cdot u_m D_{00jk} \quad (2.60)$$

$$= \sum_{n=1}^3 (X_2^{-1})_{in} \left[S_{njkm}^4 - \delta_{nj} D_{00km} - \delta_{nk} D_{00jm} - \delta_{nm} D_{00jk} \right], \quad (2.61)$$

where

$$S_{njkm}^4 = \frac{1}{2} [C_{\mu\nu\rho}(n) - C_{\mu\nu\rho}(0) - r_n D_{\mu\nu\rho}] \times \\ \left[u_j^\mu u_k^\nu u_m^\rho - u_j \cdot u_k \frac{\omega^{\mu\nu}}{(n-3)} u_m^\rho - u_j \cdot u_m \frac{\omega^{\mu\rho}}{(n-3)} u_k^\nu - u_k \cdot u_m \frac{\omega^{\nu\rho}}{(n-3)} u_j^\mu \right] \\ = \frac{1}{2} [C_{jnk_n m_n}(n) \delta_{nj}^- \delta_{nk}^- \delta_{nm}^- - C_{jkm}(0) - r_n D_{jkm}]. \quad (2.62)$$

$C_{00i}(0)$ and $C_{ijk}(0)$ are the coefficients of,

$$C^{\mu\nu\rho}(0) = \overline{l^\mu l^\nu l^\rho} = \sum_{i=1}^3 g^{[\mu\nu} q_i^{\rho]} C_{00i}(0) + \sum_{i,j,k=1}^3 q_i^\mu q_j^\nu q_k^\rho C_{ijk}(0). \quad (2.63)$$

A complete list of tensor coefficients related to 1-,2-,3- and 4-point functions is given in the appendix B of Ref. [65]. We have maintained the n dependence in writing these tensor coefficients. In the above, one could have also used p -basis to expand tensor integrals. It is just a matter of personal taste.

2.1.3 Oldenborgh-Vermaseren (OV) reduction

Now we turn to a tensor reduction method which is equivalent to the above but avoids explicit computation of tensor coefficients. Introduction of artificial virtualities for internal lines and the use of generalized Kronecker deltas allow compact formulae for the tensor reduction. We will describe all the important aspects of this method by applying it to the reduction of 3-point functions. We define s -vectors related to the internal lines by $p_1 = s_1 - s_0$, $p_2 = s_2 - s_1$, $p_3 = s_0 - s_2$, such that $s_i^2 = m_i^2$, and $p_1 + p_2 + p_3 = 0$. Recall the *van Neerven-Vermaseren* decomposition of the loop momentum for a three-point function,

$$l^\mu = \mathcal{P}^\mu + \omega_l^\mu; \quad \mathcal{P}^\mu = \sum_{i=1}^2 (l \cdot p_i) v_i^\mu, \quad (2.64)$$

$$\text{where } v_1^\mu = \delta_{p_1 p_2}^{\mu p_2} / \Delta_2, \quad v_2^\mu = \delta_{p_1 p_2}^{p_1 \mu} / \Delta_2 \quad \text{and} \quad \omega_\nu^\mu = \delta_{p_1 p_2 \nu}^{p_1 p_2 \mu} / \Delta_2. \quad (2.65)$$

Writing $l.p_i$ in terms of propagators,

$$\mathcal{P}^\mu = \frac{1}{\Delta_2} \left[\delta_{p_1 p_2}^{s_0 \alpha} \delta_{p_1 p_2}^{\mu \alpha} - \frac{1}{2} (d_0 \delta_{p_1 p_2}^{\mu p_2} + d_1 \delta_{p_1 p_2}^{\mu p_3} + d_2 \delta_{p_1 p_2}^{\mu p_1}) \right]. \quad (2.66)$$

Also note that $\omega_\nu^\mu p_i^\nu = \omega_\nu^\mu \mathcal{P}^\nu = 0$. We are now set to do the tensor reduction. We will again use the overline notation introduced previously. The rank-1, 3-point function is give by,

$$C^\mu = \overline{l}^\mu \quad (2.67)$$

$$= \overline{\mathcal{P}^\mu} + \overline{\omega_l^\mu} \quad (2.68)$$

$$= \frac{1}{\Delta_2} \left[\delta_{p_1 p_2}^{s_0 \alpha} \delta_{p_1 p_2}^{\mu \alpha} C_0 - \frac{1}{2} (\delta_{p_1 p_2}^{\mu p_2} B_0(0) + \delta_{p_1 p_2}^{\mu p_3} B_0(1) + \delta_{p_1 p_2}^{\mu p_1} B_0(2)) \right]. \quad (2.69)$$

Since \overline{l}^ν can only be a linear combination of p_1 and p_2 , it implies $\overline{\omega_l^\mu} = 0$. This holds true for any odd combination of ω_l^μ . In the reduction of higher rank tensors we replace one l at a time using Eq. 2.64. The rank-2, 3-point function is given by,

$$C^{\mu\nu} = \overline{l}^\mu \overline{l}^\nu \quad (2.70)$$

$$= \overline{\mathcal{P}^\mu \overline{l}^\nu} + \overline{\omega_l^\mu \overline{l}^\nu} \quad (2.71)$$

$$= \frac{1}{\Delta_2} \left[\delta_{p_1 p_2}^{s_0 \alpha} \delta_{p_1 p_2}^{\mu \alpha} C_\nu - \frac{1}{2} (\delta_{p_1 p_2}^{\mu p_2} B_\nu(0) + \delta_{p_1 p_2}^{\mu p_3} B_\nu(1) + \delta_{p_1 p_2}^{\mu p_1} B_\nu(2)) \right] + \omega_\nu^\mu C_{00}, \quad (2.72)$$

$$\text{where } C_{00} = \frac{1}{(n-2)} \overline{\omega_l^\mu} = \frac{1}{(n-2)} \overline{(l^2 - \mathcal{P}^2)} \quad (2.73)$$

$$\text{and } \overline{(l^2 - \mathcal{P}^2)} = \frac{1}{\Delta_2} \left[\delta_{s_0 p_1 p_2}^{s_0 p_1 p_2} C_0 + \frac{1}{2} \delta_{p_1 p_2}^{s_1 p_2} B_0(0) + \frac{1}{2} \delta_{p_1 p_2}^{s_0 p_3} B_0(1) + \frac{1}{2} \delta_{p_1 p_2}^{s_0 p_1} B_0(2) \right]. \quad (2.74)$$

Similarly for the rank-3, 3-point function,

$$C^{\mu\nu\rho} = \overline{l}^\mu \overline{l}^\nu \overline{l}^\rho \quad (2.75)$$

$$= \overline{\mathcal{P}^\mu \overline{l}^\nu \overline{l}^\rho} + \overline{\omega_l^\mu \overline{l}^\nu \overline{l}^\rho} \quad (2.76)$$

$$= \frac{1}{\Delta_2} \left[\delta_{p_1 p_2}^{s_0 \alpha} \delta_{p_1 p_2}^{\mu \alpha} C_{\nu\rho} - \frac{1}{2} (\delta_{p_1 p_2}^{\mu p_2} B_{\nu\rho}(0) + \delta_{p_1 p_2}^{\mu p_3} B_{\nu\rho}(1) + \delta_{p_1 p_2}^{\mu p_1} B_{\nu\rho}(2)) \right] + \overline{\omega_l^\mu \mathcal{P}^\nu \overline{l}^\rho} + \overline{\omega_l^\mu \omega_l^\nu \overline{l}^\rho} \quad (2.77)$$

$$\begin{aligned}
\Rightarrow C^{\mu\nu\rho} &= \frac{1}{\Delta_2} \left[\delta_{p_1 p_2}^{s_0 \alpha} \delta_{p_1 p_2}^{\mu \alpha} C_{\nu\rho} - \frac{1}{2} \left(\delta_{p_1 p_2}^{\mu p_2} B_{\nu\rho}(0) + \delta_{p_1 p_2}^{\mu p_3} B_{\nu\rho}(1) + \delta_{p_1 p_2}^{\mu p_1} B_{\nu\rho}(2) \right) \right] \\
&+ \frac{\omega_\rho^\mu}{\Delta_2} \left[\delta_{p_1 p_2}^{s_0 \alpha} \delta_{p_1 p_2}^{\nu \alpha} C_{00} - \frac{1}{2} \left(\delta_{p_1 p_2}^{\nu p_2} B_{00}(0) + \delta_{p_1 p_2}^{\nu p_3} B_{00}(1) + \delta_{p_1 p_2}^{\nu p_1} B_{00}(2) \right) \right] \\
&+ \overline{\omega_l^\mu \omega_l^\nu \mathcal{P}^\rho} + \overline{\omega_l^\mu \omega_l^\nu \omega_l^\rho}
\end{aligned} \tag{2.78}$$

$$\begin{aligned}
\Rightarrow C^{\mu\nu\rho} &= \frac{1}{\Delta_2} \left[\delta_{p_1 p_2}^{s_0 \alpha} \delta_{p_1 p_2}^{\mu \alpha} C_{\nu\rho} - \frac{1}{2} \left(\delta_{p_1 p_2}^{\mu p_2} B_{\nu\rho}(0) + \delta_{p_1 p_2}^{\mu p_3} B_{\nu\rho}(1) + \delta_{p_1 p_2}^{\mu p_1} B_{\nu\rho}(2) \right) \right] \\
&+ \frac{\omega_\rho^\mu}{\Delta_2} \left[\delta_{p_1 p_2}^{s_0 \alpha} \delta_{p_1 p_2}^{\nu \alpha} C_{00} - \frac{1}{2} \left(\delta_{p_1 p_2}^{\nu p_2} B_{00}(0) + \delta_{p_1 p_2}^{\nu p_3} B_{00}(1) + \delta_{p_1 p_2}^{\nu p_1} B_{00}(2) \right) \right] \\
&+ \frac{\omega_\nu^\mu}{\Delta_2} \left[\delta_{p_1 p_2}^{s_0 \alpha} \delta_{p_1 p_2}^{\rho \alpha} C_{00} - \frac{1}{2} \left(\delta_{p_1 p_2}^{\rho p_2} B_{00}(0) + \delta_{p_1 p_2}^{\rho p_3} B_{00}(1) + \delta_{p_1 p_2}^{\rho p_1} B_{00}(2) \right) \right].
\end{aligned} \tag{2.79}$$

$B_{00}(N)$ is the coefficient of $B_{\mu\nu}(N)$. Although we can reduce 2-point functions also using this method, we stick to the PV type reduction for B_μ and $B_{\mu\nu}$ described above. One can perform the reduction of 4-point functions along the same line with appropriately defined \mathcal{P}^μ and ω_ν^μ . For the sake of completeness we list all the important relations required in the recursive reduction of 4-point functions up to rank-4. For the reduction of box tensor integrals,

$$l^\mu = \mathcal{P}^\mu + \omega_l^\mu; \quad \mathcal{P}^\mu = \sum_{i=1}^3 (l \cdot p_i) v_i^\mu, \tag{2.80}$$

$$\begin{aligned}
\text{where } v_1^\mu &= \delta_{p_1 p_2 p_3}^{\mu p_2 p_3} / \Delta_3, \quad v_2^\mu = \delta_{p_1 p_2 p_3}^{p_1 \mu p_3} / \Delta_3, \\
v_3^\mu &= \delta_{p_1 p_2 p_3}^{p_1 p_2 \mu} / \Delta_3 \quad \text{and} \quad \omega_\nu^\mu = \delta_{p_1 p_2 p_3 \nu}^{\mu p_1 p_2 p_3} / \Delta_3.
\end{aligned} \tag{2.81}$$

$$\mathcal{P}^\mu = \frac{1}{\Delta_3} \left[\frac{1}{2} \delta_{p_1 p_2 p_3}^{s_0 \alpha \beta} \delta_{p_1 p_2 p_3}^{\mu \alpha \beta} - \frac{1}{2} \left(d_0 \delta_{p_1 p_2 p_3}^{\mu p_2 p_3} - d_1 \delta_{p_1 p_2 p_3}^{\mu p_3 p_4} + d_2 \delta_{p_1 p_2 p_3}^{\mu p_4 p_1} - d_3 \delta_{p_1 p_2 p_3}^{\mu p_1 p_2} \right) \right]. \tag{2.82}$$

$$\begin{aligned}
\overline{(l^2 - \mathcal{P}^2)} &= \frac{1}{\Delta_3} \left[\delta_{s_0 p_1 p_2 p_3}^{s_0 p_1 p_2 p_3} D_0 + \frac{1}{2} \delta_{p_1 p_2 p_3}^{s_1 p_2 p_3} C_0(0) - \frac{1}{2} \delta_{p_1 p_2 p_3}^{s_0 p_3 p_4} C_0(1) \right. \\
&\quad \left. + \frac{1}{2} \delta_{p_1 p_2 p_3}^{s_0 p_4 p_1} C_0(2) - \frac{1}{2} \delta_{p_1 p_2 p_3}^{s_0 p_1 p_2} C_0(3) \right].
\end{aligned} \tag{2.83}$$

$$\begin{aligned}
\overline{(l^2 - \mathcal{P}^2)^2} &= \frac{1}{\Delta_3} \left[\delta_{s_0 p_1 p_2 p_3}^{s_0 p_1 p_2 p_3} \overline{(l^2 - \mathcal{P}^2)} + \frac{n-3}{2} \delta_{p_1 p_2 p_3}^{s_1 p_2 p_3} C_{00}(0) - \frac{n-3}{2} \delta_{p_1 p_2 p_3}^{s_0 p_3 p_4} C_{00}(1) \right. \\
&\quad \left. + \frac{n-3}{2} \delta_{p_1 p_2 p_3}^{s_0 p_4 p_1} C_{00}(2) - \frac{n-3}{2} \delta_{p_1 p_2 p_3}^{s_0 p_1 p_2} C_{00}(3) \right].
\end{aligned} \tag{2.84}$$

$C_{00}(N)$ can be obtained following Eq. 2.73. The tensor reduction method of Oldenborgh and Vermaseren can be seen as a reduction in dual vector basis. This method of reduction, due to its compactness, is very well suited for numerical implementation. More details on the method can be found in Ref. [63].

2.2 Reduction of Five-point Tensor Integrals

The SM processes considered in this thesis have five external particles, therefore the reduction of 5-point functions is also required. The most complicated tensor structure that occur in these processes is the rank-5, 5-point function $E_{\mu\nu\rho\sigma\alpha}$. Since these integrals are UV finite, we can perform the tensor reduction in 4 dimensions. The PV type reduction can be applied to them, but at this level it becomes very cumbersome. Also the tensor decomposition of $E_{\mu\nu}$ and of higher rank 5-point functions is overcomplete because in 4 dimensions,

$$g^{\mu\nu} = \sum_{i=1}^4 p_i^\mu v_i^\nu = \sum_{i,j=1}^4 (v_i \cdot v_j) p_i^\mu p_j^\nu, \quad (2.85)$$

i.e., the four vectors p_i^μ span the $n = 4$ dimensional Minkowski space. Thus for the 5-point functions,

$$\begin{aligned} l^\mu &= \mathcal{P}^\mu = \sum_{i=1}^4 (l \cdot p_i) v_i^\mu \\ &= \sum_{i=1}^4 v_i^\mu \left[\frac{1}{2} d_i - \frac{1}{2} d_{i-1} + s_0 \cdot p_i \right], \end{aligned} \quad (2.86)$$

and we can use ε -tensor representation of dual vectors, given by

$$\begin{aligned} v_1^\mu &= \varepsilon^{\mu p_2 p_3 p_4} / \varepsilon^{p_1 p_2 p_3 p_4}, \quad v_2^\mu = \varepsilon^{p_1 \mu p_3 p_4} / \varepsilon^{p_1 p_2 p_3 p_4}, \\ v_3^\mu &= \varepsilon^{p_1 p_2 \mu p_4} / \varepsilon^{p_1 p_2 p_3 p_4}, \quad v_4^\mu = \varepsilon^{p_1 p_2 p_3 \mu} / \varepsilon^{p_1 p_2 p_3 p_4}. \end{aligned} \quad (2.87)$$

Therefore,

$$\begin{aligned} \mathcal{P}^\mu &= \sum_{i=1}^4 s_0 \cdot p_i v_i^\mu - \frac{1}{2} (d_0 \varepsilon^{\mu p_2 p_3 p_4} + d_1 \varepsilon^{\mu p_3 p_4 p_5} + d_2 \varepsilon^{\mu p_4 p_5 p_1} \\ &\quad + d_3 \varepsilon^{\mu p_5 p_1 p_2} + d_4 \varepsilon^{\mu p_1 p_2 p_3}) / \varepsilon^{p_1 p_2 p_3 p_4}. \end{aligned} \quad (2.88)$$

This relation now can be used to write down 5-point tensor integrals in terms of 5-point and 4-point functions of lower rank. For example, the rank-5, 5-point function is given by,

$$E^{\mu\nu\rho\sigma\alpha} = \overline{l^\mu l^\nu l^\rho l^\sigma l^\alpha} = \overline{l^\mu l^\nu l^\rho l^\sigma \mathcal{P}^\alpha} \quad (2.89)$$

$$\begin{aligned} &= E^{\mu\nu\rho\sigma} \sum_{i=1}^4 s_{0 \cdot p_i} v_i^\alpha - \left[D^{\mu\nu\rho\sigma}(0) \varepsilon^{\alpha p_2 p_3 p_4} + D^{\mu\nu\rho\sigma}(1) \varepsilon^{\alpha p_3 p_4 p_5} \right. \\ &\quad \left. + D^{\mu\nu\rho\sigma}(2) \varepsilon^{\alpha p_4 p_5 p_1} + D^{\mu\nu\rho\sigma}(3) \varepsilon^{\alpha p_5 p_1 p_2} + D^{\mu\nu\rho\sigma}(4) \varepsilon^{\alpha p_1 p_2 p_3} \right] / \varepsilon^{p_1 p_2 p_3 p_4} \end{aligned} \quad (2.90)$$

and so on for lower rank 5-point functions. The reduction of 4-point functions appearing in the above pentagon tensor reduction must be done in n dimensions. This ends our discussion on the reduction of one-loop tensor integrals considered in this thesis and we confirm the most general structure of one-loop amplitudes given in Eq. 2.13.

Remark: In a dimensionally regulated tensor coefficient/integral, replacing $n = 4 - 2\epsilon$ at the end of the complete reduction leads to $\mathcal{O}(\epsilon)$ terms in its expression. Whenever these $\mathcal{O}(\epsilon)$ terms hit $1/\epsilon$ pole of UV divergent integrals (A_0 and B_0 in the complete reduction), the tensor coefficient gets finite contributions. These finite contributions are called rational terms. The rational part \mathcal{R} in Eq. 2.13, is the collection of all such terms in a one-loop amplitude. We see that the rational terms appear due to the UV regularization of tensor integrals. However, this does not mean that those tensor coefficients/integrals which are UV finite will not have rational terms, or tensor coefficients which are UV divergent will necessarily have rational terms. For example, all rank-one tensor coefficients (including B_1 which is UV divergent) do not have rational terms because the n dependence enters through $g_{\mu\nu}$, only when rank ≥ 2 . On the other hand, the tensor coefficients C_{ij} , D_{ijk} , D_{00ij} and D_{ijkl} , all are UV finite, but they do have rational terms. Unlike the rational terms of a UV divergent tensor coefficient, those of a UV finite tensor coefficient are implicit, that is, the rational terms in a UV finite tensor coefficient arise only from the UV divergent tensor coefficients. For example, see the expression of C_{ij} in Eqs. 2.41 and 2.42. This also implies that the n dependence in D_{00ij} (Eq. 2.58) is of no consequence and we can take $n = 4$. The same is true for the UV finite tensor coefficients of 5-point functions with rank ≤ 5 , and the reduction of 5-point functions into 4-point functions using the

4-dimensional Schouten identity is completely justified. Note that the rational terms in tensor coefficients of N -point functions with $N > 2$ are independent of internal line masses if $m_i^2 = m^2$. The explicit expressions for the rational parts of basic tensor coefficients are given in Ref. [68].

2.3 Fermion Loop Amplitudes

In this thesis, as mentioned in the introduction, we will be dealing with the fermion loop amplitudes. The fermion loop diagrams/amplitudes have many special properties which can serve as an important check on calculations and can even simplify certain calculations sometimes. In this section, we will discuss some of the properties which we have come across while calculating fermion loop diagrams.

2.3.1 IR finiteness of fermion loop diagrams

In the mass regularization, the infrared singular part of a massless fermion loop diagram appears as,

$$\sim A \ln^2(m^2) + B \ln(m^2) + \mathcal{O}(m^2), \quad (2.91)$$

where A and B are complex functions of kinematic invariants. The $\ln^2(m^2)$ piece refers to an overlapping of the soft and collinear singularities. The classification of IR singularities at one-loop is given in appendix B.1. In the following, we will show that for a given (individual) fermion loop diagram, $A = B = 0$, that is, it is IR finite. In general, IR finiteness is expected to hold for a gauge invariant combination of fermion loop diagrams like in the case of their UV finiteness. The proof is obvious for the case of massive fermions in the loop. Also, if all the external legs are massive/offshell, the diagram would be IR finite even for massless fermions in the loop. So we need to consider only those fermion loop diagrams in which fermions are massless or more correctly their masses can be neglected and at least one external leg is massless.

In general, we can have scalars, gauge bosons and gravitons attached to a fermion loop. With one massless external particle we expect only collinear singularity while for two adjacent external massless particles, the soft and collinear singularities and their overlap may develop. IR finiteness of a fermion loop diagram can be shown by

showing its soft finiteness and collinear finiteness. This automatically takes care of its finiteness in overlapping regions. At one-loop, the general fermion loop integral has the following form (see Fig. 2.2),

$$I \simeq \int d^n l \frac{\text{tr}(\dots \not{l}_{i-1} V_i \not{l}_i V_{i+1} \not{l}_{i+1} \dots)}{\dots l_{i-1}^2 l_i^2 l_{i+1}^2 \dots}, \quad (2.92)$$

where V_i s are vertex factors for a given massless external particle attached to the

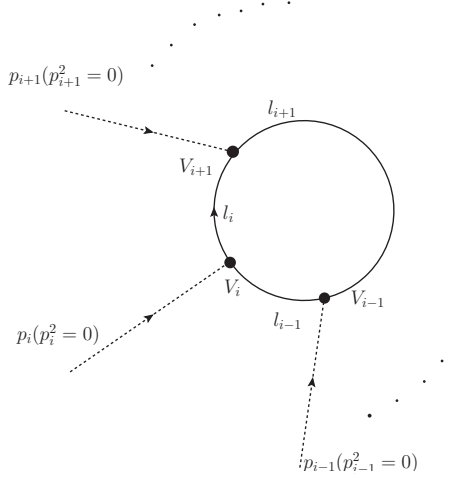


Figure 2.2: Massless fermion loop diagram. Dotted external lines represent any suitable massless particle.

fermion loop. From the momentum conservation at each vertex, it is clear that $l_i = l_{i-1} + p_i$, $l_{i+1} = l_i + p_{i+1}$ etc. The Feynman rules for needed vertices are given in Fig. 2.3. For simplification, factors of ‘ i ’ and coupling constants etc. are dropped in writing those rules. We did not consider graviton-graviton-fermion-fermion vertex, since it does not correspond to a soft or collinear configuration described above. We will closely follow the analysis of IR singular structure of one-loop diagrams described in the appendix B.1.

First we would like to see the behavior of this integral as any of the internal lines becomes soft, *i.e.*, its momentum vanishes. Without loss of generality, we consider softness of l_i and take $l_i = \epsilon$. We see that in the limit $\epsilon \rightarrow 0$, the denominators which

vanish in general are

$$\begin{aligned}
l_{i-1}^2 &= \epsilon^2 - 2\epsilon \cdot p_i, \\
l_i^2 &= \epsilon^2 \\
\text{and } l_{i+1}^2 &= \epsilon^2 + 2\epsilon \cdot p_{i+1},
\end{aligned} \tag{2.93}$$

where we have used on mass-shell conditions for p_i and p_{i+1} . Neglecting ϵ^2 with respect to $\epsilon \cdot p_i$ and $\epsilon \cdot p_{i+1}$ in Eq. 2.93, we see that the integral in Eq. 2.92, in the soft limit, behaves as

$$I \sim \int d^n \epsilon \frac{\not{\epsilon}}{\epsilon \cdot p_i \epsilon^2 \epsilon \cdot p_{i+1}} \sim \epsilon^{n-3}, \tag{2.94}$$

and it vanishes in $n = 4$ dimensions. Thus each fermion loop diagram is soft finite, independent of the kind of massless external particles attached to it. We should mention here that the soft finiteness of fermion loop diagrams is indirectly shown by Kinoshita in [69].

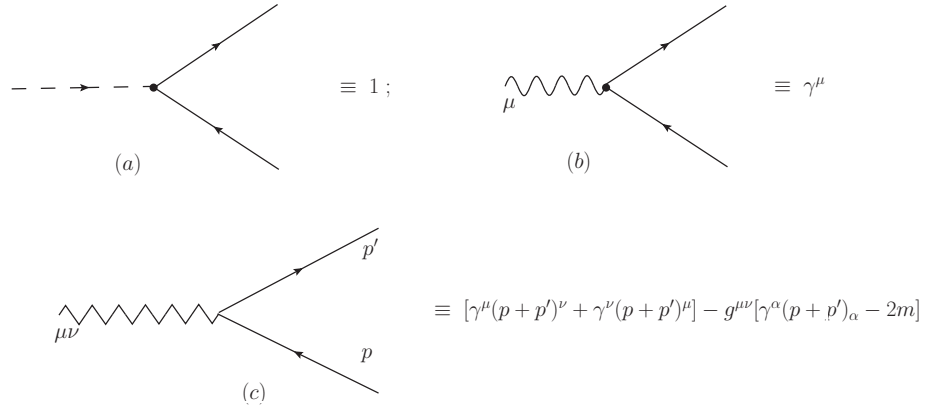


Figure 2.3: Feynman rules: (a) scalar-fermion-fermion vertex (b) vector boson-fermion-fermion vertex (c) graviton-fermion-fermion vertex

Next we consider the behavior of the fermion loop integral in collinear region. We take $l_i = xp_{i+1} + \epsilon_\perp$, ($x \neq 0, -1$ as it corresponds to the softness of l_i and l_{i+1} , respectively) with $\epsilon_\perp \cdot p_{i+1} = 0$. Note that in $\epsilon_\perp \rightarrow 0$ limit, this condition implies collinearity of l_i with p_{i+1} . In this collinear limit, only vanishing denominators are $l_i^2 = \epsilon_\perp^2$ and $l_{i+1}^2 = \epsilon_\perp^2$. Thus the integral in Eq. 2.92 reads,

$$I \simeq \int \frac{d^n \epsilon_\perp}{\epsilon_\perp^4} \text{tr}(\dots l_{i-1} V_i \not{p}_{i+1} V_{i+1} \not{p}_{i+1} \dots). \tag{2.95}$$

We need to make the above substitution for l_i in V_i s also, in case they may depend on the loop momentum, *e.g.*, in the graviton-fermion-fermion vertex. Since the vertex factors are different for different kind of external particles (see Fig. 2.3), we will consider three separate cases to see the behavior of fermion loop integral in the collinear limit.

1. Scalars:

In this case, the vertex factor is simply $V_{i+1} = 1$, and since $\not{p}_{i+1}\not{p}_{i+1} = p_{i+1}^2 = 0$, the integral in Eq. 2.95 is

$$I \simeq \int \frac{d^n \epsilon_\perp}{\epsilon_\perp^4} \text{tr}(\dots \not{l}_{i-1} \not{p}_{i+1} \not{p}_{i+1} \dots) = 0. \quad (2.96)$$

2. Vector bosons:

The vertex factor in this case, is

$$V_{i+1} = \gamma_\mu e_{i+1}^\mu = \not{e}_{i+1}. \quad (2.97)$$

Here e_{i+1}^μ is the polarization vector of the vector boson with momentum p_{i+1} . Using the transversality and on-shell conditions for the vector boson, we see that

$$\not{p}_{i+1} \not{e}_{i+1} \not{p}_{i+1} = 2 \not{p}_{i+1} e_{i+1} \cdot p_{i+1} - p_{i+1}^2 \not{e}_{i+1} = 0. \quad (2.98)$$

and therefore the fermion loop integral in collinear limit, Eq. 2.95, vanishes.

3. Gravitons:

The graviton-fermion vertex factor is given by

$$V_{i+1} = [\gamma_\mu (2l_i + p_{i+1})_\nu + \gamma_\nu (2l_i + p_{i+1})_\mu - g_{\mu\nu} (2\not{l}_i + \not{p}_{i+1} - 2m)] e_{i+1}^{\mu\nu}, \quad (2.99)$$

where $e_{i+1}^{\mu\nu}$ is the polarization tensor for graviton of momentum p_{i+1} . It has following well known properties,

$$\begin{aligned} e_{i+1}^{\mu\nu} g_{\mu\nu} = (e_{i+1})_\mu^\mu &= 0 \text{ (traceless condition),} \\ p_{i+1}^\mu (e_{i+1})_{\mu\nu} &= 0 \text{ (transverse condition).} \end{aligned} \quad (2.100)$$

Using these properties the vertex factor in Eq. 2.99 becomes

$$V_{i+1} = 4\gamma_\mu e_{i+1}^{\mu\nu} (l_i)_\nu. \quad (2.101)$$

In the collinear limit, taken above, it is

$$V_{i+1} = 4x\gamma_\mu e_{i+1}^{\mu\nu} (p_{i+1})_\nu = 0, \quad (2.102)$$

due to the transverse condition. Therefore the fermion loop diagram with external gravitons, like the cases of scalars and vector bosons, is also collinear finite.

Combining all the above results of this section, we see that a general fermion loop diagram is soft as well as collinear finite. To summarize, the soft finiteness of fermion loop diagrams follows from simple power counting in vanishing loop momentum, while their collinear finiteness results utilizing various properties of massless external particles attached to the loop. The result holds even for axial coupling of external particles with the fermion. Though we have not considered any flavor change in the loop, it should be clear from the above analysis that our result remains true for any possible flavor changing interaction vertex in the loop.

We can utilize the above fact regarding an individual fermion loop diagram to show, that the IR structure of any one-loop amplitude with $N \geq 3$ can be fixed completely in terms of the IR structure of 3-point functions only. Since we have learned quite a bit about one-loop amplitudes, it would be sufficient for us to show that the IR singularities of box scalar integrals can be expressed in terms of those of reduced triangle scalars. The amplitude of the fermion loop diagram, shown in Fig. 2.4, is²

$$\begin{aligned} \mathcal{M}_{1234}(\phi^4) &= \int \frac{d^n l}{(2\pi)^n} \frac{\text{tr}(\not{l} \not{l}_3 \not{l}_2 \not{l}_1)}{l^2 l_1^2 l_2^2 l_3^2} \\ &= \int \frac{d^n l}{(2\pi)^n} \frac{4(l.l_3 l_2.l_1 - l.l_2 l_3.l_1 + l.l_1 l_2.l_3)}{l^2 l_1^2 l_2^2 l_3^2}. \end{aligned} \quad (2.103)$$

²Note that there are two more independent diagrams which contribute to the ϕ^4 -amplitude in the Yukawa theory. We do not require them here.

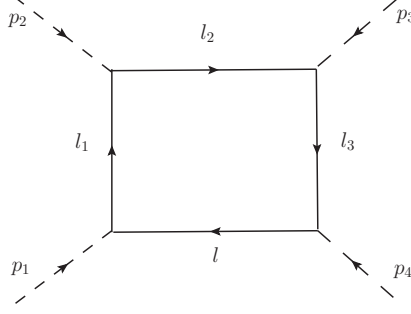


Figure 2.4: Interaction of 4 scalars in the Yukawa theory of scalars and fermions.

Rearranging the terms in the numerator, we can write

$$\begin{aligned}
\mathcal{M}_{1234}(\phi^4) &= (p_1^2 p_3^2 + p_2^2 p_4^2 - st) D_0 + (s - p_1^2 - p_2^2) C_0(3) \\
&\quad + (t - p_1^2 - p_4^2) C_0(2) + (s - p_3^2 - p_4^2) C_0(1) \\
&\quad + (t - p_2^2 - p_3^2) C_0(0) + 2 B_0(0, 2) + 2 B_0(1, 3), \quad (2.104)
\end{aligned}$$

where $s = (p_1 + p_2)^2$ and $t = (p_2 + p_3)^2$. $C_0(i)$ and $B_0(i, j)$ are reduced triangles and bubbles written in the missing propagator notation introduced earlier in this chapter. Since the bubble scalars are IR finite, the IR finiteness of the above fermion loop amplitude implies

$$\begin{aligned}
D_0|_{IR} &= \frac{1}{(st - p_1^2 p_3^2 - p_2^2 p_4^2)} \left[(t - p_2^2 - p_3^2) C_0(0)|_{IR} + (s - p_3^2 - p_4^2) C_0(1)|_{IR} \right. \\
&\quad \left. + (t - p_1^2 - p_4^2) C_0(2)|_{IR} + (s - p_1^2 - p_2^2) C_0(3)|_{IR} \right], \quad (2.105)
\end{aligned}$$

which is the desired result. It can be compared with the identity, derived in [60]

$$D_0^n = \frac{1}{2} \left(\sum_{i=0}^3 \alpha_i C_0^n(i) + (3 - n) \beta D_0^{n+2} \right), \quad (2.106)$$

where $\alpha_i = \sum_{j=0}^3 (Y^{-1})_{i+1, j+1}$ and $\beta = \sum_{i=0}^3 \alpha_i$. Y_{ij} is the modified Cayley matrix of the box integral. Since the six-dimensional box integral is finite, the IR structure of box integrals is completely decided by that of triangle integrals in 4 dimensions. We have used the identity in Eq. 2.105, to obtain the IR singular terms in some of the complicated box scalar integrals listed in the appendix B.2. The IR finiteness of an individual Feynman diagram can also serve a good check on tensor reduction routines.

2.3.2 Rational terms, Gauge invariance, Anomaly & Decoupling in fermion loop amplitudes

We know that the rational part \mathcal{R} in Eq. 2.13, is a result of the UV regularization of tensor integrals. In a UV finite fermion loop amplitude, \mathcal{R} is independent of masses of internal lines³. We have verified this in many UV finite fermion loop amplitudes including those considered in this thesis. It should be clear from the general structure of one-loop amplitudes that in a gauge invariant amplitude, \mathcal{R} should be separately gauge invariant. In the case of one-loop calculation of fermion loop diagrams, in dimensional regularization, the issue of chiral anomaly is related to the presence of odd number of γ^5 in a linearly (or worse) divergent integrals. There is always an ambiguity in carrying out the full calculation in dimensional regularization as γ^5 is strictly a 4-dimensional object. However, this ambiguity arises only in fixing the rational part of the amplitude. The non-rational finite part of the amplitude is strictly 4-dimensional. Therefore, any $\mathcal{O}(\epsilon)$ structure of γ^5 , if it at all exists in $n = 4 - 2\epsilon$ dimensions, should contribute to the rational part only. Thus anomalies affect only the rational part of the amplitude. They are also independent of the fermion mass. It is well known that anomalies may affect the gauge invariance of the amplitude. In the presence of anomaly, any violation of the gauge invariance of an amplitude should occur only in the rational part of the amplitude – the non-rational part should remain gauge invariant.

In a fermion loop amplitude containing both the vector (γ^μ) and axial-vector ($\gamma^\mu\gamma^5$) type couplings, it is reasonable to expect that the chiral anomaly, being associated with γ^5 , should spoil only the axial-vector current conservation and the conservation of vector current must hold. However, it is not very clear if this feature can always be ensured by treating γ^5 in 4 dimensions. The 4-dimensional γ^5 may lead to spurious anomalies in the amplitude, resulting in the non-conservation of vector currents. To ensure the vector current conservation in the amplitude, it is advisable to use an appropriate prescription for γ^5 in n dimensions. It is important to note that if we do not regulate anomaly by using a suitable n -dimensional γ^5 prescription,

³To our knowledge, there is no proof of this statement and it can be taken as a conjecture. From the point-of-view of the validity of this statement, any overall factor of fermion mass in the amplitude is irrelevant.

various other symmetries of the amplitude may not hold. Even the relation between charge-conjugated fermion loop diagrams does not hold and the violation, as we now expect, is only in the rational part. Thus by using an appropriate prescription for γ^5 in n dimensions, we generate a rational part consistent with various symmetries of the amplitude. The treatment of γ^5 in n dimensions is discussed in the appendix C.2.

Now we will discuss how one can obtain the correct rational part of a fermion loop amplitude by doing the full calculation just in 4 dimensions. The decoupling of heavy fermions is in general expected in any UV finite fermion loop amplitude involving couplings which are not proportional to the fermion mass in the loop [70]. This is a very nice feature of fermion loop amplitudes. It can be utilized to fix the rational part of the amplitude without any ambiguity. It is particularly important in calculating fermion loop amplitudes suffering from the anomaly and where an n -dimensional γ^5 prescription is needed to generate the rational part consistent with various symmetries of the amplitude. Since the amplitudes are UV finite and the decoupling of heavy fermions does hold, it implies that there must be a cancellation between the mass independent $(n-4)$ -dimensional rational part and the 4-dimensional non-rational finite part of the amplitude in Eq. 2.13 as large fermion mass limit is taken. Therefore, we do not need to calculate the rational terms explicitly. The rational part \mathcal{R} is simply the negative of the non-rational part of the amplitude in large fermion mass limit. Though the decoupling does not hold if a Higgs boson is attached to the fermion loop, the structure of the fermion loop amplitude (with Higgs bosons) suggests that one can still fix the rational part by taking the large fermion mass limit. For that, one should take away the overall (explicit) factor of the fermion mass before taking the limit. Once again the amplitude goes to zero indicating a cancellation between the rational part and the non-rational part of the amplitude. In the appendix C.1, we have given the expressions of ggH and ggZ quark loop amplitudes treating both the gluons off-shell. One can see there that, indeed, after removing any overall factor of quark mass from the amplitude, the rational terms are independent of quark mass and in the $m^2 \rightarrow \infty$ limit, the amplitude vanishes due to a cancellation between rational and non-rational parts of the amplitude. This knowledge, about the rational terms in UV finite fermion loop amplitudes, also gives

an opportunity to examine the validity of the reduction of 5-point functions into 4-point functions using the 4-dimensional identity. One may worry that carrying out these reductions also in n dimensions may give additional contribution to the rational part of the amplitude. In our SM projects described in chapter 3, we have confirmed by making separate gauge invariance checks on the rational part and also by checking the decoupling theorem in UV finite amplitudes, that the $(n = 4 - 2\epsilon)$ -dimensional reduction of 5-point functions does not differ from the 4-dimensional one in $\epsilon \rightarrow 0$ limit. We would like to emphasize that in a UV finite and gauge invariant fermion loop amplitude, decoupling theorem check is more powerful than the gauge invariance check, in ensuring the correctness of the rational part.

Remark: Fermion loop amplitudes involve the trace of a string of γ -matrices over Dirac indices. After the trace evaluation a fermion loop amplitude is, in general, a collection of the scalar and tensor integrals. It is interesting to note that in a fermion loop diagram containing at maximum one spin-0 particle leg, the amplitude can always be cast in such a form that it does not explicitly depend on the fermion mass. The fermion mass terms appear explicitly after tensor reduction. They are also present in the scalar integrals. In all our fermion loop processes including the one involving a Higgs boson, we have observed this feature.

Chapter 3

Gluon-Gluon Contribution to Di-vector Boson + Jet Production

In this chapter, we will study within the SM, the production of a pair of electroweak vector bosons in association with a hard jet via gluon fusion. In particular, we will consider leading order $gg \rightarrow \gamma\gamma g$, $gg \rightarrow \gamma Zg$, $gg \rightarrow ZZg$ and $gg \rightarrow W^+W^-g$ processes at hadron colliders such as the LHC. These processes proceed via quark loop diagrams at the leading order itself. In fact, the process $gg \rightarrow VV'g$ contributes to the hadronic process $pp \rightarrow VV'j + X$ at the next-to-next-leading order (NNLO) in α_s . Being leading order contributions, these are finite and therefore their contributions towards the hadronic cross sections can be calculated separately. We will compute the hadronic cross sections of these gluon initiated process at various collider centre-of-mass energies and compare them with the corresponding tree-level hadronic processes. We will also make a comparison with the corresponding $gg \rightarrow VV'$ processes. Some important kinematic distributions common to them, will also be given. We will present a detailed study of $gg \rightarrow \gamma Zg$ process which is central to all other processes. We will make comments on the issue of numerical instabilities which commonly arises in such calculations. This chapter is based on the work reported in [71–73].

The search for new physics at the LHC is in progress and the collider is delivering data presently at 8 TeV centre-of-mass energy. The discovery of a fundamental scalar particle (most probably a Higgs boson) of mass around 125 GeV has received a lot of world-wide attention [7–9]. We expect more good news from the experiments

at the LHC before the collider goes for a two year long pause. So far, the SM of particle physics seems to be in excellent agreement with the collected data (more than 10 fb^{-1}). There have been searches for the hints of physics beyond the SM such as supersymmetry, large extra dimensions, etc. But, as of now, there is no clear evidence [12–15]. The process of identifying the discovered fundamental scalar particle as *the Higgs boson* is also continuing. Due to the lack of signals for beyond the SM scenarios, there is a need to look for the SM processes that were not accessible earlier at the Tevatron. Most of such processes have several particles in the final state, and/or occur at the higher order. Calculations of multiparticle processes not only provide tests of the SM, they can also contribute to the background to new physics signals. One such class of processes is multi-vector boson production in association with one or more jets.

At the LHC centre-of-mass energy, the collider has another useful feature. In the proton-proton collisions, the gluon luminosity can be quite significant. It can even dominate over the quark luminosity in certain kinematic domains. Therefore, at the LHC, loop mediated gluon fusion processes can be important. Di-vector boson production via gluon fusion have been studied by many authors [74–80]. We consider another class of processes $gg \rightarrow VV'g$, where V and V' can be any allowed combination of electroweak vector bosons. These processes can be a background to the Higgs boson production as well as new physics scenarios such as the *Technicolor*. At the leading order, these processes receive contribution from quark loop diagrams. The prototype diagrams are displayed in Fig. 3.1. The calculations for the process $gg \rightarrow \gamma\gamma g$ have already been performed [81, 82]. Preliminary results for $gg \rightarrow \gamma Z g$ were presented in [71]. Recently, *Melia et al.* have presented calculations for $gg \rightarrow W^+W^-g$ [83]. In the next section, we give details on the structure of the amplitudes. In section 3.2, we describe the method of calculation and important numerical checks. Numerical results are presented in section 3.3 and a discussion on the issue of numerical instability in our calculations follows in section 3.4.

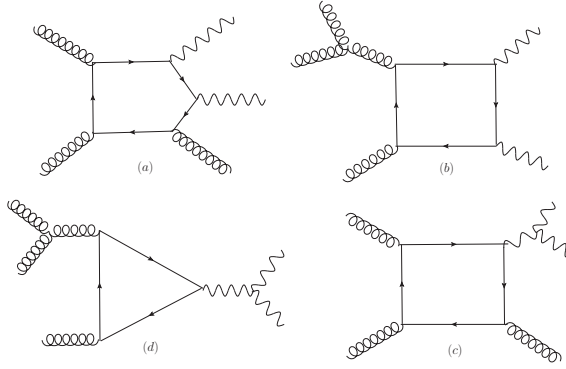


Figure 3.1: The prototype diagrams for the processes $gg \rightarrow VV'g$. The wavy lines represent the appropriate combination of the γ , Z or W boson. The last two classes (c) and (d) are relevant to WWg production only. We do not consider diagrams involving Higgs boson for the ZZg and WWg cases.

3.1 The Amplitudes

The processes $\gamma\gamma g$, γZg and ZZg receive contribution from two main classes of quark loop diagrams – pentagon and box types, as shown in (a) and (b) of Fig. 3.1. The box class of diagrams are due to the triple gluon vertices and they can be further divided into three subclasses. This subclassification has its own physical importance. These subclasses are separately gauge invariant with respect to the electroweak vector bosons. Other diagrams can be obtained by a suitable permutation of external legs. For each quark flavor, there are 24 pentagon-type and 18 box-type diagrams. However, due to Furry’s theorem, only half of the 42 diagrams are independent. The $\gamma\gamma g$ amplitude is purely vector type. In γZg and ZZg cases, the pentagon diagrams give both the vector as well as axial-vector contributions, while the box diagrams give only vector contribution. We work with five massless quark flavors and expect decoupling of the top quark.

In the case of WWg process, instead of a single quark flavor, two quark flavors of a single generation contribute to the above discussed pentagon and box diagrams. To keep the matter simple, for this process, we work with the first two generations of massless quarks. It is expected that the contribution from the third generation will not be significant in low p_T region [80]. There are additional box and triangle

classes of diagrams due to $\gamma/Z WW$ vertex for each quark flavor. These are shown in (c) and (d) of Fig. 3.1. Due to Furry's theorem, the triangle diagrams with γWW coupling do not contribute and only axial-vector part of the triangle diagrams with ZWW coupling contribute to the amplitude. Since the axial-vector coupling of the Z boson to a quark is proportional to the T_q^3 value, the axial-vector contributions from additional triangle and box diagrams, when summed over a massless quark generation, vanish. The vector contribution from the additional box-type diagrams is separately gauge invariant. Because of its color structure, it interferes with the axial-vector part of the pentagon amplitude. We have explicitly checked that its contribution towards the cross section is very small; therefore we have dropped this contribution. Thus, effectively we are left with the ZZg -like contributions for WWg . The Higgs boson interference effects for the cases of ZZg and WWg are ignored in the present calculation. Our one-loop processes, being the leading order processes, are expected to be finite, *i.e.*, free from ultraviolet (UV) and infrared (IR) divergences. The amplitudes of our processes has the following general structure:

$$\begin{aligned}
\mathcal{M}^{abc}(gg \rightarrow VV'g) &= i \frac{f^{abc}}{2} \mathcal{M}_V(VV'g) + \frac{d^{abc}}{2} \mathcal{M}_A(VV'g), \\
\mathcal{M}_V(VV'g) &= -e^2 g_s^3 C_V(VV'g) (\mathcal{P}_V - \mathcal{B}_V), \\
\mathcal{M}_A(VV'g) &= -e^2 g_s^3 C_A(VV'g) (\mathcal{P}_A).
\end{aligned} \tag{3.1}$$

This structure is explained in detail in [71]. Here $\mathcal{M}_{V,A}$ are amplitudes for the vector and axial-vector parts of the full amplitude under consideration. Because of the Bose symmetry $\mathcal{M}_V \rightarrow -\mathcal{M}_V$ under the exchange of any two external gluons while \mathcal{M}_A remains same. \mathcal{B}_V and $\mathcal{P}_{V,A}$ are the box and pentagon contributions from a single flavor (single generation for the WWg case) of quarks. The structure of the amplitude suggests that the vector and axial-vector contributions, in the γZg , ZZg and WWg cases, should be separately gauge invariant. Moreover, due to the color structure when we square the amplitude, the interference between the vector part and the axial-vector part vanishes, *i.e.*,

$$|\mathcal{M}(gg \rightarrow VV'g)|^2 = \left(6|\mathcal{M}_V|^2 + \frac{10}{3}|\mathcal{M}_A|^2 \right). \tag{3.2}$$

Therefore the cross section of any of these processes, is an incoherent sum of the vector and axial-vector contributions. The couplings $C_{V,A}$ for various cases are listed below

and contributions from all the relevant quark flavors (described above) are included appropriately.

$$\begin{aligned}
C_V(\gamma\gamma g) &= \frac{11}{9}, \quad C_A(\gamma\gamma g) = 0, \\
C_V(\gamma Z g) &= \frac{1}{\sin\theta_w \cos\theta_w} \left(\frac{7}{12} - \frac{11}{9} \sin^2\theta_w \right), \\
C_A(\gamma Z g) &= \frac{1}{\sin\theta_w \cos\theta_w} \left(-\frac{7}{12} \right), \\
C_V(ZZ g) &= \frac{1}{\sin^2\theta_w \cos^2\theta_w} \left(\frac{5}{8} - \frac{7}{6} \sin^2\theta_w + \frac{11}{9} \sin^4\theta_w \right), \\
C_A(ZZ g) &= \frac{1}{\sin^2\theta_w \cos^2\theta_w} \left(-\frac{5}{8} + \frac{7}{6} \sin^2\theta_w \right), \\
C_V(WW g) &= \frac{1}{\sin^2\theta_w} \left(\frac{1}{2} \right), \\
C_A(WW g) &= \frac{1}{\sin^2\theta_w} \left(-\frac{1}{2} \right).
\end{aligned} \tag{3.3}$$

We would also like to see if the top quark loop contributes significantly in $\gamma\gamma g$ and $\gamma Z g$ processes. The top quark coupling in these amplitudes can be found in [73].

3.2 Calculation and Numerical Checks

For each class of diagrams, we write down the prototype amplitudes using the SM Feynman rules [52]. The amplitude of all other diagrams are generated by appropriately permuting the external momenta and polarizations in our code. The quark loop traces without γ_5 are calculated in n dimensions, while those with γ_5 are calculated in 4 dimensions using FORM [64]. We do not need any n -dimensional prescription for γ_5 as the pentagon diagrams, which are the only contributions to the axial-vector part of the amplitude, are UV finite and free of anomaly. The amplitude contains one-loop tensor integrals. In the case of pentagon-type diagrams, the most complicated integral is rank-5 tensor integral ($E^{\mu\nu\rho\sigma\delta}$), while for the box-type diagrams, rank-4 tensor integral ($D^{\mu\nu\rho\sigma}$) is the most complicated one. Five point tensor and scalar integrals are written in terms of box tensor and scalar integrals using 4-dimensional Schouten Identity. The box tensor integrals are reduced, in $n = 4 - 2\epsilon$ dimensions, into the standard scalar integrals – A_0 , B_0 , C_0 and D_0 using FORTRAN routines that follows from the reduction scheme developed by Oldenborgh and Vermaseren [63]. We require

box scalar integrals with two massive external legs at the most. The scalar integrals with massive internal lines are calculated using OneLOop library [84]. Because of a very large and complicated expression of the amplitude, we calculate the amplitude numerically before squaring it. This requires numerical evaluation of the polarization vectors of the gauge bosons. We choose the real basis, instead of the helicity basis, for the polarization vectors to calculate the amplitude. This is to reduce the size of the compiled program and the time taken in running the code. We use RAMBO in our Monte Carlo integration subroutine to generate three particle phase space for our processes [85].

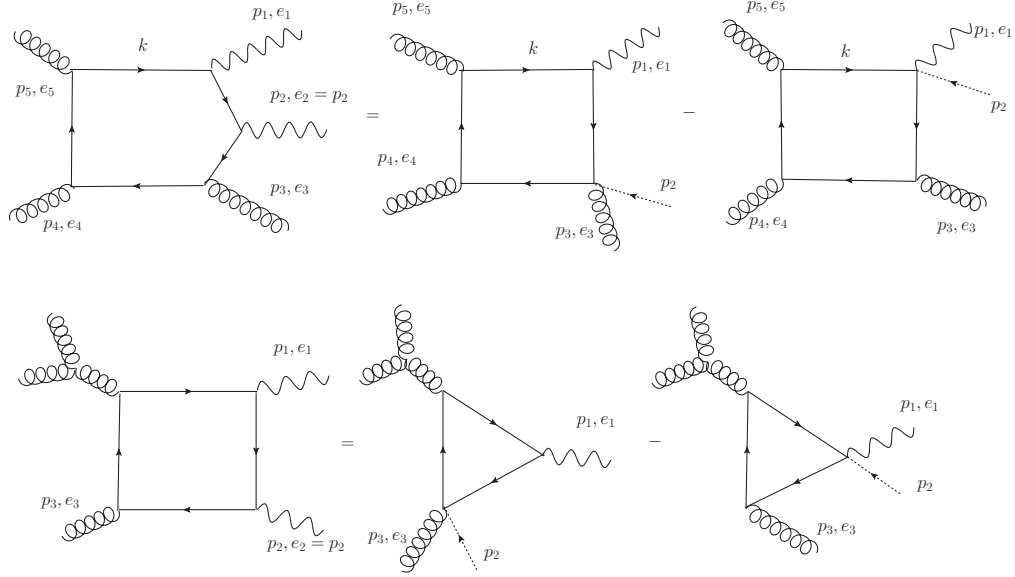


Figure 3.2: Ward identities for $gg \rightarrow \gamma\gamma g$ pentagon and box diagrams. All the momenta are taken incoming. The dotted lines take care of momentum insertion at relevant vertices.

Since the processes $gg \rightarrow VV'g$ are leading order one-loop processes, the general amplitude in Eq. 3.1 should be both UV as well as IR finite. However, individual diagrams may be UV and/or IR divergent. The IR divergence is relevant to only light quark cases. All these singularities are encoded in various scalar integrals. To make UV and IR finiteness checks on our amplitude we have derived all the required scalar integrals and they are listed in the appendix B.2. Following are the details of various checks made on our amplitude given in Eq. 3.1.

1. **UV Finiteness:** The tadpole and bubble scalar integrals (A_0 and B_0) are the only sources of UV singularity in any one-loop amplitude. For the case of massless internal lines, A_0 s do not appear in the tensor reduction. For both the massive and massless quark contributions, we have verified that the amplitude is UV finite. The amplitude of each pentagon diagram has only UV finite tensor integrals. Therefore, each pentagon diagram is UV finite by itself as expected from a naive power counting. The box diagrams individually are not UV finite. Therefore, the cancellation of the divergence in the sum of the box diagrams is an important check. We find that the three classes of box diagrams are separately UV finite.
2. **IR Finiteness:** The diagrams with massless internal quarks have mass singularities. Even in the case of a quark of small mass, like the bottom quark, these diagrams may have large logarithms which should cancel for the finiteness of the amplitude. There can be $\ln^2(m_q^2)$ and $\ln(m_q^2)$ types of mass singular terms. We have checked explicitly that such terms are absent from the amplitude. Moreover, we have verified that the IR finiteness holds for each fermion loop diagram, confirming the general result proved in Sec. 2.3.1.
3. **Ward Identities:** Certain mathematical identities can be obtained by replacing a polarization vector by its 4-momentum in any of the pentagon/box amplitudes. This way a pentagon amplitude can be written as a difference of two (reduced) box amplitudes and also a box amplitude can be written as a difference of two (reduced) triangle amplitudes. For example, if we replace the polarization vector of one of the photons by its 4-momentum in the prototype pentagon and box amplitudes for $gg \rightarrow \gamma\gamma g$, we get

$$\begin{aligned} \mathcal{M}_P(p_1, p_2, p_3, p_4; e_1, e_2 = p_2, e_3, e_4, e_5) &= \mathcal{M}_B(p_1, p_2 + p_3, p_4; e_1, e_3, e_4, e_5) \\ &\quad - \mathcal{M}_B(p_1 + p_2, p_3, p_4; e_1, e_3, e_4, e_5), \end{aligned} \tag{3.4}$$

$$\begin{aligned} \mathcal{M}_B(p_1, p_2, p_3; e_1, e_2 = p_2, e_3, e_{45}) &= \mathcal{M}_T(p_1, p_2 + p_3; e_1, e_3, e_{45}) \\ &\quad - \mathcal{M}_T(p_1 + p_2, p_3; e_1, e_3, e_{45}). \end{aligned} \tag{3.5}$$

Here e_i s are polarization vectors of the gauge bosons and e_{45} denotes the triple gluon vertex attached to the box/triangle diagram. These identities are shown diagrammatically in Fig. 3.2. We have verified them numerically. These Ward identities are important checks on individual diagrams and a set of these identities can also be utilized for a systematic study of numerical instabilities in the tensor reduction, near exceptional phase space points. An exceptional phase space point corresponds to the vanishing of a partial sum of the external momenta.

4. **Gauge Invariance:** As we have seen, because of the color structure, the vector and axial-vector parts of the amplitude do not interfere and they are separately gauge invariant. The vector part of the amplitude has gauge invariance with respect to the three gluons and the electroweak bosons. This has been checked by replacing the polarization vector of any of these gauge particles by its momentum ($\varepsilon^\mu(p_i) \rightarrow p_i^\mu$) which makes the amplitude vanish. As one would expect the pentagon and the three classes of box contributions are separately gauge invariant with respect to the electroweak bosons. For each gluon, one of the three classes of box amplitudes is separately gauge invariant and further cancellation takes place among the pentagon and the other two box contributions. The axial-vector part of the amplitude is separately gauge invariant with respect to all the three gluons and the photon. We verify that due to explicit breaking of the chiral symmetry in the presence of a quark mass, the axial-vector part of the amplitude, in γZg , ZZg and WWg cases, vanishes on replacing the Z/W boson polarization by its 4-momentum only in the $m_q \rightarrow 0$ limit.
5. **Decoupling of heavy quarks:** As a consistency check, we have also verified that the vector and axial-vector parts of the amplitude vanish in the large quark mass limit [70]. This feature of the amplitude is very closely related to its UV structure. The decoupling theorem holds for each pentagon amplitude and also for each class of box amplitudes. For the process $gg \rightarrow \gamma Zg$, in Fig. 3.3, we have plotted the ratio of the squared-amplitudes for five and six quark flavor contributions as a function of the top quark mass. The phase space point corresponds to a fixed partonic centre-of-mass energy, $\sqrt{s} = 8M_Z$. The

vector and axial-vector contributions are plotted separately. The $m_t = 4M_Z$ corresponds to the scale above which the top quarks in the loop cannot go on-shell. Various slope changes shown in this plot correspond to the possibilities of producing one or more final state particles via on-shell $t\bar{t}$ annihilation.

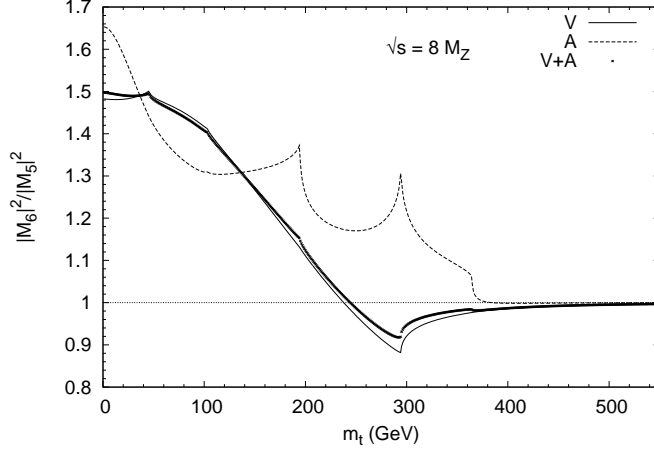


Figure 3.3: Decoupling of the top quark in $gg \rightarrow \gamma Z g$ amplitude. The vector and axial-vector contributions are shown separately.

3.3 Numerical Results

Based on the procedure outlined above, we can now compute the hadronic cross sections and examine various features of our processes. As we have already mentioned, we compute amplitudes numerically using the real polarization vectors of the gauge bosons. There are 32 polarized amplitudes for the case of $\gamma\gamma g$, 48 for the case of $\gamma Z g$ and 72 for the cases of ZZg and WWg . Given the number of diagrams, the number of polarization combination and the length of the amplitude, the computation becomes very time consuming. Each phase space point evaluation takes about 1.3 seconds on a single machine that we use. We use ifort compiler on Intel Xeon CPU 3.20GHz machines. We, therefore, run the code in a parallel environment using AMCI package, a PVM implementation of the VEGAS algorithm [86, 87]. We have used more than 30 cores to run the code in the parallel environment. Still it takes more than 12 hours

to get suitable cross section which includes both the massive and massless quark contributions. We will now divide our numerical results into two parts. In the first part, we will do a comparative study of the γZg , ZZg and WWg processes. Also we will update the results for $\gamma\gamma g$ at 8 TeV LHC. The second part will deal with the numerical results for the γZg process in greater detail.

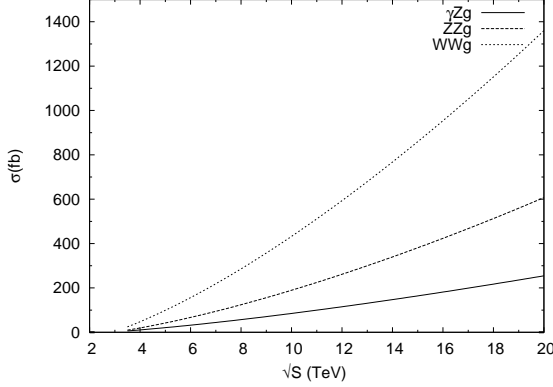


Figure 3.4: Variation of the cross sections with the collider centre-of-mass energy for $gg \rightarrow VV'g$.

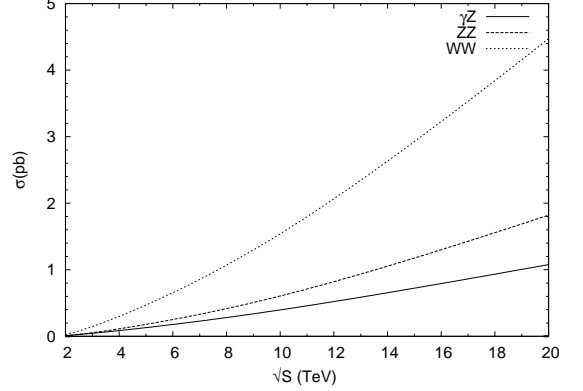


Figure 3.5: Variation of the cross sections with the collider centre-of-mass energy for $gg \rightarrow VV'$.

3.3.1 Numerical results for $VV'g$

Since the processes γZg , ZZg and WWg have both the vector and the axial-vector contributions, we can put them in one class and study their relative behavior. Their results do not include the top quark-loop contribution. The comparative study, presented in this section, uses following kinematic cuts:

$$p_T^{\gamma,Z,W,j} > 30 \text{ GeV}, |\eta^{\gamma,Z,W,j}| < 2.5, R(\gamma, \gamma/j) > 0.6, \quad (3.6)$$

where $R(\gamma, j) = \sqrt{\Delta\eta_{\gamma j} + \Delta\phi_{\gamma j}}$, is the isolation cut between the photon and the jet. In addition to this, we have chosen the factorization and the renormalization scales as $\mu_f = \mu_r = p_T^{\gamma/Z/W}$, as appropriate. In this section, we have used CTEQ6M parton distribution functions to obtain the results [88]. In Fig. 3.4, we present the results of the cross section calculation for the three processes. We note that at typical LHC energy, the cross sections are of the order of 100 fb. For example, at the centre-of-mass

energy of the 8 TeV, the cross sections are 46.7 fb, 95.5 fb, and 225.2 fb, respectively for the γZg , ZZg and WWg production processes. Therefore, one may expect a few thousand of such events at the end of the present run. But a W/Z boson is observed through its decay channels. If we consider the case when all the W/Z bosons are seen through their decays to the electron/muon only, then, with 20 fb^{-1} integrated luminosity, the number of events for these processes will be approximately 60, 10, and 220 respectively. However, if we allow one of the W/Z boson to decay hadronically, then the number of events would increase significantly. At the 14 TeV centre-of-mass energy, the numbers will be about a factor of three larger. The relative behavior of cross sections of the three processes, as the centre-of-mass energy varies, is quite similar to the case of di-vector boson production via gluon fusion as shown in Fig. 3.5. This common behavior is mainly due to the relative couplings of the processes listed above in Eq. 3.3. We find that at 14 TeV the cross sections for our processes are 20 – 30% of those for the corresponding di-vector boson production (without jet) processes. We can also compare the contributions of these loop processes with those of the corresponding tree-level processes. We find that the processes $gg \rightarrow \gamma Zg, WWg$ make about 4 – 5% contribution to the processes $pp \rightarrow \gamma Zj, WWj$, while $gg \rightarrow ZZg$ makes a contribution of about 10 – 15% to the $pp \rightarrow ZZj$ process. Here ‘ j ’ stands for a jet. This is quite similar to the case of the di-vector boson production. Tree-level estimates are obtained using MadGraph [89].

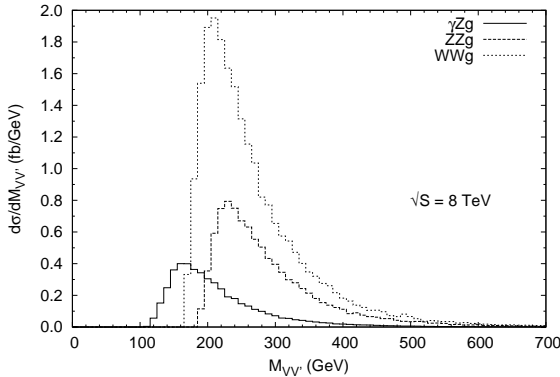


Figure 3.6: Invariant mass distributions of the pair of vector boson at 8 TeV, for $gg \rightarrow VV'g$.

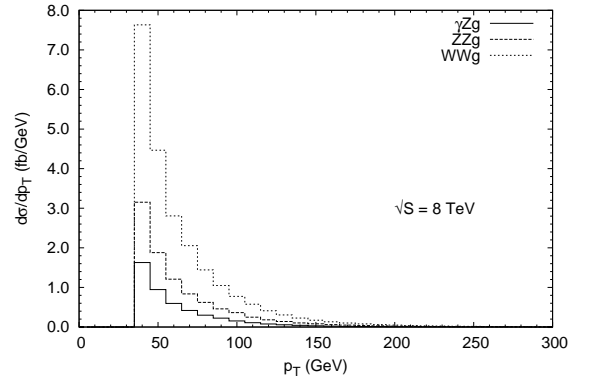


Figure 3.7: Transverse momentum distributions of the gluon jet at 8 TeV, for $gg \rightarrow VV'g$.

We have also compared our results for the WWj production case with those of *Melia et al.* [83]. Though they have considered the leptonic decays of the W bosons and the kinematic cuts, choice of scales and parton distributions etc. are quite different, the percentage contribution of gluon-gluon channel as compared to the LO cross section is same within the allowed range of uncertainty, *i.e.*, 4 – 5%. The values of the cross section are more strongly dependent on the values of parameters and kinematic cuts; still two results are similar if we take into account quoted uncertainties and branching ratios. The contribution of these gluon fusion processes can be even larger in appropriate kinematic regime.

We now discuss few kinematic distributions at 8 TeV collider centre-of-mass energy. These distributions remain same, characteristically, at 14 TeV centre-of-mass energy. The invariant mass distributions for the pair of vector boson are shown in Fig. 3.6. The positions of the peaks are related to the masses of the vector bosons in each case. Of course, the WW invariant mass cannot be measured experimentally. In Fig. 3.7, the transverse momentum distributions for gluon jet is given for the three processes. The major contribution to the cross section comes from low p_T region, as we expect. The cross section is very sensitive to the p_T cut on gluon as it is radiated from one of the incoming gluons in the box diagrams.

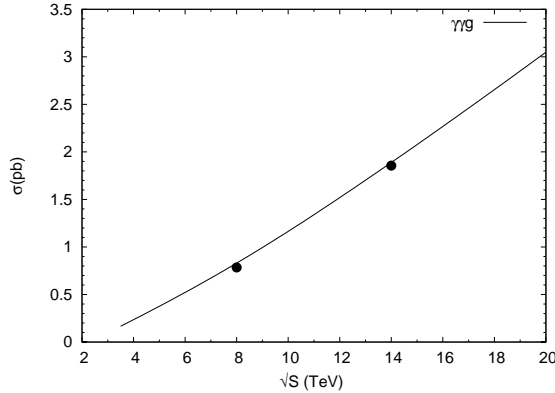


Figure 3.8: The collider energy dependence of the cross section for $gg \rightarrow \gamma\gamma g$.

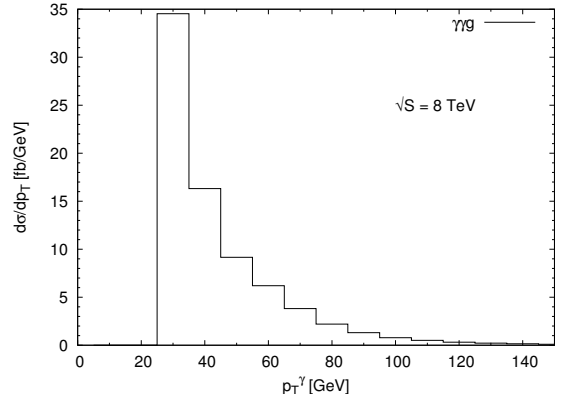


Figure 3.9: Transverse momentum distributions of the photon in $gg \rightarrow \gamma\gamma g$.

The variation of the hadronic cross section with the collider centre-of-mass energy, for $\gamma\gamma g$ production via gluon fusion, is given in Fig. 3.8. The result is with the above kinematic cuts and choices except that, $p_T^\gamma > 20$ GeV. We reconfirm the importance

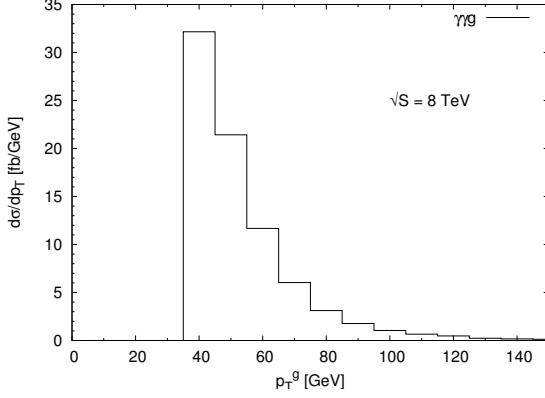


Figure 3.10: Transverse momentum distribution of the gluon jet in $gg \rightarrow \gamma\gamma g$.

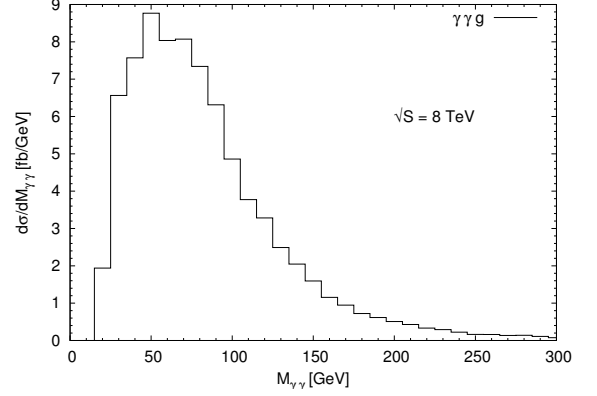


Figure 3.11: Invariant mass distribution of the two photons in $gg \rightarrow \gamma\gamma g$.

of $gg \rightarrow \gamma\gamma g$ process at the LHC. We have checked that the top quark contribution to the cross section is very small. Therefore the results include light quark loop contributions only. The cross section at the 8 TeV (14 TeV) centre-of-mass energy is about 0.78 pb (1.86 pb), leading to several hundred (thousand) events with even 1 fb^{-1} of integrated luminosity. Few important kinematic distributions related to this process are given at 8 TeV LHC in Figs. 3.9, 3.10 and 3.11.

3.3.2 Numerical results for $\gamma Z g$

Now we will have a detailed discussion on the results for the $gg \rightarrow \gamma Z g$ process. We first study the importance of the diagrams with the top quark in the loop. In Fig. 3.12, we see that the contribution of the top quark ($m_t = 175 \text{ GeV}$) to the hadronic cross section is negligible. We also see a knee in the plot at $m_t = \frac{M_Z}{2}$. This corresponds to the Z boson production via $t\bar{t}$ annihilation. The top quark decouples at around 100 GeV. We have, therefore, not included its contribution in our results presented below. The run time of our code is also reduced by 50%. It is not surprising that the top quark decouples at such a low value for our processes. This is simply because there are four/five quark propagators in each box/pentagon diagram, leading to a large power of the top quark mass in the denominator.

We can divide our numerical results that are presented in this section into two

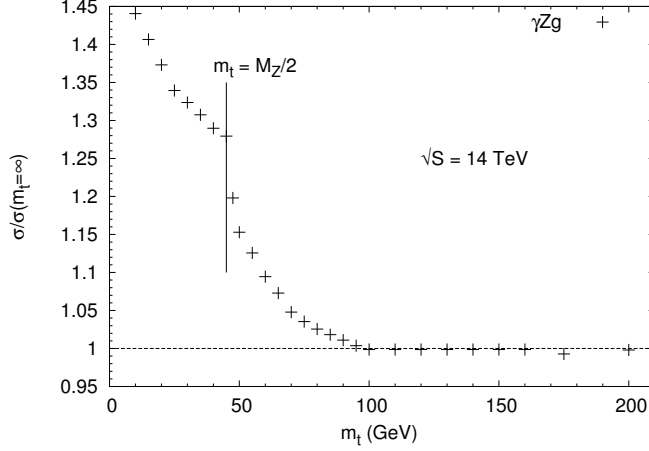


Figure 3.12: Decoupling of the top quark in the cross section calculation of $gg \rightarrow \gamma Z g$.

categories. We first discuss theoretical results, related to the structure of the amplitude, keeping the Z boson on-shell. Theoretical results presented below include following kinematic cuts:

$$p_T^j > 30 \text{ GeV}, p_T^{\gamma, Z} > 20 \text{ GeV}, |\eta^{\gamma, Z, j}| < 2.5, R(\gamma, j) > 0.6. \quad (3.7)$$

We have chosen the factorization and the renormalization scales as $\mu = \mu_f = \mu_r = E_T^Z (= \sqrt{M_Z^2 + (p_T^Z)^2})$, the transverse energy of the Z boson. Results are obtained using CTEQ6M PDFs [88]. In Fig. 3.13, we give the dependence of the cross section on the collider centre-of-mass energy to see the effect of a large gluon luminosity at higher energies. We have already seen that the vector and axial-vector parts of the amplitude are separately gauge invariant. Their contributions towards the cross section are also included in the figure. The axial-vector contribution is only about 10% of the total cross section; this contribution comes from the pentagon class of diagrams. Although the box-contribution to the cross section is not separately gauge invariant with respect to the gluons, it is gauge invariant with respect to the γ and the Z boson. We find that more than 70% of the total cross section is due to the box-amplitude only, see Fig. 3.14. The scale variation of the cross section about the central value $\mu_0 = E_t^Z$, is shown in Fig. 3.15. On increasing the scale by a factor of 2, the cross section decreases by about 25%; it increases by about 40% on decreasing the scale by a factor of 2. These large variations are expected because our calculation is

effectively LO as far as the μ dependence is concerned. We see that the cross section falls as we increase the scale μ . This is because an increase in the factorization scale increases the cross section due to the increase in the gluon luminosity; but an increase in the renormalization scale decreases the cross section because of the decrease in the value of $\alpha_s(\mu)$. When we increase both the scales at the same time, the effect of the change in the renormalization scale is stronger. It leads to an overall decrease in the cross section with the increase in the scale μ .

Next, we come to the discussion on our phenomenological results. These results include various kinematic distributions related to the final state particles. For phenomenological results, we work in the narrow width approximation. We allow the Z boson to decay into two leptons in the phase space. In this case, the kinematic cuts are

$$p_T^j > 30 \text{ GeV}, p_T^\gamma > 15 \text{ GeV}, p_T^l > 10 \text{ GeV}, |\eta^{\gamma,l,j}| < 2.5, R(i_1, i_2) > 0.4. \quad (3.8)$$

Here i_1 and i_2 may represent any of the $\gamma/l/j$. For convenience, we have chosen the scale $\mu = \mu_f = \mu_r = M_Z$. In Fig. 3.16, we give the cross section variation in the range of 8 TeV to 14 TeV centre-of-mass energies using both the CTEQ6l1 and CTEQ6M PDFs. These numbers do not include the branching ratio of $Z \rightarrow l^+l^-$. In particular, the cross sections with CTEQ6l1 (CTEQ6M) parton distributions, are 65.4 (53.0) fb and 202.4 (154.3) fb at 8 TeV and 14 TeV centre-of-mass energies respectively. With these cross sections, number of $gg \rightarrow \gamma Z g$ events can be as large as 20000 at the 14 TeV LHC, with 100 fb^{-1} integrated luminosity. However, to observe these events, one may have to look at $Z \rightarrow l^+l^-$ decay channel; here l can be an electron/muon. So including the branching ratios, one may expect more than 1000 events for $gg \rightarrow \gamma Z(\rightarrow l^+l^-)g$ process. The transverse momentum and rapidity distributions for the final state particles are shown in Figs. 3.17-3.22 at the 8 TeV centre-of-mass energy. We have given normalized distributions as they remain same for different choices of parton distributions and/or scales. These distributions are characteristically similar at different collider centre-of-mass energies, but at higher energies contribution coming from high p_T /rapidity region grows, while low p_T /rapidity region contribution goes down. We note that p_T^j is softer as compared to p_T^γ . It is because the cross section is dominated by the box class of diagrams and in these diagrams, the gluon is

emitted as a bremsstrahlung radiation, see Fig. 3.14. Due to the same reason, *i.e.*, the gluon is emitted more collinearly, the rapidity distribution of the gluon jet is broader as compared to that of the photon. The lepton- p_T distribution peaks around $M_Z/2$. On the other hand the rapidity distribution of the lepton is more central compared to the η^γ distribution.

\sqrt{S} (TeV)	$p_T^{\gamma,min}$ (GeV)	σ^{LO} (pb)	σ^{NLO} (pb)	$\sigma_{gg}^{\text{NNLO}}$ (fb)	$\sigma_{gg}^{\text{NNLO}}/(\sigma^{\text{NLO}} - \sigma^{\text{LO}})$ (%)	$\sigma_{gg}^{\text{NNLO}}/\sigma^{\text{NLO}}$ (%)
8	30	2.202	3.391	46.05 (38.25)	3.87 (3.22)	1.36 (1.13)
	50	1.144	1.744	30.49 (25.61)	5.08 (4.27)	1.75 (1.47)
14	30	4.868	7.722	158.72 (124.48)	5.56 (4.36)	2.06 (1.61)
	50	2.608	4.158	109.92 (86.61)	7.09 (5.59)	2.64 (2.08)
35	30	14.973	23.548	854.09 (606.07)	9.96 (7.07)	3.63 (2.57)
	50	8.220	13.514	607.35 (438.88)	11.47 (8.29)	4.49 (3.25)

Table 3.1: Cross sections for the production of $pp \rightarrow \gamma Z j + X$ at various collider centre-of-mass energies. We use CTEQ6l1 PDF set at the LO and CTEQ6M PDF set at the NLO. The NNLO predictions are with CTEQ6l1(CTEQ6M) parton distribution. The factorization and renormalization scales are set to, $\mu_f = \mu_r = \mu_0 = M_Z$.

We have also compared results of this NNLO calculation with the LO and NLO predictions for $pp \rightarrow \gamma(Z \rightarrow \nu\bar{\nu})j + X$ [90]. The LO and NLO results are obtained using parton-level next-to-leading order program MCFM¹. The comparison is presented after removing the branching ratios in Table 3.1. The table includes results at three different centre-of-mass energies and for two values of the $p_T^{\gamma,min}$. We have included the centre-of-mass energy of 35 TeV, as it is proposed for the HE-LHC collider. The other kinematic cuts are: $p_T^j > 30$ GeV, $p_T^{miss} > 30$ GeV, $|\eta^{\gamma,j}| < 2.5$, $R(\gamma, j) > 0.4$. This table illustrates two facts – 1) the fraction of NNLO events increases with the increase in $p_T^{\gamma,min}$, 2) the NNLO process becomes more important as we increase the centre-of-mass energy. There is an increase in the NNLO fraction with an increase in

¹<http://mcfm.fnal.gov/>

$p_T^{\gamma,min}$ because, in the NLO events, photon is emitted from a quark line; a larger $p_T^{\gamma,min}$ suppresses the NLO contribution more than the NNLO contribution. In Fig. 3.23, we have compared the normalized p_T^{γ} -distributions at the NLO and NNLO, leading to the same conclusion. The importance of the NNLO process is more at higher centre-of-mass energy simply because of the increase in the gluon-gluon luminosity. At 8 TeV, the scale uncertainties in the NLO calculations, on changing the scale by a factor of two in both the directions of the central value, are in the range 7 – 8%, while the same in the NNLO calculations is 30 – 50%.

3.4 The Issue of Numerical Instability

Like other calculations of our types, we have also faced the issue of numerical instability in our calculations for certain phase space points. This is a well known issue in the reduction of one-loop tensor integrals of higher rank and higher points. The issue of numerical instability may also occur in the evaluation of the scalar integrals. We have taken care of this by using the OneLOop implementation of the scalar integrals. We face numerical instabilities primarily in the evaluation of pentagon tensor integrals. This is related to the inaccurate evaluation of the Gram determinants in those phase space regions where the linear independence of external momenta (modulo 4-momentum conservation) is compromised, *i.e.*, near the exceptional phase space points. The inverse Gram determinants appear in the reduction of tensor integrals. Near exceptional phase space points, the Gram determinants become very small and give rise to numerical problems. These numerical problems are result of a loss of precision due to the large cancellations. This problem can be handled in several ways. One way is to use higher precision for the tensor reduction and for the evaluation of scalar integrals. This certainly reduces the number of exceptional phase space points but the code becomes enormously slow. Another approach could be to use special expressions for the tensor reduction, near such phase space points [91]. It is important to mention here that none of these two approaches cure the problem of numerical instability completely [92]. A more economic and convenient way to proceed in this situation is to judiciously ignore the contributions from such phase space points. This one can do because we are not doing precision calculations and

exceptional phase space points are unlikely to give a significant contribution to the total cross section. We perform a gauge invariance (GI) test on the full amplitude for each phase space point. In practice, we introduce a small cut-parameter δ , and under GI we check, if $|\mathcal{M}|^2 < \delta$ holds true for each phase space point. We ignore all those points which fail to pass this test. In our code we have set $\delta = 10^{-6}$. With this value of δ and other kinematic cuts, the fraction of points ignored is below 2%. However, with higher p_T cut and/or less stringent cut on the δ , the number of such points can drop to a level of 0.01%. Our Monte Carlo phase space integration subroutine is based on the VEGAS algorithm. We believe that the adaptive nature of the VEGAS algorithm also affects the percentage of exceptional phase space points that one may come across in such calculations. We sample about 0.4-0.5 million phase space points to obtain the numerical results. Given the volume of phase space, the number of exceptional phase space points is small and it is reasonable to assume that the cross section is not dominated by this region of phase space. We find that our result depends on this cut very weakly and remains quite stable over the range of $10^{-4} - 10^{-12}$ for the choice of the cut-parameter. This can be seen in Fig. 3.24. This stability reflects that the exceptional phase space points are few and make small contribution at the level of total cross section.

We have also checked our results for the cross section calculation by implementing a set of Ward identity tests and its sensitivity on δ -like cut-parameter. Examples of these identities are given in Eqs. 3.4 and 3.5. However, these identities should not be implemented in a straightforward manner. For example, the pentagon ward identity in Eq. 3.4 can be implemented in the following form,

$$(1 - \frac{\mathcal{M}_P}{\mathcal{M}_B^1 - \mathcal{M}_B^2}) < \delta. \quad (3.9)$$

Numerically, due to the Ward identity, the ratio $\mathcal{M}_P/(\mathcal{M}_B^1 - \mathcal{M}_B^2) \sim \mathcal{O}(1)$. In Eq. 3.9, we compare two numbers of $\mathcal{O}(1)$, which gives precise information on the order of cancellation within the working precision. Although the total cross section is quite stable, various distributions, specially the rapidity distributions near the edges, are quite sensitive to the variation in δ . Edges of distributions define the region where exceptional phase space points may lie. Therefore, the inaccuracy of the distributions at the edges of the phase space is not surprising. We have seen that the exceptional

phase space points may defy the GI and/or Ward identity tests sometimes. One can make these δ -like cuts more stringent to get more reliable distributions. One can also identify exceptional phase space points at the level of Gram determinants which may be more economical. Phase space points corresponding to a large cancellation in the Gram determinants can be ignored without putting stringent cuts on δ and again leading to more reliable distributions. A method to implement this criterion is discussed in [92].

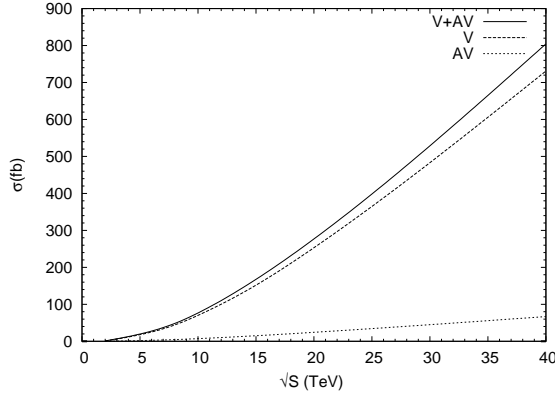


Figure 3.13: The vector and axial-vector contributions of the hadronic cross section for $gg \rightarrow \gamma Z g$.

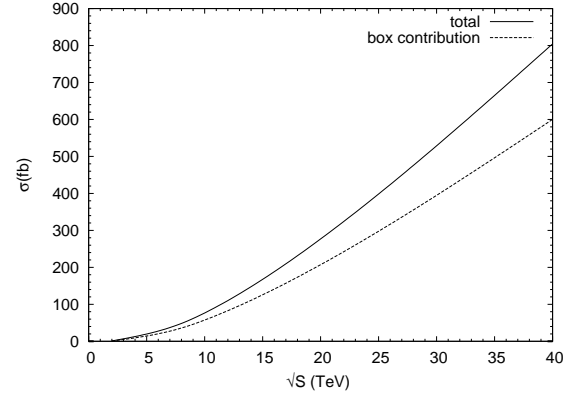


Figure 3.14: Contribution of the box-amplitude towards the hadronic cross section for $gg \rightarrow \gamma Z g$.

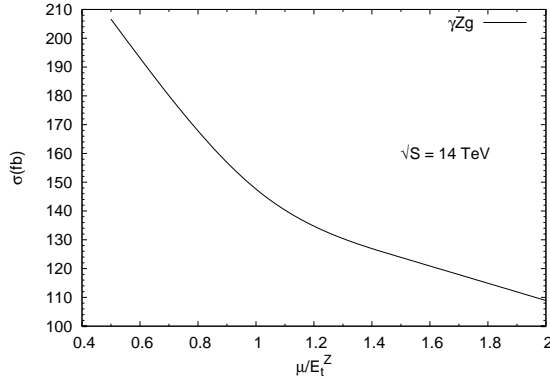


Figure 3.15: Variation of the cross section for $gg \rightarrow \gamma Z g$ with the scale, $\mu = \mu_r = \mu_f$ at 14 TeV.

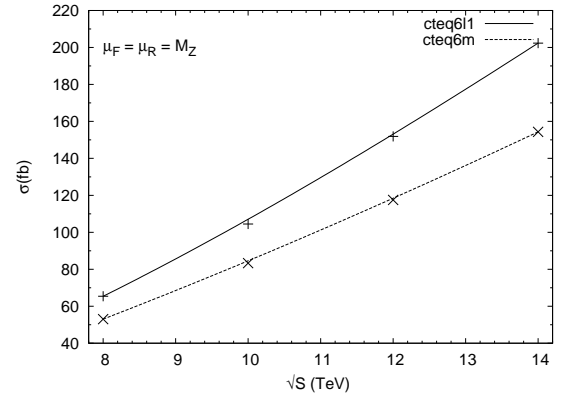


Figure 3.16: Dependence of the cross section on the collider energy, for $gg \rightarrow \gamma Z(\rightarrow l^+ l^-) g$.

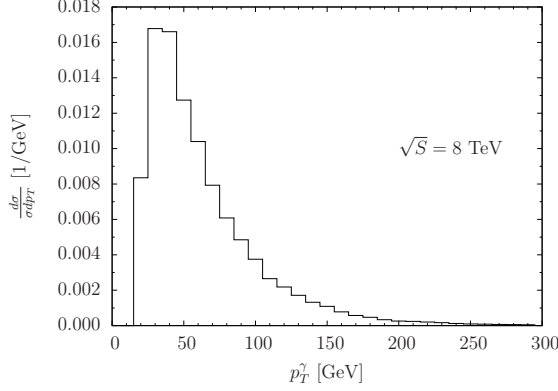


Figure 3.17: Transverse momentum distribution of the photon at 8 TeV centre-of-mass energy in $gg \rightarrow \gamma Z(\rightarrow l^+ l^-)g$.

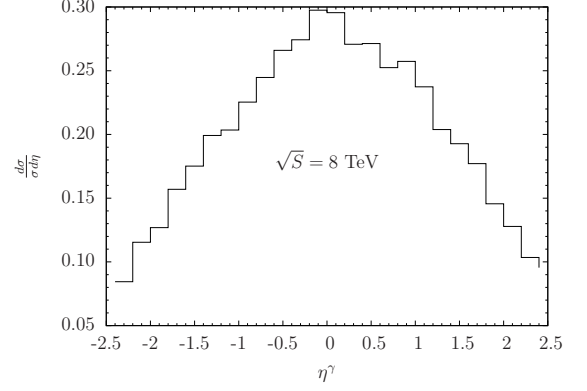


Figure 3.18: Rapidity distribution of the photon at 8 TeV centre-of-mass energy in $gg \rightarrow \gamma Z(\rightarrow l^+ l^-)g$.

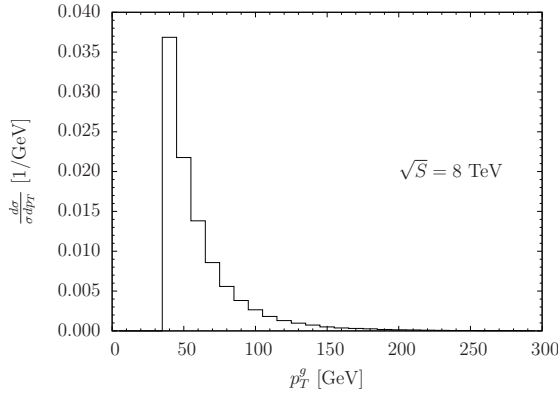


Figure 3.19: Transverse momentum distribution of the gluon jet at 8 TeV centre-of-mass energy in $gg \rightarrow \gamma Z(\rightarrow l^+ l^-)g$.

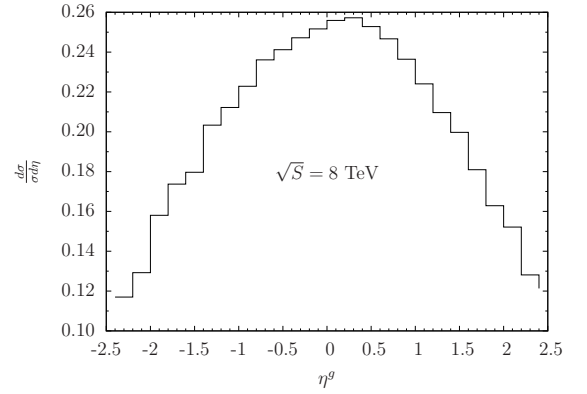


Figure 3.20: Rapidity distribution of the gluon jet at 8 TeV centre-of-mass energy in $gg \rightarrow \gamma Z(\rightarrow l^+ l^-)g$.

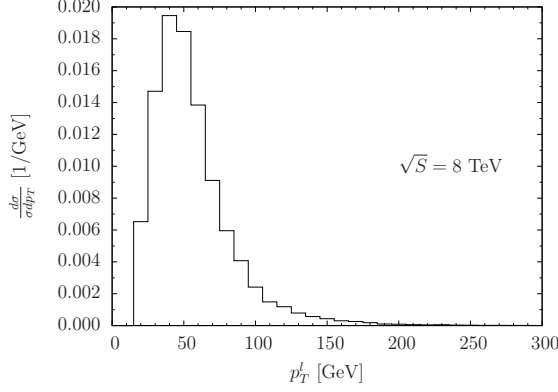


Figure 3.21: Transverse momentum distribution of lepton at 8 TeV centre-of-mass energy in $gg \rightarrow \gamma Z(\rightarrow l^+ l^-)g$.

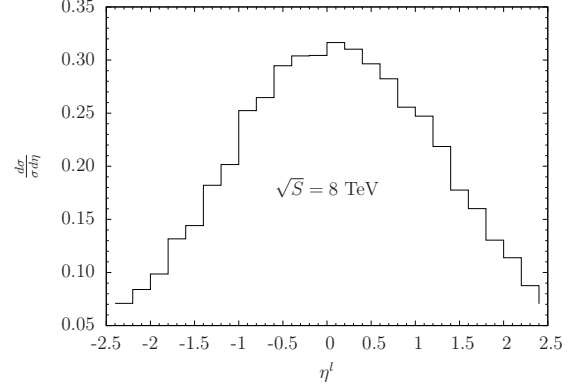


Figure 3.22: Rapidity distribution of lepton at 8 TeV centre-of-mass energy in $gg \rightarrow \gamma Z(\rightarrow l^+ l^-)g$.

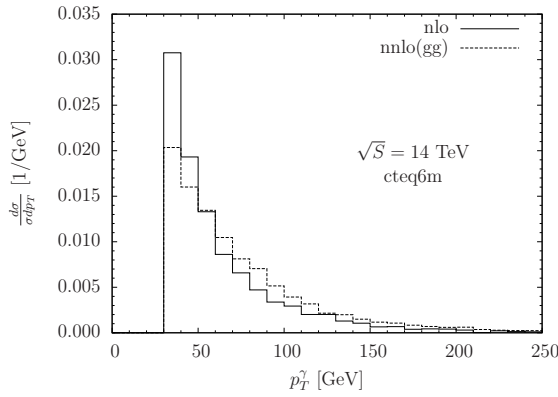


Figure 3.23: A comparison of the normalized p_T -distributions of γ at NLO and NNLO. The NLO distribution is obtained using MCFM.

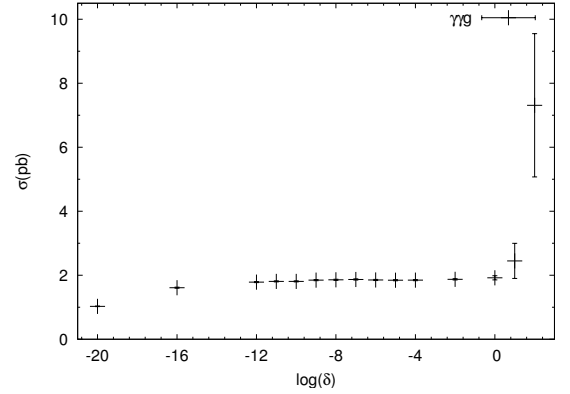


Figure 3.24: Dependence of the total cross section on GI test cut-parameter (δ) for $gg \rightarrow \gamma\gamma g$ at 14 TeV. The error bars are shown explicitly.

Chapter 4

Production of KK-gravitons with a Boson via Gluon Fusion

In this chapter, we will consider the associated production of an electroweak boson and the KK-graviton modes via gluon fusion in the ADD model. In particular, we will study leading order $gg \rightarrow HG_{\text{KK}}$, $gg \rightarrow \gamma G_{\text{KK}}$ and $gg \rightarrow ZG_{\text{KK}}$ processes. Like the SM processes discussed earlier, these processes also proceed via quark loop diagrams at the leading order and are finite. These processes contribute to the hadronic processes $pp \rightarrow BG_{\text{KK}} + X$, at the NLO in α_s , where $B \in \{H, \gamma, Z\}$. We will calculate the inclusive cross sections of these gluon channel processes at the LHC and discuss some important kinematic distributions. In this chapter, by inclusive we mean the contribution from all the kinematically accessible KK-modes. We will also study the dependence of these results on the model parameters δ and M_S . This chapter is based on the work reported in [93–95]. A brief overview of the model is given in Sec. 1.2.

Like the other new physics scenarios, the searches for the model of large extra dimensions or the ADD model is also continuing at the LHC. With the 7 TeV LHC data, the bounds on the model parameters have also improved quite significantly [96–103]. In the context of the ADD model, studies of processes involving the exchange of KK-gravitons and those in which KK-gravitons are produced directly, have been reported for both the Tevatron and the LHC [104–112]. Due to a large gluon flux available at the LHC, the gluon initiated processes can be quite important. In this regard, we have investigated the KK-graviton production in association with a boson

($H/\gamma/Z$) via gluon fusion. Unlike the cases of γ/ZG_{KK} production, the $q\bar{q}$ initiated tree-level HG_{KK} production process has very small cross section due to a vanishingly small coupling of the Higgs boson with light quarks. Even with a non-zero bottom quark mass, the tree-level cross section can be at best of the order 10^{-3} fb at the LHC. The contribution of the gluon-gluon channel is, therefore, expected to be relatively more important for the HG_{KK} production at the LHC. The situation is analogous to the single Higgs boson production in the SM. There too the $gg \rightarrow H$ channel dominates the hadronic cross section. The rest of the chapter is organized as follows: In the next section, we give some details on the structure of the amplitudes. Various checks on our amplitudes and the method of computation are described in section 4.2 and 4.3. Numerical results are presented in section 4.4. An interesting issue related to the ZG_{KK} amplitude calculation is added in the end.

4.1 The Structure of Amplitudes

At the leading order, the process $gg \rightarrow BG_{\text{KK}}$ proceeds via quark loop diagrams. The allowed vertices and their Feynman rules, in the ADD model, are listed in Ref. [48]. Depending upon the coupling of the KK-graviton with the standard model particles, there are three classes of diagrams: a triangle class of diagrams due to *quark*–*boson*–*graviton* coupling, another triangle class of diagrams due to *boson*–*graviton* coupling and the box class of diagrams due to *quark*–*graviton* coupling. The prototype diagram in each class is shown in Fig. 4.1. Other diagrams are obtained just by appropriate permutations of the external legs. There are total six box and twelve triangle diagrams for each quark flavor. However, due to the charge-conjugation property of the fermion loop diagrams, only half of the diagrams are independent. Since the coupling of the Higgs boson with quarks is proportional to the quark masses, in the $gg \rightarrow HG_{\text{KK}}$ case, we consider only bottom and top quark contributions. For a given massive quark in the loop, the HG_{KK} amplitude has the following structure:

$$\begin{aligned}\mathcal{M}_q^{ab}(gg \rightarrow HG_{\text{KK}}) &= \frac{1}{8} y_q g_s^2 \kappa \left(\frac{\delta^{ab}}{2} \right) \mathcal{A}(m_q), \\ \mathcal{A}(m_q) &= [2 \mathcal{A}_{tri}(m_q) - \mathcal{A}_{box}(m_q)].\end{aligned}\tag{4.1}$$

Here the Yukawa coupling, $y_q = \frac{1}{2}g_w(m_q/M_W)$ and $\kappa = \sqrt{2}/M_P$. Furthermore, a and b are color indices of the two gluons. \mathcal{A}_{tri} is the net contribution from the two triangle classes of diagrams, shown in Figs. 4.1 (a) and (b).

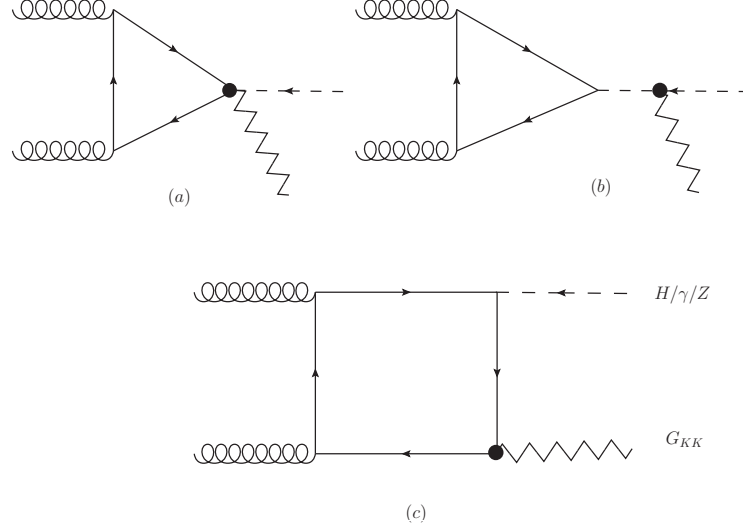


Figure 4.1: Prototype Feynman diagrams for $gg \rightarrow H/\gamma/Z + G_{KK}$ in the ADD model.

For $gg \rightarrow \gamma G_{KK}$ case, we find that the amplitudes of the diagrams, related by charge-conjugation, are equal and opposite to each other. This implies that at the LO,

$$\mathcal{M}(gg \rightarrow \gamma G_{KK}) = 0. \quad (4.2)$$

By introducing charge-conjugation transformation of the KK-graviton field and using charge-conjugation properties of the gluon and photon fields, it can be shown that the γG_{KK} amplitude does vanish at the LO. This is just an implication of the extension of Furry's theorem in the presence of gravitons, photons and gluons. The graviton field is considered even under charge-conjugation as it couples with the energy-momentum tensor only. This, we have explicitly verified using the ADD model Lagrangian [94]. This result would remain valid to all orders if only QED and/or QCD radiative corrections are included. In the presence of the weak interaction, this result may not hold to all orders.

The $gg \rightarrow Z G_{KK}$ amplitude has both the vector and axial-vector contributions coming from the Z boson coupling to the quarks. The vector part of the amplitude

is similar to the γG_{KK} amplitude and therefore at the LO, the process receives contribution only from the axial-vector part of the amplitude. For a given quark flavor in the loop, the amplitude has the following structure:

$$\mathcal{M}_q^{ab}(gg \rightarrow ZG_{\text{KK}}) = g_z g_s^2 \kappa \left(\frac{\delta^{ab}}{2} \right) c_A^q \mathcal{A}(m_q), \quad (4.3)$$

$$\mathcal{A}(m_q) = \mathcal{A}_{tri}(m_q) - \mathcal{A}_{box}(m_q). \quad (4.4)$$

Here $g_z = g_w/\cos\theta_w$ and $c_A^q = -T_q^3/2$. \mathcal{A}_{tri} includes the contributions from both types of triangle diagrams. We find that due to the nature of KK-graviton coupling with quarks, both the triangle and box diagrams are linearly divergent and therefore they will give rise to anomalous contributions to the amplitude. Of the six quark flavours, we treat the u, d, s , and c quarks as massless. Since the amplitude of the process is proportional to T_q^3 value, the first two generations do not contribute. Therefore, the full amplitude, including the contributions from all the six quarks, is

$$\sum_q \mathcal{M}_q^{ab}(gg \rightarrow ZG_{\text{KK}}) = -\frac{1}{4} g_w g_s^2 \kappa \left(\frac{\delta^{ab}}{2} \right) [\mathcal{A}(m_t) - \mathcal{A}(m_b)]. \quad (4.5)$$

We note that the cross section is of $\mathcal{O}(\alpha_s^2)$, and therefore this LO contribution can be included in $\sigma_{\text{NLO}}(pp \rightarrow ZG_{\text{KK}} + X)$ [110, 111].

The one-loop amplitudes for $gg \rightarrow H/ZG_{\text{KK}}$ are expected to be free of ultraviolet (UV) and infrared (IR) singularities for each quark flavour. The IR singularities (large logs in the mass regularization) are applicable to light quark cases only. We also expect gauge invariance with respect to the gluon and the KK-graviton currents. However, in the ZG_{KK} case, due to the presence of anomalies, the amplitude for an individual quark flavour may not be gauge invariant with respect to the axial-vector current in the $m_q \rightarrow 0$ limit. Since the model is free from anomalies, we expect gauge invariance after summing over all the six quark flavours. The confirmation of the cancellation of UV and IR singularities and gauge invariance with respect to the vector and axial-vector currents are powerful checks on our calculation. We make all these checks as described in the next section.

4.2 Details of Calculation and Checks

Our one-loop calculation is based on the traditional Feynman diagram method. The amplitude of each diagram is written using the SM and ADD model Feynman rules. The ADD model Feynman rules we require are also listed in the appendix D.1. However, we need not compute all the diagrams explicitly. We only need to compute the prototype diagrams. All other diagrams can be obtained by suitable permutations of the external momenta and polarizations. This works quite well in the HG_{KK} case. However, due to the presence of γ^5 in the ZG_{KK} amplitude, one needs to take extreme care in making these permutations in n dimensions. The permutation should not be across the γ^5 vertex. Such permuted diagrams need to be computed explicitly. Due to the presence of a quark loop, the amplitude of each diagram is proportional to the trace of a string of gamma matrices. We compute these traces using FORM [64]. This is the most important part of the calculation. The presence of 4-dimensional γ^5 in the trace, leads to spurious anomalies in the amplitude. We, therefore, need an appropriate n -dimensional treatment of γ^5 . We have used Larin's prescription for γ^5 to calculate the trace in n dimensions [113]. According to this prescription,

$$\gamma_\mu \gamma^5 = -\frac{i}{6} \epsilon_{\mu\nu\rho\sigma} \gamma^\nu \gamma^\rho \gamma^\sigma. \quad (4.6)$$

After calculating the trace, we express the amplitude in terms of appropriate tensor integrals. The box amplitude has rank-4 tensor integrals, while the triangle amplitude has rank-2 tensor integrals at the most. The tensor reduction into scalars is done in $n = (4-2\epsilon)$ dimensions using the methods of Odenborgh and Vermaseren [63], also described in the Sec. 2.1.3. All the required scalar integrals for the massless quark case are listed in the appendix B.2. We need only the UV and IR singular pieces of these scalars to verify the cancellation of UV and IR singularities. For both the cases of bottom and top quarks, we use FF library to calculate the required scalars [114]. Due to a very large and complicated expression of the amplitude, we compute the amplitude numerically before squaring it. This requires computation of the polarization vectors for the gauge bosons and for the KK-graviton. We have chosen the helicity basis for them. It also helps in making additional checks on our calculation by verifying relations among helicity amplitudes. The KK-graviton polarization tensor is constructed from the polarization vectors of two massive vector bosons as

suggested in [48]. To obtain hadronic cross sections, we perform integrations over two body phase space and the gluon PDFs, using a Monte Carlo integration subroutine based on the VEGAS algorithm. Since the KK-gravitons are produced directly, we also require an additional integration over the KK-graviton mass parameter M_{KK} , to obtain an inclusive cross section.

As discussed in the previous section, our one-loop processes are expected to be finite. We verify that both the massive and massless contributions are UV finite. We observe that each triangle diagram is UV finite by itself, while the box amplitude is UV finite only after adding all the box contributions. As we discussed in the Sec. 2.3.1, fermion loop diagrams are known to be IR finite, in both the massive and massless fermion cases, for any kind and any number of external particles attached to the loop. In the massless quark case, we check that each diagram is IR finite and therefore IR finiteness holds for the full amplitude. Finally, we check the gauge invariance of the amplitude with respect to the two gluons by replacing their polarizations with their respective momenta. In the HG_{KK} case, we observe that some of the triangle diagrams are separately gauge invariant with respect to both the gluons. To ensure the correctness of their contribution towards the full amplitude, we have also performed a gauge invariance check with respect to the KK-graviton current. In the ZG_{KK} case, we find that (only after using γ^5 prescription in the trace) both the bottom and top quark contributions are separately gauge invariant with respect to the two gluons. In ZG_{KK} -triangle class of diagrams, involving graviton-gauge boson coupling, we have chosen the gauge-fixing parameter $\xi = 1$ (the Feynman gauge) for the gluon case and $\xi = \infty$ (the Unitary gauge) for the Z boson case. As expected, the calculation does not depend on any specific choice of the gauge-fixing parameter. We also check gauge invariance of the amplitude with respect to the Z boson. Because of the anomaly, the two contributions are not separately gauge invariant. However, the total amplitude is gauge invariant up to the top quark mass, as expected due to the explicit breaking of the chiral symmetry. All these checks on our amplitude have been made both numerically as well as analytically. The issue of anomaly in ZG_{KK} amplitude is discussed in the end.

We have also cross-checked our calculations by taking the $m_t \rightarrow \infty$ limit. In the

ZG_{KK} case, for a given phase space point, we vary the top quark mass and observe that the amplitude-squared (which includes both the bottom and top quark contributions) approaches a constant value (the bottom quark contribution) as $m_t \rightarrow \infty$. This implies the complete decoupling of the top quark, *i.e.*, the top quark contribution of the amplitude goes to zero in large m_t limit. It is expected from the decoupling theorem [70]. This feature has been plotted in Fig. 4.2. The change in slope around $m_t = \sqrt{s}/2$ corresponds to a physical threshold after which the top quark propagators cannot go on-shell and the amplitude is real. It is well known that the decoupling theorem does not hold for fermion loop amplitudes involving a Higgs boson. This is because, the Higgs boson coupling to fermions is proportional to the fermion masses. Like in the case of $gg \rightarrow H$ amplitude, we do observe non-decoupling of the heavy top quark in the $gg \rightarrow HG_{KK}$ amplitude. In Fig. 4.3, the rise in the curve, as m_t increases in the beginning, is due to the explicit top quark mass dependence in the numerator (m_t^2 in the amplitude). As we approach larger values of m_t , the effective suppression ($\sim 1/m_t^2$ in the amplitude) due to the propagators dominates and the amplitude becomes independent of m_t .

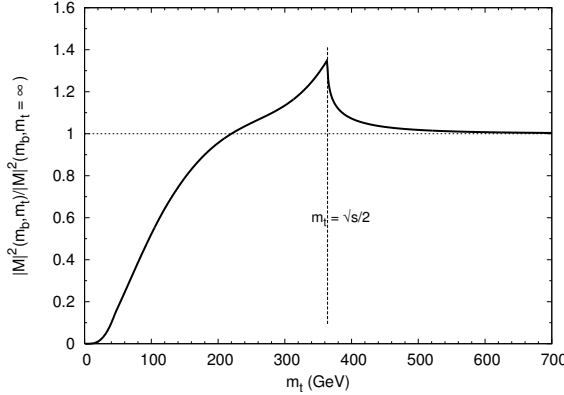


Figure 4.2: Decoupling of the top quark as $m_t \rightarrow \infty$, in $gg \rightarrow ZG_{KK}$.

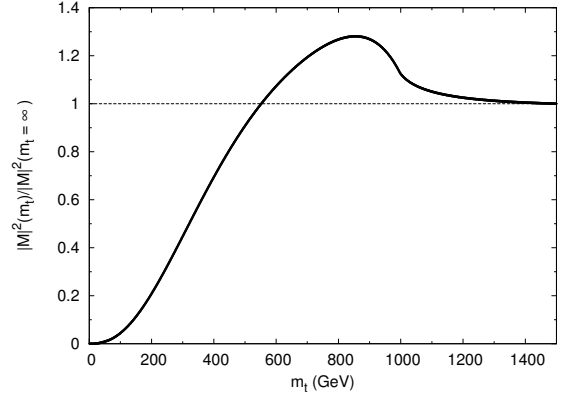


Figure 4.3: Non-decoupling of the top quark as $m_t \rightarrow \infty$, in $gg \rightarrow HG_{KK}$.

4.3 $gg \rightarrow HG_{KK}$ Calculation in the Effective theory of Gluon-Higgs coupling

In the heavy top quark limit ($m_t \gg M_H/2$), the interaction of gluons with the Higgs boson can be described by an effective Lagrangian [115],

$$\mathcal{L}_{eff} = -\frac{1}{4}g_{eff}G_{\mu\nu}^a G^{a,\mu\nu}H, \quad (4.7)$$

where the effective coupling is

$$g_{eff} = \frac{\alpha_s}{3\pi v} [1 + \mathcal{O}(M_H^2/4m_t^2)]. \quad (4.8)$$

It is known that the full calculation of the Higgs production via gluon fusion (including its radiative corrections), matches quite well with the calculation performed using this effective Lagrangian, even for physical top quark mass $m_t = 175$ GeV and $M_H = 120$ GeV [116–118]. We can also use this Lagrangian, in the ADD model to calculate $gg \rightarrow HG_{KK}$ process. Furthermore, we can compare this effective theory calculation with the full calculation. In the heavy top quark limit, both calculations should be in complete agreement. In this case, the diagrams contributing to the process are displayed in the Fig. 4.4. The Feynman rule for the last diagram is derived following

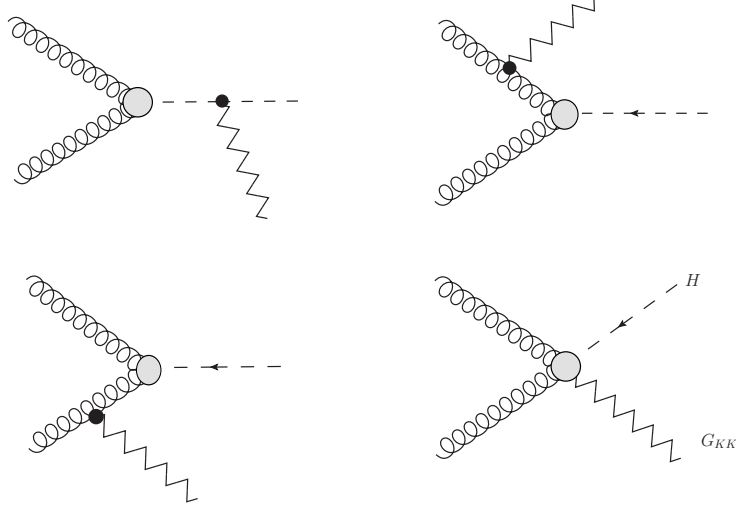


Figure 4.4: Feynman diagrams for $gg \rightarrow HG_{KK}$ in the heavy top quark limit.

Ref. [48] and it is added in the appendix D.1. In this effective theory, the amplitude-squared of $gg \rightarrow HG_{\text{KK}}$ process is

$$\begin{aligned} \sum_{pol.} |\mathcal{M}(gg \rightarrow HG_{\text{KK}})|^2 = & \frac{1}{6(M_H^2 - s)^2 t^2 u^2} \left[6M_H^{12}(t+u)^2 + 7s^2 t^2 u^2 (t+u)^2 - 12M_H^{10} \right. \\ & ((t+u)^3 + 2s(t^2 + tu + u^2)) + 6M_H^8((t+u)^2(t^2 + 4tu + u^2) + 2s^2(3t^2 + tu + 3u^2) + \\ & 2s(t+u)(3t^2 + 4tu + 3u^2)) - 4M_H^2 stu(3tu(t+u)^2 + 3s^2(t^2 + tu + u^2) + s(t+u) \\ & (3t^2 + 8tu + 3u^2)) - 12M_H^6(tu(t+u)^3 + 2s^3(t^2 + u^2) + 3s^2(t+u)(t^2 + tu + u^2) + \\ & s(t^4 + 7t^3u + 10t^2u^2 + 7tu^3 + u^4)) + 2M_H^4(3t^2u^2(t+u)^2 + 12stu(t+u)^3 + 3s^4 \\ & (t^2 + u^2) + 6s^3(t+u)(t^2 + tu + u^2) + s^2(3t^4 + 30t^3u + 44t^2u^2 + 30tu^3 + 3u^4)) \left. \right], \end{aligned} \quad (4.9)$$

where a summation over external polarizations is included. Here s, t and u are Mandelstam variables and they satisfy, $s + t + u = M_H^2 + M_{\text{KK}}^2$.

4.4 Numerical Results

In this section, we present results for $gg \rightarrow H/ZG_{\text{KK}}$ processes at the LHC. The results depend on the two parameters of the ADD model - (i) the number of extra-space dimensions δ and (ii) the fundamental scale of Gravity M_S . We will study this dependence and other features of our processes in the following. In Fig. 4.5, we have plotted the hadronic cross sections as a function of the collider centre-of-mass energy for both the processes. Due to a large gluon flux at higher energies, the cross sections also increase. Here we have chosen $\delta = 2$ and $M_S = 2$ TeV. This combination of the model parameters has already been ruled out. Nevertheless, for a study of the qualitative features of many of the results presented here, this combination is as good as any other combination. In addition, we have applied following kinematic cuts:

$$p_T^H > 20 \text{ GeV}, p_T^Z > 30 \text{ GeV}, |\eta^{H/Z}| < 2.5, \sqrt{s} < M_S. \quad (4.10)$$

The cut on the partonic centre-of-mass energy or equivalently on the $HG_{\text{KK}}/ZG_{\text{KK}}$ invariant mass is known as a *truncated scheme* in the literature. This cut is related to the fact that theoretical predictions within the ADD model, which is an effective field theory, can be valid only below the fundamental scale M_S . It will be interesting to

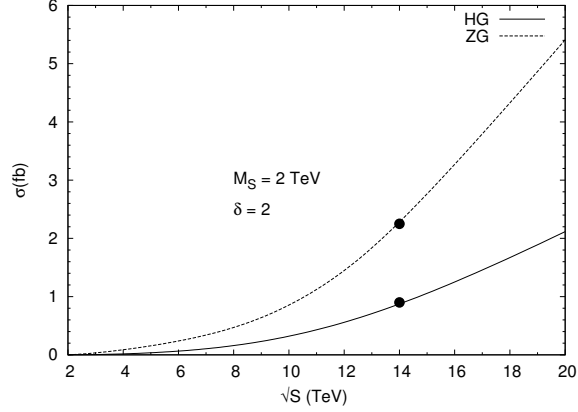


Figure 4.5: Collider energy dependence of the hadronic cross sections for $gg \rightarrow H/ZG_{\text{KK}}$ at the LHC.

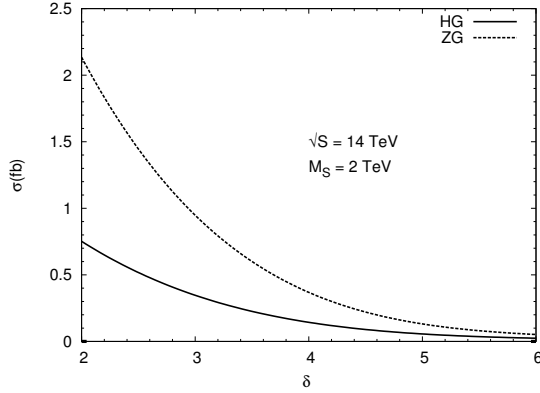


Figure 4.6: Dependence of the cross sections on the number of extra dimensions δ , for the scale $M_S = 2$ TeV.

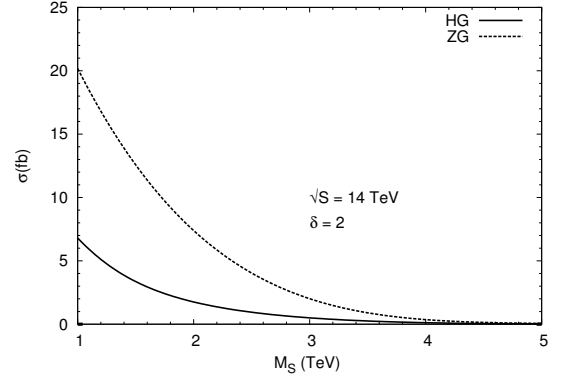


Figure 4.7: Dependence of the cross sections on the scale M_S , for the number of extra dimension $\delta = 2$

probe the sensitivity of our predictions on this kind of a constraint. We will further comment on the issue at the end of this section. Since our gluon fusion processes are finite, the partonic cross sections do not depend on the factorization scale μ_f . Also, their dependence on the renormalization scale μ_r is only through the strong coupling parameter α_s . We have chosen the transverse energy ($E_T = \sqrt{M^2 + (p_T)^2}$) of the weak bosons H/Z , as the common scale for the μ_f and μ_r . In principle, we can work with both the LO and NLO PDFs. We have used the LO CTEQ6L1 PDF, in the HG_{KK} case and the NLO CTEQ6M PDF, in ZG_{KK} case [88]. We note that at the

14 TeV LHC energy, the cross sections are 0.75 fb and 2.13 fb for the HG_{KK} and ZG_{KK} cases, respectively. The HG_{KK} cross section is much smaller than expected. The smallness of the cross section is due to two-orders of magnitude cancellation in the amplitude between the box and the triangle contributions. This destructive interference occurs due to the relative minus sign between the two contributions. However, the triangle and the box amplitudes are not separately gauge invariant. A similar cancellation is also seen in the ZG_{KK} amplitude. In the HG_{KK} case, we find that the bottom quark loop contribution to the cross section is less than a percent. In the ZG_{KK} case, we have also calculated the hadronic cross section for a $p_T^Z > 400$ GeV to avoid the SM background as suggested in [47]. We find that the cross section is about 0.2 fb and it is almost 10% of the NLO QCD correction calculated in [110, 111].

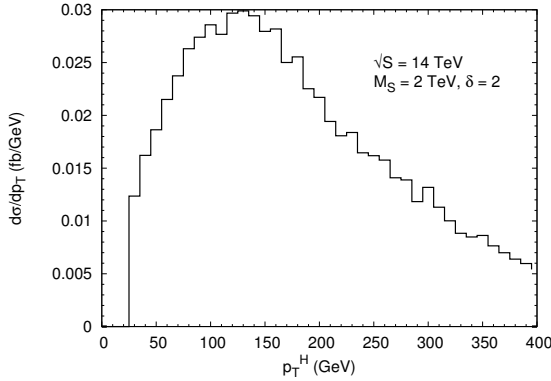


Figure 4.8: Transverse momentum distribution of the Higgs boson for $M_S = 2$ TeV and $\delta = 2$.

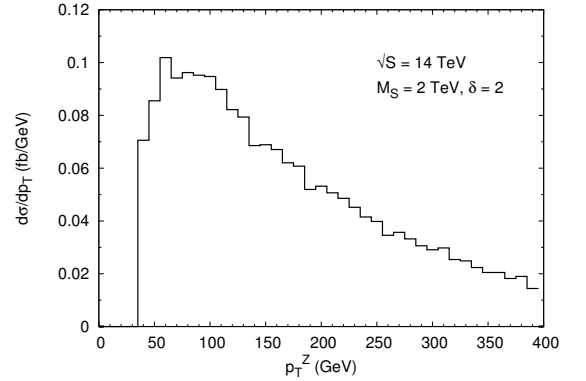


Figure 4.9: Transverse momentum distribution of the Z boson for $M_S = 2$ TeV and $\delta = 2$.

We now illustrate various kinematic aspects of these processes at the 14 TeV centre-of-mass energy. In Figs. 4.6 and 4.7, we show the dependence of inclusive cross sections of the two processes on the ADD model parameters δ and M_S . As δ or M_S is increased, the density of states for KK-graviton modes falls (see Eq.1.33), and therefore the cross sections also go down. The transverse momentum distributions of the Higgs and the Z boson are plotted in Figs. 4.8 and 4.9, respectively. The p_T distributions are peaked about the masses of the weak bosons as one would expect. In the direct production processes of KK-graviton, all the kinematically allowed modes

are produced. Figs. 4.10 and 4.11 show the KK-graviton mass distributions. Since the density of KK-graviton modes increases with the KK-graviton mass M_{KK} , the differential cross sections also increase before the phase space suppression takes over. As the Eq. 1.33 suggests, the peak in the distributions will depend on the ADD model parameters δ and M_S . Next, we study the scale dependence of the cross sections. We vary the common scale of the factorization and renormalization around its central value, $\mu_0 = E_T^{H/Z}$. The cross sections change by about 25 – 30% by changing μ in the range between $\mu_0/2$ and $2\mu_0$. We find that the uncertainty in our calculations, due to the choice of different PDF sets, is in the range of 5 – 20% for the two processes.

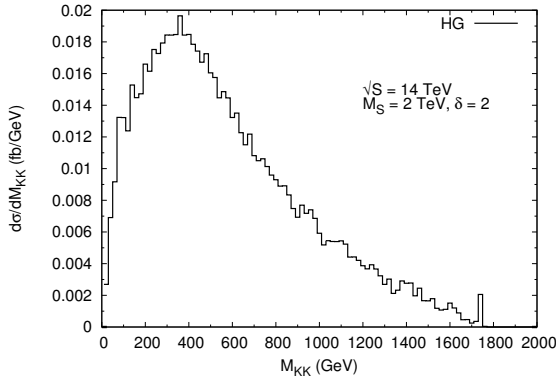


Figure 4.10: KK-graviton mass distribution in HG_{KK} case, for $M_S = 2$ TeV and $\delta = 2$.

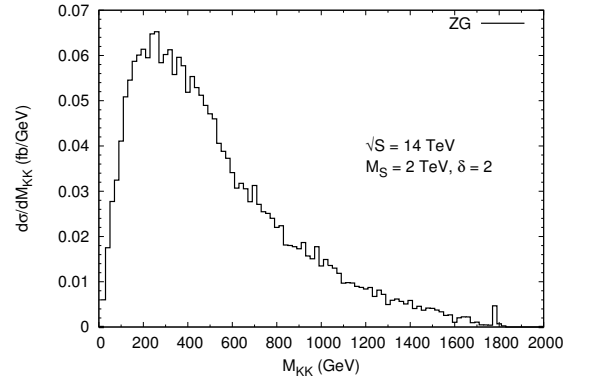


Figure 4.11: KK-graviton mass distribution in ZG_{KK} case, for $M_S = 2$ TeV and $\delta = 2$.

We discussed in the Sec. 4.3 that the process $gg \rightarrow HG_{\text{KK}}$ can also be calculated in an effective theory of ggH -coupling. The cross section calculations in the full theory and in the effective theory do not agree for $M_H = 120$ GeV and $m_t = 175$ GeV. However, the two calculations agree very well for a very large top quark mass value ($m_t \geq 1.2$ TeV) as required. This is shown in Fig. 4.12. Note that unlike the SM $gg \rightarrow H$ case, in our case, there is one extra scale present – namely, the mass of the KK-graviton M_{KK} . We have seen that the M_{KK} value is significantly larger than the mass of the top quark most of the time, see Fig. 4.10. Because of this, \sqrt{s} , which is larger than $M_H + M_{\text{KK}}$, can go much beyond $2m_t$. Therefore, one cannot expect the effective theory calculation to agree with the full calculation for $M_H = 120$ GeV and the physical top quark mass $m_t = 175$ GeV. Finally, we comment on the UV

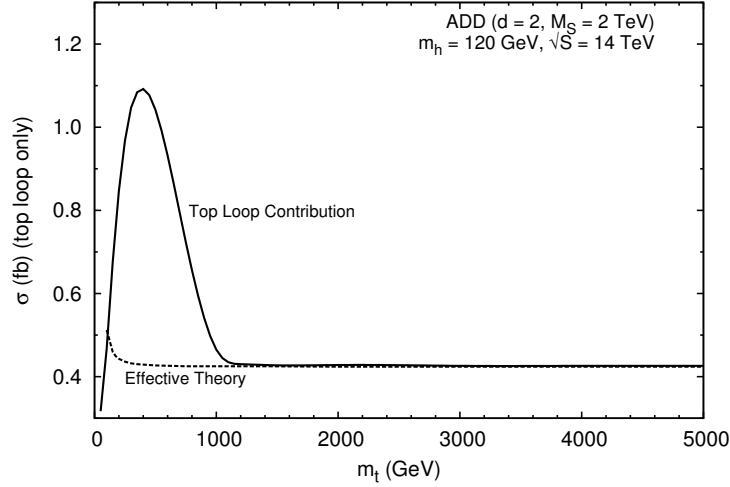


Figure 4.12: A comparison of $gg \rightarrow HG_{KK}$ cross sections calculated in full theory and in the effective theory.

sensitivity of our theoretical results. As mentioned before, we have presented all the results for which the partonic energy \sqrt{s} is below the fundamental scale M_S , *i.e.*, the truncated scheme. It has been argued in Ref. [47] that, if relaxing this constraint does not change the results significantly, then results of the effective field theory can be trusted. We find that the cross sections in the truncated and untruncated schemes (that is, with and without cut on \sqrt{s}) differ by 20% for $\delta = 2$ and $M_S = 2$ TeV. This difference, as expected, increases for larger values of δ while it decreases with increasing M_S [93].

4.5 A Discussion on ZG_{KK} Calculation

The coupling of the KK-graviton with the quarks is such that the triangle and the box diagrams, in the ZG_{KK} case, are linearly divergent in loop momentum and they have VVA and $VVVA$ coupling structures respectively. The issue of chiral anomaly is well known in a linearly divergent fermion loop triangle diagram having VVA -structure. Because of the linear divergence, the $VVVA$ -box diagrams also give anomalous contributions to the amplitude. This can be confirmed by checking the relations among

charge-conjugated box diagrams, in the absence of a suitable n -dimensional γ^5 prescription. The presence of anomaly affects the gauge invariance of the amplitude and for reliable predictions, our amplitude should be gauge invariant with respect to all the currents. We have already mentioned that if we do not regulate anomaly by using a suitable prescription for γ^5 , the amplitude for the bottom/top quark in the loop, is not gauge invariant with respect to the gluons due to spurious anomalies. Even the relations among charge-conjugated diagrams and the Bose symmetry of the amplitude do not hold. It turns out that the n -dimensional γ^5 prescription, given in Eq. 4.6, respects various symmetries of diagrams and the amplitude. We have mentioned that, with this γ^5 prescription, both the bottom and top quark contributions are separately gauge invariant with respect to the gluons and only the axial-vector current, corresponding to the Z boson, is anomalous. The anomaly in axial-vector current, being independent of the quark mass, also goes away in the full amplitude. See Eq. 4.5. We have learned from our general discussion on the chiral anomaly that the anomalous contributions to the amplitude, including the spurious ones in 4 dimensions, affect only the fermion mass independent rational part \mathcal{R} , see Sec. 2.3.2. The quark mass independence of the rational part, for an individual quark, is checked explicitly. In the full amplitude, shown in Eq. 4.5, the rational terms will cancel between the bottom and the top quark contributions. Therefore, even if we work with 4-dimensional γ^5 , the full amplitude is going to be gauge invariant with respect to all the currents. Although, the amplitude for an individual quark flavor in the loop will not be gauge invariant anymore, their difference in Eq. 4.5 is always gauge invariant. We have verified this in a separate calculation. All the numerical results, presented above, agree with this way of doing calculation. It is definitely more economical because with 4-dimensional γ^5 we require only one prototype box amplitude and two prototype triangle amplitudes (one for each class) to generate the full amplitude. On the other hand, if we use γ^5 prescription given in Eq. 4.6, we need two prototype box amplitudes and four prototype triangle amplitudes (two for each case) to generate the full amplitude. Also, with this γ^5 prescription, the trace calculation gives rise to a bigger expression for the amplitude of each diagram.

Chapter 5

Summary

In this thesis, we have considered two classes of gluon fusion processes which may be important at a high energy hadron collider such as the LHC. We have reported on the production of a pair of electroweak vector bosons with a jet via gluon fusion within the Standard Model. We have taken a model of large extra dimensions, the ADD model, as an example of new physics and have also considered the associated production of an electroweak boson and KK-gravitons. These gluon fusion processes receive contributions from the quark loop diagrams at the leading order and they are finite. The amplitude calculation is based on the traditional Feynman diagram approach. We have developed general purpose codes to perform the reduction of one-loop tensor integrals. All the basic scalar integrals which may appear in a one-loop amplitude are derived analytically and have been implemented in a FORTRAN routine. A flexible Monte Carlo integration routine based on the VEGAS algorithm is used to obtain the total as well as differential cross sections in these processes. To reduce the run time in the calculations of the SM processes, we have run the code in a parallel environment using the AMCI package.

We have verified our one-loop calculations by performing numerous checks on the amplitudes. We have checked the ultraviolet and infrared finiteness of the amplitudes. We have checked the structure of amplitudes by making gauge invariance checks. We have also verified the expected behavior of these amplitudes in the heavy quark mass limit. The general result regarding the infrared finiteness of an individual fermion loop diagram is also confirmed in these processes. We have shown and verified that

in a fermion loop amplitude, plagued from chiral anomaly, the anomaly is related to the rational part of the amplitude. We have given a prescription for obtaining the correct rational part in a UV finite fermion loop amplitude utilizing the decoupling theorem.

In our study of the SM processes, we find that due to a large gluon flux available at the LHC, these processes are quite important. The typical hadronic cross section for the $gg \rightarrow \gamma\gamma g$ is about 1 pb and it is about 10 % of the corresponding tree-level contribution. Like the $gg \rightarrow \gamma\gamma$ process, it is also important in the searches of a light Higgs boson. We find that the top quark loop contribution to the $gg \rightarrow \gamma\gamma g, \gamma Z g$ cross sections is negligible. For the processes $gg \rightarrow ZZg$ and $gg \rightarrow W^+W^-g$, we have kept only $\gamma Z g$ -like contributions. Their cross sections are in the range of 4 – 15% of the corresponding tree-level cross sections. We have observed a qualitative similarity of these processes with the corresponding di-vector boson production cases. At the 14 TeV centre-of-mass energy, the cross sections of $gg \rightarrow VV'g$ processes are 20-30 % of those for the $gg \rightarrow VV'$ processes. In a detailed study of the $gg \rightarrow \gamma Z g$ process, we have compared this NNLO level contribution with the LO and the NLO predictions using the MCFM program. We note that the percentage contribution ($\sigma^{\text{NNLO}}/\sigma^{\text{NLO}}$) is about 2-3% which can be enhanced by choosing an appropriate set of kinematic cuts. The cross section of this process is dominated by the box contributions and therefore by the vector part of the amplitude. The axial-vector part of the amplitude contributes only about 10 % towards the cross section. Being leading order process, the scale uncertainty in the cross section calculation is governed by the strong coupling parameter α_s and the parton distributions, and it is quite large ($\sim 25\text{-}40\%$). The observability of this process at the LHC is discussed considering the decay of the Z boson into the charged leptons. We find that at 14 TeV and with 100 fb^{-1} integrated luminosity, one can expect more than thousand events for $gg \rightarrow \gamma Z (\rightarrow l^+l^-)g$ process at the LHC. The issue of numerical instability in our calculations is dealt by systematically ignoring the contributions from the exceptional phase space points. We have adopted three different strategies to ignore their contributions, all in agreement within the allowed range of uncertainty. We have seen that such phase space points are very few and the contributions from such phase space points do not dominate the cross section.

In the ADD model processes, we have argued that the $gg \rightarrow \gamma G_{\text{KK}}$ amplitude vanishes at the leading order due to an extension of Furry's theorem which includes the graviton. We find that, as expected, the gluon-gluon contribution to $pp \rightarrow HG_{\text{KK}} + X$ dominates its cross section. For the model parameter values, $\delta = 2$ and $M_S = 2$ TeV, the hadronic cross section is only about 0.6 fb at 14 TeV LHC. We have cross-checked our full one-loop calculation by working in an effective theory of gluon-Higgs coupling. In the effective theory, the process becomes a tree-level process. We find that for the physical top quark mass there is no agreement between the two calculations. This difference can be attributed to the fact that we have a large scale, the mass of the KK-gravitons, present in the theory. However, in the limit of a very heavy top quark the two results are in complete agreement as desired. In the case of $gg \rightarrow ZG_{\text{KK}}$ process, we find that the amplitude gets contribution solely from the axial-vector part of the Z boson coupling to a quark and the quarks of a massless/mass-degenerate generation do not contribute. Due to the nature of graviton-quark coupling, the box diagrams are also anomalous along with the triangle diagrams. We also learned that the anomaly should be regulated using a suitable γ^5 prescription in n dimensions to ensure various symmetries of the diagrams and the amplitude. As expected, we find that the axial-vector current conservation in the amplitude holds only after including both the bottom and top quark contributions. The typical cross section at 14 TeV is about 2 fb and it is about 10 % of the NLO cross section for $\delta = 2$ and $M_S = 2$ TeV. In both the HG_{KK} and ZG_{KK} cases, we find that there is a significant cancellation at the amplitude level between the triangle and the box contributions. The smallness of the cross sections for these processes, particularly in the HG_{KK} case, may be due to this cancellation. The cross sections of these processes go down with increasing δ and/or M_S . We see that the massive KK-graviton modes contribute significantly towards the inclusive cross section. Like in the case of the SM processes, we do observe a large uncertainty ($\sim 5\text{-}20\%$) due to the scale variation. To check the sensitivity of our results on the scale of Gravity M_S , we have calculated the cross section in both the truncated and untruncated schemes and the results differ by about 20%.

We have seen that at higher energies, the contributions of all these gluon fusion processes increase. However, their cross sections suffer from large scale uncertainties

as mentioned above. The scale uncertainties can be reduced by calculating radiative corrections to these processes. The radiative corrections, which will also involve calculation of two-loop diagrams, are particularly important to our gluon fusion SM processes. Unlike the one-loop calculation, the calculation of two-loop amplitudes is not very common and its techniques are not yet standardized [119–122]. Very few two-loop calculations of phenomenological importance, are available even for three and four-point functions. We have mentioned that beyond four-point function, the one-loop calculations are subject to numerical instabilities near exceptional phase space points. In the traditional approach of tensor reduction, this issue can be resolved to a certain degree by employing special expressions for the reduction of higher point tensor integrals near such points [91]. One may also use modern techniques (on-shell methods), based on the generalized unitarity cut, of calculating one-loop amplitudes [66, 123–125]. These techniques are results of many important ideas which have been developed over the years and due to them the automation of one-loop calculations, like that of tree-level calculations, seems feasible [126–130]. Like the case of $gg \rightarrow VV'$, the compact analytic expressions for $gg \rightarrow VV'g$ amplitudes can be calculated using these techniques [79, 131, 132]. These analytic expressions will certainly reduce the computation time and can also be used for precision calculation at the LHC. The SM gluon fusion processes $gg \rightarrow VV'g$ with soft jet form the real radiation part of the radiative correction to $gg \rightarrow VV'$ processes. Therefore, a full radiative correction of the LO $gg \rightarrow VV'$ processes can be a fruitful exercise [133]. I would like to conclude by quoting *L. D. Landau*,

**“A method is more important than a discovery,
since the right method will lead to new
and even more important discoveries.”**

Appendix A

A.1 Units, Conventions, Notations & Definitions

Natural units and Conversion factors

$$\begin{aligned}\hbar &= c = 1 \\ 1 \text{ GeV} &= 1.783 \times 10^{-24} \text{ g} \\ (1 \text{ GeV})^{-1} &= 0.1973 \times 10^{-13} \text{ cm} \\ (1 \text{ GeV})^{-1} &= 0.658 \times 10^{-24} \text{ sec} \\ 1 \text{ barn} &= 10^{-24} \text{ cm}^2\end{aligned}\tag{A.1}$$

Metric

$$\begin{aligned}g^{\mu\nu} &= g_{\mu\nu} = \text{diag}(+1, -1, -1, -1) \\ p^\mu &= (p^0, \vec{p}), \quad p_\mu = g_{\mu\nu} p^\nu = (p^0, -\vec{p}) \\ p.k &= p^\mu k_\mu = p^0 k^0 - \vec{p}.\vec{k} \\ \partial^\mu &\equiv \frac{\partial}{\partial x_\mu} = \left(\frac{\partial}{\partial t}, -\vec{\nabla} \right),\end{aligned}\tag{A.2}$$

where $\vec{\nabla}$ is the gradient operator in three-dimensional space.

Pauli matrices

$$\sigma^1 = \begin{pmatrix} 0 & 1 \\ 1 & 0 \end{pmatrix}, \quad \sigma^2 = \begin{pmatrix} 0 & -i \\ i & 0 \end{pmatrix}, \quad \sigma^3 = \begin{pmatrix} 1 & 0 \\ 0 & -1 \end{pmatrix}.\tag{A.3}$$

Dirac matrices

$$\begin{aligned}
\{\gamma^\mu, \gamma^\nu\} &= 2g^{\mu\nu}; \quad \gamma^\mu = (\gamma^0, \gamma^i) \\
\{\gamma^\mu, \gamma^5\} &= 0; \quad \gamma^5 = i\gamma^0\gamma^1\gamma^2\gamma^3 \\
(\gamma^\mu)^\dagger &= \gamma^0\gamma^\mu\gamma^0, \quad (\gamma^5)^\dagger = \gamma^5 \\
(\gamma^0)^2 &= 1, \quad (\gamma^i)^2 = -1, \quad (\gamma^5)^2 = 1 \\
\text{tr}(\gamma^\mu\gamma^\nu\gamma^\rho\gamma^\sigma) &= 4(g^{\mu\nu}g^{\rho\sigma} - g^{\mu\rho}g^{\nu\sigma} + g^{\mu\sigma}g^{\nu\rho}) \\
\text{tr}(\gamma^\mu\gamma^\nu\gamma^\rho\gamma^\sigma\gamma^5) &= -4i \varepsilon^{\mu\nu\rho\sigma} \\
\text{tr}(\gamma^\mu\gamma^\nu\gamma^\rho\gamma^\sigma \dots) &= \text{tr}(\dots\gamma^\sigma\gamma^\rho\gamma^\nu\gamma^\mu) \\
\gamma^\mu\gamma_\mu &= n, \quad \gamma^\mu\gamma^\nu\gamma_\mu = -(n-2)\gamma^\nu
\end{aligned} \tag{A.4}$$

where $\varepsilon^{\mu\nu\rho\sigma}$ is completely antisymmetric tensor in 4 dimensions with following properties

$$\begin{aligned}
\varepsilon^{0123} &= -\varepsilon_{0123} = +1, \\
\varepsilon^{\alpha\beta\mu\nu}\varepsilon_{\alpha\beta\rho\sigma} &= -2(\delta_\rho^\mu\delta_\sigma^\nu - \delta_\sigma^\mu\delta_\rho^\nu).
\end{aligned} \tag{A.5}$$

Polarization sums

$$\begin{aligned}
\text{spin } \frac{1}{2}: \quad \sum_\lambda u^\lambda(p) \bar{u}^\lambda(p) &= (\not{p} - m); \quad \bar{u}^\lambda(p) = u^\lambda(p)^\dagger \gamma^0, \\
\sum_\lambda v^\lambda(p) \bar{v}^\lambda(p) &= (\not{p} + m); \quad \not{p} = \gamma^\mu p_\mu.
\end{aligned} \tag{A.6}$$

$$\begin{aligned}
\text{massless spin } 1: \quad \sum_\lambda \varepsilon_\mu^{(\lambda)}(p) \varepsilon_\nu^{*(\lambda)}(p) &\rightarrow -g_{\mu\nu}, \\
\text{massive spin } 1: \quad \sum_\lambda \varepsilon_\mu^{(\lambda)}(p) \varepsilon_\nu^{*(\lambda)}(p) &= -g_{\mu\nu} + \frac{p_\mu p_\nu}{M^2}.
\end{aligned} \tag{A.7}$$

$$\begin{aligned}
\text{massive spin } 2: \quad \sum_\lambda \varepsilon_{\mu\nu}^{(\lambda)}(p) \varepsilon_{\rho\sigma}^{*(\lambda)}(p) &= \left(-g_{\mu\rho} + \frac{p_\mu p_\rho}{M^2}\right) \left(-g_{\nu\sigma} + \frac{p_\nu p_\sigma}{M^2}\right) \\
&\quad + \left(-g_{\mu\sigma} + \frac{p_\mu p_\sigma}{M^2}\right) \left(-g_{\nu\rho} + \frac{p_\nu p_\rho}{M^2}\right) \\
&\quad - \frac{2}{n-1} \left(-g_{\mu\nu} + \frac{p_\mu p_\nu}{M^2}\right) \left(-g_{\rho\sigma} + \frac{p_\rho p_\sigma}{M^2}\right).
\end{aligned} \tag{A.8}$$

Spin-1 propagator in R_ξ -gauge

$$iD_{\mu\nu}(q^2, \xi) = \frac{i}{q^2 - M^2} \left[-g_{\mu\nu} + \frac{q_\mu q_\nu}{q^2 - \xi M^2} (1 - \xi) \right]. \quad (\text{A.9})$$

Some of the very popular choices of the gauge-fixing parameter are Landau gauge ($\xi = 0$), Feynman gauge ($\xi = 1$) and Unitary/Physical gauge ($\xi = \infty$).

In the context of tensor reduction

$$\begin{aligned} \{v_i\} &\rightarrow \text{dual vectors to } \{p_i\}, \\ \{u_i\} &\rightarrow \text{dual vectors to } \{q_i\}, \\ \text{such that } v_i \cdot p_j &= u_i \cdot q_j = \delta_{ij}, \text{ where } q_i = \sum_{j=1}^i p_j, \quad q_0 = 0. \end{aligned} \quad (\text{A.10})$$

Gamma function

$$\Gamma(z) = \int_0^\infty dt \, e^{-t} t^{z-1} \quad (\text{A.11})$$

$$\Gamma(1+z) = z\Gamma(z) \quad (\text{A.12})$$

$$\Gamma(\epsilon) = \frac{1}{\epsilon} - \gamma_E + \mathcal{O}(\epsilon) \quad (\text{A.13})$$

where $\epsilon \rightarrow 0$ and $\gamma_E \simeq 0.5772157$, is the Euler-Mascheroni constant.

Integral parameterizations

$$\frac{1}{a^N} = \frac{1}{\Gamma(N)} \int_0^\infty dt \, e^{-at} t^{N-1} \quad (\text{A.14})$$

This is known as Schwinger parameterization. We can use this to obtain the Feynman parameterization,

$$\frac{1}{\prod_{i=1}^N a_i} = \int_0^1 \prod_i dx_i \frac{(N-1)!}{(\sum_i a_i x_i)^N} \delta\left(\sum_i x_i - 1\right). \quad (\text{A.15})$$

n -dimensional integration

$$\int \frac{d^n l}{(2\pi)^n} \frac{1}{(l^2 - M^2)^N} = i \frac{(-1)^N}{(4\pi)^{n/2}} \frac{\Gamma(N - n/2)}{\Gamma(N)} \left(\frac{1}{M^2}\right)^{N-n/2} \quad (\text{A.16})$$

$SU(N)$ algebra

The generators T^a ($a = 1, 2, \dots, N^2 - 1$) of $SU(N)$ are hermitian, traceless matrices such that

$$[T^a, T^b] = i f^{abc} T^c. \quad (\text{A.17})$$

The numbers f^{abc} are called the structure constants. In the fundamental representation T^a are N -dimensional matrices and they satisfy,

$$\{T^a, T^b\} = \frac{1}{N}\delta^{ab} + d^{abc} T^c, \quad (\text{A.18})$$

$$\text{with, } \text{tr}(T^a T^b) = \frac{1}{2}\delta^{ab}. \quad (\text{A.19})$$

Here d^{abc} is totally symmetric in a, b and c . Since $\text{tr}(T^a T^b) \propto \delta^{ab}$, it can be seen that f^{abc} are totally antisymmetric in a, b and c . Some useful identities are

$$T^a T^b = \frac{1}{2N}\delta^{ab} + \frac{1}{2}d^{abc}T^c + \frac{1}{2}if^{abc}T^c, \quad (\text{A.20})$$

$$\text{tr}(T^a T^b T^c) = \frac{1}{4}(d^{abc} + if^{abc}), \quad (\text{A.21})$$

$$f^{abc}f^{a'bc} = N\delta^{aa'}, \quad (\text{A.22})$$

$$d^{abc}d^{a'bc} = \frac{(N^2 - 4)}{N}\delta^{aa'}, \quad d^{aab} = 0. \quad (\text{A.23})$$

In the adjoint representation, the generators T^a are $(N^2 - 1)$ -dimensional matrices and

$$(T^a)_{bc} = -if^{abc}. \quad (\text{A.24})$$

Standard Model parameters

The Fermi constant, $G_F = 1.166 \times 10^{-5} \text{ GeV}^{-2}$

$$M_Z = 91.1876 \text{ GeV}, \quad M_W = 80.403 \text{ GeV}$$

$$M_H = 125 \text{ GeV}, \quad m_b = 4.65 \text{ GeV}$$

$$m_t = 173.5 \text{ GeV}, \quad \sin^2\theta_w = 0.23$$

$$\alpha_{em}^{-1}(M_Z^2) = 127.918, \quad \alpha_s(M_Z^2) = 0.1176. \quad (\text{A.25})$$

A.2 Logs and Di-Logs

The natural logarithm of a complex number is a multivalued function having a branch cut along the negative real axis. For a complex number $z = re^{i\theta}$,

$$\begin{aligned} \ln(z) &= f_n(r, \theta) \\ &= \ln(r) + i(\theta + 2n\pi), \end{aligned} \quad (\text{A.26})$$

with $r > 0$ and $-\pi < \theta \leq \pi$. The $n = 0$ corresponds to the principal branch. The discontinuity of this function across the negative real axis can be seen by noting that,

$$\lim_{\epsilon \rightarrow 0} [f_n(r, \pi - \epsilon) - f_n(r, -\pi + \epsilon)] = 2i\pi. \quad (\text{A.27})$$

Also, note that

$$\lim_{\epsilon \rightarrow 0} f_n(r, \pi - \epsilon) = \lim_{\epsilon \rightarrow 0} f_{n+1}(r, -\pi + \epsilon), \quad (\text{A.28})$$

i.e., the moment θ exceeds π it goes to the next branch. Remember that $f_n(r, \theta)$ is single valued on each branch with $-\pi < \theta \leq \pi$. The rule for the logarithm of a product of two complex numbers z_1 and z_2 is,

$$\ln(z_1 z_2) = \ln(z_1) + \ln(z_2) + 2i\pi \eta(z_1, z_2), \quad (\text{A.29})$$

where

$$\begin{aligned} \eta(z_1, z_2) = & \Theta(-\text{Im } z_1) \Theta(-\text{Im } z_2) \Theta(\text{Im } z_1 z_2) \\ & - \Theta(\text{Im } z_1) \Theta(\text{Im } z_2) \Theta(-\text{Im } z_1 z_2). \end{aligned} \quad (\text{A.30})$$

In the analytical evaluation of the one-loop scalar integrals, one often comes across the Spence function or the di-logarithm. It is defined by [134]

$$\text{Sp}(z) = - \int_0^1 dt \frac{\ln(1 - zt)}{t} = - \int_0^z dt \frac{\ln(1 - t)}{t} \quad (\text{A.31})$$

$$= z + \frac{z^2}{2^2} + \frac{z^3}{3^2} + \dots \text{ for } |z| \leq 1. \quad (\text{A.32})$$

Since the branch cut of the logarithm is along the negative real axis, the branch cut of the Spence function starts at $z = 1$ along the positive real axis. Some of the special values are

$$\begin{aligned} \text{Sp}(-1) &= -\frac{\pi^2}{12}, \text{Sp}(0) = 0, \\ \text{Sp}(1) &= \frac{\pi^2}{6}, \text{Sp}(2) = \frac{\pi^2}{4}. \end{aligned} \quad (\text{A.33})$$

We list few important identities related to Spence functions,

$$-\text{Sp}(1 - z) = \text{Sp}(z) + \ln(z)\ln(1 - z) - \frac{\pi^2}{6} \quad (\text{A.34})$$

$$-\text{Sp}\left(\frac{1}{z}\right) = \text{Sp}(z) + \frac{1}{2}\ln^2(-z) + \frac{\pi^2}{6} \quad (\text{A.35})$$

$$\text{Sp}(z) + \text{Sp}(-z) = \frac{1}{2} \text{Sp}(z^2). \quad (\text{A.36})$$

Some simple identities which could be useful in the evaluation of the one-loop scalar integrals are,

$$\ln(a \pm i\epsilon) = \ln|a| \pm i\pi \Theta(-a) \quad (\text{A.37})$$

$$\ln(a - i\epsilon a) = \ln(a + i\epsilon) \quad (\text{A.38})$$

$$\ln(-a - i\epsilon a) = \ln(-a - i\epsilon) \quad (\text{A.39})$$

$$\begin{aligned} \ln(a + i\epsilon) + \ln(b - i\epsilon) &= \ln[ab + i\epsilon \operatorname{sign}(b - a)] \\ &= \ln[ab + i\epsilon \operatorname{sign}(b)] \\ &= \ln[ab - i\epsilon \operatorname{sign}(a)] \end{aligned} \quad (\text{A.40})$$

$$\begin{aligned} \ln\left(\frac{a}{b - i\epsilon}\right) &= \ln\left(\frac{a}{b} + i\epsilon a\right) \\ &= \ln\left(\frac{a - i\epsilon}{b - i\epsilon}\right) \end{aligned} \quad (\text{A.41})$$

$$\operatorname{Sp}(a \pm i\epsilon a) = \operatorname{Sp}(a \pm i\epsilon) \quad (\text{A.42})$$

$$\operatorname{Sp}(-a \pm i\epsilon a) = \operatorname{Sp}(-a \mp i\epsilon). \quad (\text{A.43})$$

Here a and b are real numbers and ϵ is a vanishingly small positive number.

Appendix B

B.1 Simple analysis of infrared singularities at one-loop

Computation of virtual diagrams involve integration over undetermined loop momenta. These loop integrals may be ill-defined as they may diverge for certain limiting values of the momentum flowing in the loop. A well known case is that of the ultra-violet singularity which may arise as the loop momentum becomes very large. With massless particles present in the theory, these integrals may develop infrared (IR) or more appropriately mass singularities as well. Also, there are singularities which originate from specific phase space points such as physical and anomalous thresholds. A systematic study of the mass singularities and the threshold singularities can be done via Landau Equations [135–137]. Kinoshita describes the mass singularities of Feynman amplitudes as pathological solutions of Landau Equations [69].

Here we limit ourselves to the IR singularity of one-loop diagrams, away from any threshold. Also we do not consider any exceptional phase space point, corresponding to the vanishing of any partial sum of external momenta. According to Kinoshita, these are pure mass singularities, valid for all possible kinematic invariants made out of the external momenta. These mass singularities can be of soft or collinear type. Under certain circumstances, which we will discuss below, an overlapping of the soft and collinear singularities may also occur. In Ref. [69], this issue is discussed thoroughly, using a parametric form of the loop integrals. We will explore the structure of IR singularities of Feynman diagrams at the one-loop via naive power counting in the loop momentum.

The most general one-loop integral is of tensor type, in which the loop momentum appears in the numerator. One-loop diagrams with fermions in the loop are common examples of such integrals. Since any tensor integral at one-loop can be expressed in terms of scalar ones (*i.e.*, the one-loop integrals in ϕ^3 -theory), it is sufficient to apply our analysis to the scalar integrals only.

B.1.1 Soft singularity

These singularities appear as a result of any of the internal lines becoming soft, that is, its momentum vanishes. We consider the N -point scalar integral, Fig. B.1, in n dimensions, given by

$$I^N(p_i, m_i; i = 0 \rightarrow N - 1) = \int d^n l \frac{1}{d_0 d_1 \dots d_{N-1}}, \quad (\text{B.1})$$

with following notations for simplification,

$$\begin{aligned} d_i &= l_i^2 - m_i^2, \quad l_i = l + q_i \\ \text{and } q_i &= p_0 + p_1 + \dots + p_i. \end{aligned} \quad (\text{B.2})$$

In our notation, $p_0 = 0$, but to start with $m_0 \neq 0$. Now we wish to derive conditions

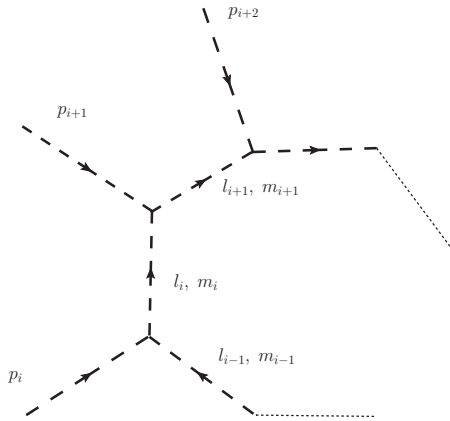


Figure B.1: General scalar one-loop diagram with momentum assignment

under which above integral may diverge as one of the internal momenta in the loop, say l_i , becomes soft. We will take $l_i = \epsilon$, with the understanding that soft limit for

l_i is reached as $\epsilon \rightarrow 0$. With $l_i = \epsilon$, in our notation, relevant denominators take the following form

$$\begin{aligned} d_{i-1} &= p_i^2 - 2\epsilon \cdot p_i - m_{i-1}^2, \\ d_i &= \epsilon^2 - m_i^2 \\ \text{and } d_{i+1} &= p_{i+1}^2 + 2\epsilon \cdot p_{i+1} - m_{i+1}^2. \end{aligned} \tag{B.3}$$

We have dropped ϵ^2 against $\epsilon \cdot p_i$ and $\epsilon \cdot p_{i+1}$, assuming ϵ is not orthogonal to p_i and p_{i+1} . The above denominators vanish under the soft limit, if

$$m_i = 0, \quad p_i^2 = m_{i-1}^2 \quad \text{and} \quad p_{i+1}^2 = m_{i+1}^2. \tag{B.4}$$

Thus in the soft limit, the scalar integral in Eq. B.1, behaves as

$$I^N \sim \int d^n \epsilon \frac{1}{\epsilon \cdot p_i \epsilon^2 \epsilon \cdot p_{i+1}} \sim \epsilon^{n-4}, \tag{B.5}$$

which diverges logarithmically in $n = 4$. In $m_i \rightarrow 0$ limit, the divergence appears as $\ln(m_i)$. Kinoshita called it λ -singularity. It is easy to check that no other denominator vanishes in the soft limit of l_i , in general. Thus, *the appearance of a soft singularity in one-loop diagrams is associated with the exchange of a massless particle between two on-shell particles*. The structure of the soft singularity in Eq. B.5 suggests that it can occur for $N \geq 3$ point functions only. A text book example of soft-singular integral is the one-loop vertex correction in QED with massive fermions, as shown in Fig. B.2.

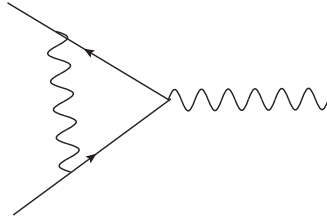


Figure B.2: One-loop correction to QED vertex

B.1.2 Collinear singularity

At one-loop, collinear singularity may appear when one of the internal momenta becomes collinear with a neighboring external leg. See Fig. B.1. We consider

$$l_i = xp_{i+1} + \epsilon_\perp, \quad (\text{B.6})$$

where $x \neq 0, -1$ (since they correspond to the softness of l_i and l_{i+1} , respectively) and $\epsilon_\perp \cdot p_{i+1} = 0$. The collinear limit is obtained as $\epsilon_\perp \rightarrow 0$. In this case relevant denominators are,

$$\begin{aligned} d_i &= x^2 p_{i+1}^2 + \epsilon_\perp^2 - m_i^2 \\ \text{and } d_{i+1} &= (x+1)^2 p_{i+1}^2 + \epsilon_\perp^2 - m_{i+1}^2. \end{aligned} \quad (\text{B.7})$$

The general conditions for these denominators to vanish are

$$p_{i+1}^2 = 0, \quad m_i = 0, \quad m_{i+1} = 0, \quad (\text{B.8})$$

that is, *one-loop diagrams in which a massless external leg meets two massless internal lines may develop a collinear divergence*. In fact, the first of the above three conditions is hidden in the assumption, $\epsilon_\perp \cdot p_{i+1} = 0$. In $\epsilon_\perp \rightarrow 0$ limit, this equality implies

$$\cos \theta \simeq \frac{p_{i+1}^0}{|\mathbf{p}_{i+1}|} > 1, \quad (\text{B.9})$$

for massive p_{i+1} . Thus for the collinear limit ($\theta \rightarrow 0$), p_{i+1} must be massless. No other denominator vanishes for non-exceptional phase space points. The N -point scalar integral in this limit goes as

$$I^N \sim \int d^m \epsilon_\perp \frac{1}{\epsilon_\perp^2 \epsilon_\perp^2} \sim \epsilon_\perp^{n-4}, \quad (\text{B.10})$$

which, like the soft singularity, is also logarithmically divergent. This singularity, sometimes referred as m -singularity, can be regularized by setting $m_{i+1} = m_i$ and taking $m_i \rightarrow 0$ limit. It appears as $\ln(m_i)$ term, as expected. Thus the one-loop QED vertex correction diagram, shown in Fig. B.2, will also have a collinear type singularity in the massless fermion limit.

B.1.3 Overlapping regions

Since we have studied the structure of the soft and the collinear singularities of a one-loop diagram, it is desirable to seek the possibility of their overlap. A soft piece with all lines massless, contains two collinear pieces. Let this soft piece be the part of a scalar N -point function in n dimensions. We set $l_i = \epsilon$, to write the N -point scalar integral for massless internal and external lines, keeping only (in general) potentially divergent denominators as $\epsilon \rightarrow 0$.

$$I^N \simeq \int d^n \epsilon \frac{1}{(\epsilon^2 - 2\epsilon \cdot p_i) \epsilon^2 (\epsilon^2 + 2\epsilon \cdot p_{i+1})}. \quad (\text{B.11})$$

Instead of taking $\epsilon \rightarrow 0$ limit right away, which clearly corresponds to the soft limit, we wish to break the above integral into soft and collinear regions. This job is easily done in the light-cone coordinates as suggested in Ref. [138]. In this coordinate, a 4-vector is written as $v \equiv (v^+, v^-, \mathbf{v}_\perp)$ where, $v^\pm = \frac{1}{\sqrt{2}}(v^0 \pm v^3)$ and $\mathbf{v}_\perp = (v^1, v^2)$ is a 2-dimensional Euclidean vector. The dot product of two 4-vectors then takes following form

$$u \cdot v = u^+ v^- + u^- v^+ - \mathbf{u}_\perp \cdot \mathbf{v}_\perp. \quad (\text{B.12})$$

This can easily be generalized to n dimensions. In the centre-of-mass frame of p_i and p_{i+1} , using the light-cone variables, we may write

$$p_i \equiv \sqrt{2} \omega (1, 0, \mathbf{0}_\perp), \quad p_{i+1} \equiv \sqrt{2} \omega (0, 1, \mathbf{0}_\perp). \quad (\text{B.13})$$

Here $\mathbf{0}_\perp$ is a $(n-2)$ -dimensional null vector in Euclidean space. Now the integral in Eq. B.11, reads

$$I^N \simeq \int \frac{d\epsilon^+ d\epsilon^- d^{n-2}\epsilon_\perp}{(\epsilon^2 - 2\sqrt{2}\omega\epsilon^-) \epsilon^2 (\epsilon^2 + 2\sqrt{2}\omega\epsilon^+)}, \quad (\text{B.14})$$

with $\epsilon^2 = 2\epsilon^+\epsilon^- - \epsilon_\perp^2$. Notice that we can make ϵ and therefore l_i , collinear to p_i by setting ϵ^- and ϵ_\perp equal to zero. To do it more systematically, we choose $\epsilon^- = \lambda \epsilon_\perp^2$ where $\lambda \neq 0$ and take $\epsilon_\perp \rightarrow 0$ limit in the above equation, so that the integral becomes

$$I^N \sim \int \frac{d\epsilon^+ d\lambda \epsilon_\perp^2 d^{n-2}\epsilon_\perp}{\epsilon_\perp^2 \epsilon_\perp^2 \epsilon^+} = \int d\lambda \frac{d\epsilon^+}{\epsilon^+} \frac{d^{n-2}\epsilon_\perp}{\epsilon_\perp^2}. \quad (\text{B.15})$$

Once again we obtain the log-type collinear singularity in $n = 4$ dimensions. Furthermore, if we take $\epsilon^+ \rightarrow 0$, we make l_i soft and we see the overlapping of the soft and

collinear singularities, which is also logarithmic in nature. Note that this singularity structure never gets worse for any other choice of ϵ^- made above. It should be obvious that for non-exceptional phase space points there is no overlapping of two soft regions or two distant collinear regions in a one-loop diagram. Thus a one-loop IR divergent integral is written as sum of terms, each containing two large-log factors at the most. In dimensional regularization ($n = 4 - 2\epsilon_{IR}$, $\epsilon_{IR} \rightarrow 0^-$), IR singular terms at one-loop appear as coefficients of $1/\epsilon_{IR}$ (soft and/or collinear case) and $1/\epsilon_{IR}^2$ (overlapping case) [61]. In Fig. B.2, if we allow fermion lines to be massless, the one-loop correction to QED vertex exhibits the full structure of IR divergences that can appear in a general one-loop amplitude.

We have seen that for a one-loop diagram to have the IR singularity, at least one internal line must be massless. Diagrams with all the external legs off-shell are IR finite, even if all the internal lines are massless. The tensor integrals at most retain the IR-singular structure of the scalar integrals. Since, at maximum, three denominators of a general N -point scalar integral vanish at a time in infrared regions, one should expect the possibility of expressing IR-singular terms of any one-loop diagram ($N > 3$), in terms of those of appropriate 3-point functions. In Ref. [139], this expectation is achieved for the most general one-loop integral. We have also argued this in Sec. 2.3.1. The above analysis also tells us that any one-loop diagram is IR finite in $n > 4$ dimensions.

B.2 One-loop scalar integrals

Evaluation of one-loop scalar integrals involves integration over undetermined loop momentum. We may encounter UV singularity in these integrals as loop momentum becomes very large. Naive power counting suggests that only tadpole and bubble integrals are UV divergent integrals. We use dimensional regularization ($n = 4 - 2\epsilon$) to regulate UV singularities [140]. Although the tadpole has quadratic divergence while the bubble is log-divergent, in dimensional regularization both type of UV singularities appear as $1/\epsilon$ pole. In this thesis, we are interested in fermion loop amplitudes. In many practical calculations, masses of fermions can be neglected.

Presence of massless particles leads to another kind of singularity in the one-loop scalar integrals, called the mass singularity. In 4 dimensions, these are of log-type as explained in the previous section. We have regularized these singularities by giving a small mass to the fermions. These scalar integrals are derived in the special case of $m_i^2 = m^2$, following 't Hooft and Veltman [57]. We maintain the full analytic continuation of these integrals. Depending upon external virtualities there are many cases in each class of scalar integrals.

1. One-point (Tadpole) Scalar Integral

$$\begin{aligned} A_0(m^2) &= \frac{i}{16\pi^2} m^2 [1 + \Delta_m], \\ \Delta_m &= \frac{1}{\epsilon} - \gamma_E + \ln\left(\frac{4\pi\mu^2}{m^2}\right) + \mathcal{O}(\epsilon). \end{aligned} \quad (\text{B.16})$$

Clearly for massless internal line, the tadpole scalar integral vanishes.

2. Two-point (Bubble) Scalar Integral

$$B_0(p^2; m^2) = \frac{i}{16\pi^2} \left[\Delta_m + 2 - z \ln\left(\frac{z+1}{z-1}\right) \right] \quad (\text{B.17})$$

where $z = \sqrt{1 - 4(m^2 - i\epsilon)/p^2}$. In the massless limit, this integral becomes

$$B_0(p^2; m^2 \rightarrow 0) = \frac{i}{16\pi^2} \left[\Delta_m + 2 - \ln\left(\frac{-p^2 - i\epsilon}{m^2}\right) \right], \quad (\text{B.18})$$

but there is no mass singularity. These expressions cannot be used in the case $p^2 = 0$, and therefore the integral should be separately evaluated for this particular case. The result is,

$$B_0(p^2 = 0; m^2) = \frac{i}{16\pi^2} \Delta_m. \quad (\text{B.19})$$

For the case of $p^2 = 0$, the integral develops a collinear singularity in $m^2 \rightarrow 0$ limit. However, the same integral can be shown to vanish in dimensional regularization, when $p^2 = 0, m^2 = 0$. In the special case of massless fermion loop amplitudes, one can see a correspondence between the mass regularization and the dimensional regularization of infrared singularities. Thus for our purposes, A_0 and B_0 integrals are never mass singular.

Since the triangle and box scalar integrals are UV finite, we can evaluate them in 4 dimensions. In $m^2 \rightarrow 0$ limit, these and higher point scalar integrals have the following general structure,

$$I_0^{1-loop} = \frac{i}{16\pi^2} \frac{1}{K} [f_2 \ln^2(m^2) + f_1 \ln(m^2) + f_0]. \quad (\text{B.20})$$

In 4 dimensions, the knowledge of A_0, B_0, C_0 and D_0 integrals is sufficient. The coefficients f_i , in various IR divergent scalar integrals are as follows:

3. Three-point (Triangle) Scalar Integrals

Case I: $p_1^2 = 0; p_2^2 = 0; p_3^2 \neq 0$

$$\begin{aligned} K &= 2p_3^2, \\ f_2 &= 1, \\ f_1 &= -2 \ln(-p_3^2 - i\epsilon), \\ f_0 &= \ln^2(-p_3^2 - i\epsilon). \end{aligned} \quad (\text{B.21})$$

For finite m^2 , $f_1 = f_2 = 0$ and $f_0 = \ln^2[(z+1)/(z-1)]$. Here $z = \sqrt{1 - 4(m^2 - i\epsilon)/p_3^2}$.

Case II: $p_1^2 = 0; p_2^2 \neq 0; p_3^2 \neq 0$

$$\begin{aligned} K &= 2(p_3^2 - p_2^2), \\ f_2 &= 0, \\ f_1 &= -2 \ln(-p_3^2 - i\epsilon) + 2 \ln(-p_2^2 - i\epsilon), \\ f_0 &= \ln^2(-p_3^2 - i\epsilon) - \ln^2(-p_2^2 - i\epsilon). \end{aligned} \quad (\text{B.22})$$

Case III: $p_1^2 \neq 0; p_2^2 \neq 0; p_3^2 \neq 0$

$$\begin{aligned} K &= p_1^2 + p_2^2(1 - 2\alpha) - p_3^2, \\ f_2 &= 0, \\ f_1 &= 0, \\ f_0 &= \sum_{i=1,2,3} (-1)^i \left[\text{Sp} \left(\frac{y_i - 1}{y_i + i\epsilon_i} \right) - \text{Sp} \left(\frac{y_i}{y_i - 1 - i\epsilon_i} \right) \right], \end{aligned} \quad (\text{B.23})$$

where

$$\begin{aligned} y_1 &= \frac{p_1^2(1 - \alpha) + \alpha p_3^2}{\alpha K}, \quad y_2 = \frac{\alpha}{\alpha - 1} y_1, \\ y_3 &= \frac{p_1^2 - \alpha p_2^2}{K} \quad \text{and} \quad \epsilon_i = \epsilon \text{ sign}(p_i^2). \end{aligned} \quad (\text{B.24})$$

Also, α satisfies

$$p_2^2 \alpha^2 - (p_1^2 + p_2^2 - p_3^2) \alpha + p_1^2 = 0. \quad (\text{B.25})$$

4. Four-point (Box) Scalar Integrals

Case I: $p_i^2 = 0, \forall i = 1, 2, 3, 4$

$$\begin{aligned} K &= s_{12} s_{23}, \\ f_2 &= 2, \\ f_1 &= -2 \ln(-s_{12} - i\epsilon) - 2 \ln(-s_{23} - i\epsilon), \\ f_0 &= 2 \ln(-s_{12} - i\epsilon) \ln(-s_{23} - i\epsilon) - \pi^2. \end{aligned} \quad (\text{B.26})$$

Case II: $p_1^2 = 0; p_2^2 = 0; p_3^2 = 0; p_4^2 \neq 0$

$$\begin{aligned} K &= s_{12} s_{23}, \\ f_2 &= 1, \\ f_1 &= -2 \ln(-s_{12} - i\epsilon) - 2 \ln(-s_{23} - i\epsilon) + 2 \ln(-p_4^2 - i\epsilon), \\ f_0 &= 2 \text{Sp}(1 + \alpha s_{12} + i\epsilon) + 2 \text{Sp}(1 + \alpha s_{23} + i\epsilon) - 2 \text{Sp}(1 + \alpha p_4^2 + i\epsilon) + \\ &\quad \ln^2(-s_{12} - i\epsilon) + \ln^2(-s_{23} - i\epsilon) - \ln^2(-p_4^2 - i\epsilon) - \frac{\pi^2}{3}, \end{aligned} \quad (\text{B.27})$$

where $\alpha = (p_4^2 - s_{12} - s_{23})/K$ and $s_{ij} = (p_i + p_j)^2$.

Case III: $p_1^2 = 0; p_2^2 \neq 0; p_3^2 = 0; p_4^2 \neq 0$

$$\begin{aligned} K &= s_{12} s_{23} - p_2^2 p_4^2, \\ f_2 &= 0, \\ f_1 &= -2 \ln(-s_{12} - i\epsilon) - 2 \ln(-s_{23} - i\epsilon) + 2 \ln(-p_2^2 - i\epsilon) + 2 \ln(-p_4^2 - i\epsilon), \\ f_0 &= 2 \text{Sp}(1 + \alpha s_{12} + i\epsilon) + 2 \text{Sp}(1 + \alpha s_{23} + i\epsilon) - \\ &\quad 2 \text{Sp}(1 + \alpha p_2^2 + i\epsilon) - 2 \text{Sp}(1 + \alpha p_4^2 + i\epsilon) + \\ &\quad \ln^2(-s_{12} - i\epsilon) + \ln^2(-s_{23} - i\epsilon) - \ln^2(-p_2^2 - i\epsilon) - \ln^2(-p_4^2 - i\epsilon), \end{aligned} \quad (\text{B.28})$$

where, $\alpha = (p_2^2 + p_4^2 - s_{12} - s_{23})/K$. The above expressions of the box scalar integrals, can be compared with those derived in Ref. [141]¹. For the next

¹ In Ref. [141], the IR divergent box integrals are derived in the dimensional regularization and their expressions contain terms which are artifacts of the dimensional regularization. In an IR finite amplitude such terms do not contribute.

two cases, the box scalar integrals that we have derived following 't Hooft and Veltman, have very complicated structure and we do not give those expressions here. The divergent coefficients f_1 and f_2 are derived using the identity given in Eq. 2.105, while the expressions for f_0 's are taken from Ref. [141].

Case IV: $p_1^2 = 0; p_2^2 = 0; p_3^2 \neq 0; p_4^2 \neq 0$

$$\begin{aligned}
K &= s_{12}s_{23}, \\
f_2 &= \frac{1}{2}, \\
f_1 &= -\ln(-s_{12} - i\epsilon) - 2\ln(-s_{23} - i\epsilon) + \ln(-p_3^2 - i\epsilon) + \ln(-p_4^2 - i\epsilon), \\
f_0 &= 2\operatorname{Sp}(1 + \alpha s_{12} + i\epsilon) + 2\operatorname{Sp}(1 + \alpha s_{23} + i\epsilon) - 2\operatorname{Sp}(1 + \alpha p_4^2 + i\epsilon) + \\
&\quad 2\operatorname{Sp}\left(1 - \frac{p_3^2 + i\epsilon}{s_{23} + i\epsilon}\right) - 2\operatorname{Sp}\left(1 - \frac{p_4^2 + i\epsilon}{s_{12} + i\epsilon}\right) + \\
&\quad \ln^2(-s_{12} - i\epsilon) + \ln^2(-s_{23} - i\epsilon) - \ln^2(-p_3^2 - i\epsilon) - \ln^2(-p_4^2 - i\epsilon) + \\
&\quad \frac{1}{2} [\ln(-p_3^2 - i\epsilon) + \ln^2(-p_4^2 - i\epsilon) - \ln(-s_{12} - i\epsilon)]^2, \tag{B.29}
\end{aligned}$$

where, $\alpha = (p_4^2 - s_{12} - s_{23})/K$.

Case V: $p_1^2 = 0; p_2^2 \neq 0; p_3^2 \neq 0; p_4^2 \neq 0$

$$\begin{aligned}
K &= s_{12}s_{23} - p_2^2 p_4^2, \\
f_2 &= 0, \\
f_1 &= -\ln(-s_{12} - i\epsilon) - \ln(-s_{23} - i\epsilon) + \ln(-p_2^2 - i\epsilon) + \ln(-p_4^2 - i\epsilon), \\
f_0 &= 2\operatorname{Sp}(1 + \alpha s_{12} + i\epsilon) + 2\operatorname{Sp}(1 + \alpha s_{23} + i\epsilon) - 2\operatorname{Sp}(1 + \alpha p_2^2 + i\epsilon) - \\
&\quad 2\operatorname{Sp}(1 + \alpha p_4^2 + i\epsilon) + 2\operatorname{Sp}\left(1 - \frac{p_3^2 + i\epsilon}{s_{23} + i\epsilon}\right) - 2\operatorname{Sp}\left(1 - \frac{p_4^2 + i\epsilon}{s_{12} + i\epsilon}\right) + \\
&\quad \ln^2(-s_{12} - i\epsilon) + \ln^2(-s_{23} - i\epsilon) - \ln^2(-p_2^2 - i\epsilon) - \ln^2(-p_3^2 - i\epsilon) - \\
&\quad \ln^2(-p_4^2 - i\epsilon) + \frac{1}{2} [\ln(-p_2^2 - i\epsilon) + \ln^2(-p_3^2 - i\epsilon) - \ln(-s_{23} - i\epsilon)]^2 + \\
&\quad \frac{1}{2} [\ln(-p_3^2 - i\epsilon) + \ln^2(-p_4^2 - i\epsilon) - \ln(-s_{12} - i\epsilon)]^2, \tag{B.30}
\end{aligned}$$

where, $\alpha = (p_2^2 + p_4^2 - s_{12} - s_{23})/K$.

The expressions of all the IR divergent scalar integrals, that we have derived in the mass regularization, can be compared with the complete list of divergent scalar integrals given in Ref. [61]. In this reference, the IR divergence of the scalar integrals is treated in the dimensional regularization ($n = 4 - 2\epsilon$). We can see that there is

a one-to-one correspondence (apart from terms that are artifacts of the dimensional regularization) between the results obtained in the two regularization schemes. The IR singularities, in the two regularization schemes are related as

$$\frac{1}{\epsilon} \leftrightarrow \ln(m^2), \quad \frac{2}{\epsilon^2} \leftrightarrow \ln^2(m^2). \quad (\text{B.31})$$

We would also like to mention that the finite parts of the box scalar integrals which involve di-logs/Spence functions may lead to numerical instability in their present form, due to a large cancellation among di-log terms. This problem can be cured to a certain level by putting them in different forms using di-log identities. In this thesis, we have used only divergent pieces of these integrals to make finiteness checks on amplitudes. Finite numerical results are presented using the FF/ OneLOop library of scalar integrals [84, 114].

For the case of massive internal lines, we are also interested in the large m^2 limit. In this limit, the basic scalar integrals are

$$B_0(m^2 \rightarrow \infty) = \frac{i}{16\pi^2} \left[\Delta_m + \mathcal{O}\left(\frac{1}{m^2}\right) \right], \quad (\text{B.32})$$

$$C_0(m^2 \rightarrow \infty) = \frac{i}{16\pi^2} \left[-\frac{1}{2m^2} + \mathcal{O}\left(\frac{1}{m^4}\right) \right], \quad (\text{B.33})$$

$$D_0(m^2 \rightarrow \infty) = \frac{i}{16\pi^2} \left[\frac{1}{6m^4} + \mathcal{O}\left(\frac{1}{m^6}\right) \right]. \quad (\text{B.34})$$

The non-leading terms will depend upon non-zero kinematic invariants of the scalars.

B.3 Derivation of pentagon scalar integral, E_0

We are interested in the case of equal masses for all the internal lines. This is not to simplify the derivation. The derivation can be carried out using 4-dimensional *Schouten identity* [58]. This identity is a result of the statement that $\varepsilon^{\mu_1\mu_2\mu_3\mu_4\alpha}$ is zero in 4 dimensions. Therefore antisymmetric combination of $\varepsilon^{\mu_1\mu_2\mu_3\mu_4}$ and l^α should vanish. This implies,

$$l^\alpha \varepsilon^{\mu_1\mu_2\mu_3\mu_4} = l^{\mu_1} \varepsilon^{\alpha\mu_2\mu_3\mu_4} + l^{\mu_2} \varepsilon^{\mu_1\alpha\mu_3\mu_4} + l^{\mu_3} \varepsilon^{\mu_1\mu_2\alpha\mu_4} + l^{\mu_4} \varepsilon^{\mu_1\mu_2\mu_3\alpha}. \quad (\text{B.35})$$

Schouten identity can also be derived by evaluating, $\text{tr}(\gamma^{\mu_1}\gamma^{\mu_2}\gamma^{\mu_3}\gamma^{\mu_4}\gamma^\alpha \not{l}\gamma^5)$ in 4 dimensions. In the case of 5-point function, we have four linearly independent

momenta p_1, p_2, p_3 and p_4 . In this derivation, it is more convenient to consider their linear combinations q_1, q_2, q_3 and q_4 , defined in chapter 2. Multiplying the above equation by $q_1^{\mu_1} q_2^{\mu_2} q_3^{\mu_3} q_4^{\mu_4}$, we get

$$\begin{aligned} l^\alpha \varepsilon^{q_1 q_2 q_3 q_4} &= l \cdot q_1 \varepsilon^{\alpha q_2 q_3 q_4} + l \cdot q_2 \varepsilon^{q_1 \alpha q_3 q_4} + l \cdot q_3 \varepsilon^{q_1 q_2 \alpha q_4} + l \cdot q_4 \varepsilon^{q_1 q_2 q_3 \alpha} \\ \text{or } l^\alpha &= \sum_{i=1}^4 l \cdot q_i u_i^\alpha, \end{aligned} \quad (\text{B.36})$$

where u_i s are dual vectors of q_i s, satisfying $u_i \cdot q_j = \delta_{ij}$ (clarify with Eq. 2.22). This is the same expression as in Eq. 2.31, with $m = 4$ and $\omega_l^\mu = 0$ but with different basis vectors. Contracting with l_α both the sides in Eq. B.36, we get

$$\begin{aligned} l^2 &= \sum_{i=1}^4 l \cdot q_i l \cdot u_i \\ \Rightarrow d_0 + m^2 &= \frac{1}{2} \sum_{i=1}^4 l \cdot u_i (d_i - d_0 - r_i) \\ \text{or } 2m^2 + (2 + \sum_{i=1}^4 l \cdot u_i) d_0 + l \cdot w &= \sum_{i=1}^4 l \cdot u_i d_i, \end{aligned} \quad (\text{B.37})$$

where $r_i = q_i^2$ and $w^\mu = \sum_{i=1}^4 r_i u_i^\mu$. Dividing both sides by $d_0 d_1 d_2 d_3 d_4$ and integrating over $d^4 l$, we get

$$\int d^4 l \frac{2m^2 + (2 + \sum_{i=1}^4 l \cdot u_i) d_0 + l \cdot w}{d_0 d_1 d_2 d_3 d_4} = 0. \quad (\text{B.38})$$

The contribution from the right hand side of Eq. B.37 is zero, because $\int d^4 l (l^\mu d_i / d_0 d_1 d_2 d_3 d_4)$, is a linear combination of those q_i s which are already present in the definition of the corresponding u_i s. Further, note that

$$\begin{aligned} \sum_{i=1}^4 u_i^\mu &= (\varepsilon^{\mu q_2 q_3 q_4} + \varepsilon^{q_1 \mu q_3 q_4} + \varepsilon^{q_1 q_2 \mu q_4} + \varepsilon^{q_1 q_2 q_3 \mu}) / \varepsilon^{q_1 q_2 q_3 q_4} \\ &= \varepsilon^{\mu(q_2 - q_1)(q_3 - q_2)(q_4 - q_3)} / \varepsilon^{q_1(q_2 - q_1)(q_3 - q_2)(q_4 - q_3)} \\ &= \varepsilon^{\mu p_2 p_3 p_4} / \varepsilon^{p_1 p_2 p_3 p_4} = v_1^\mu. \end{aligned} \quad (\text{B.39})$$

Also, shifting the loop momentum $l \rightarrow l - q_1$ ² in the second term of Eq. B.38,

$$\int d^4 l \frac{(2 + \sum_{i=1}^4 l \cdot u_i)}{d_1 d_2 d_3 d_4} = \int d^4 l \frac{(1 + \sum_{i=1}^4 l \cdot u_i)}{d_0 d'_1 d'_2 d'_3} = \int d^4 l \frac{(1 + l \cdot v_1)}{d_0 d'_1 d'_2 d'_3}. \quad (\text{B.40})$$

²Note that the loop integral is UV finite.

Here $d'_1 = (l + q_2 - q_1)^2 - m^2$, $d'_2 = (l + q_3 - q_1)^2 - m^2$ and $d'_3 = (l + q_4 - q_1)^2 - m^2$. Once again, since $\int d^4l (l^\mu/d_0 d'_1 d'_2 d'_3)$ is a linear combination of p_2, p_3 and p_4 , the $l.v_1$ term in the above equation does not contribute. Finally, we concentrate on the last term of the Eq. B.38. Using Eq. B.36, we write

$$\begin{aligned} l.w &= \sum_{i=1}^4 l.q_i u_i.w = \frac{1}{2} \sum_{i=1}^4 (d_i - d_0 - r_i) u_i.w \\ &= \frac{1}{2} \sum_{i=1}^4 d_i(u_i.w) - d_0(v_1.w) - w^2. \end{aligned} \quad (\text{B.41})$$

Substituting all these results in Eq. B.38, we get

$$\begin{aligned} \int d^4l \frac{4m^2 - w^2 + (2 - v_1.w)d_0 + \sum_{i=1}^4 (u_i.w)d_i}{d_0 d_1 d_2 d_3 d_4} &= 0 \\ \Rightarrow E_0 &= \frac{1}{w^2 - 4m^2} \left((2 - v_1.w)D_0^{(0)} + \sum_{i=1}^4 (u_i.w)D_0^{(i)} \right), \end{aligned} \quad (\text{B.42})$$

which is the desired relation mentioned in Eq. 2.5. In $n = 4 - 2\epsilon$ dimensions, this identity is expected to receive $\mathcal{O}(\epsilon)$ correction. This correction is proportional to 5-point scalar integral in $n = 6 - 2\epsilon$ dimensions [60]. It may appear that this $\mathcal{O}(\epsilon)$ piece could be important in the n -dimensional reduction of 5-point tensor integrals of rank $m \geq 2$ and we may require its explicit form. It has been argued (and shown explicitly in some special cases) in Ref. [60], that the $\mathcal{O}(\epsilon)$ piece is dropped out in the reduction of five-point tensor integrals with rank ≤ 5 . A general proof is given in Ref. [126]. Thus, the tensor reduction of five-point functions can be carried out in $n = 4$ dimensions without any ambiguity. In the case of five-point fermion loop amplitudes, considered in this thesis, precise arguments can be given to justify the five-point tensor reduction in 4 dimensions; refer to Sec. 2.3.2.

In the above expression of E_0 , We can also take the large m^2 limit. Using the large m^2 limit of the box scalars, given in Eq. B.34, we get

$$\begin{aligned} E_0(m^2 \rightarrow \infty) &= \frac{1}{(-4m^2)} 2 D_0(m^2 \rightarrow \infty) \\ &= \frac{i}{16\pi^2} \left[-\frac{1}{12m^6} + \mathcal{O}\left(\frac{1}{m^8}\right) \right]. \end{aligned} \quad (\text{B.43})$$

Appendix C

C.1 Examples of fermion loop triangle amplitudes

We would like to give two specific and simple examples of fermion loop amplitudes. These examples will complement the discussion presented in Sec. 2.3.2, on the special features of fermion loop amplitudes.

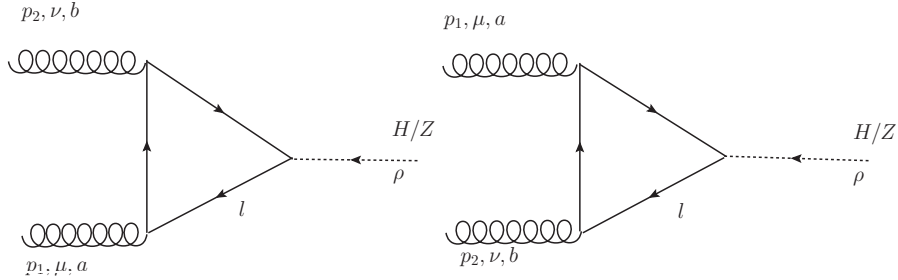


Figure C.1: Feynman diagrams for $gg \rightarrow H/Z$. The dashed line may represent the Higgs boson or the Z boson. The 4-vector index ρ is applicable in the $gg \rightarrow Z$ case only.

C.1.1 ggH amplitude; $p_1^2 \neq 0, p_2^2 \neq 0$

Ignoring the color and coupling factors etc., the tensor structure of the amplitude may be written as

$$\mathcal{M}^{\mu\nu}(p_1, p_2) = m^2 \left[F_0(p_1, p_2) g^{\mu\nu} + F_1(p_1, p_2) p_1^\mu p_1^\nu + F_2(p_1, p_2) p_2^\mu p_2^\nu + F_3(p_1, p_2) p_1^\mu p_2^\nu + F_4(p_1, p_2) p_2^\mu p_1^\nu \right]. \quad (\text{C.1})$$

The form factors $\{F_i\}$ are obtained by calculating the triangle diagrams shown in Fig. C.1. The two diagrams are related by charge-conjugation and they are equal. The gauge invariance with respect to the gluon currents, *i.e.*, $\mathcal{M}^{\mu\nu}p_{1\mu} = \mathcal{M}^{\mu\nu}p_{2\nu} = 0$, relates these form factors. The independent form factors are:

$$\begin{aligned} F_0(p_1, p_2) &= F_0(p_2, p_1) \\ &= -4 \frac{p_1^2}{\Delta_2} (p_2^2 + p_1 \cdot p_2) R_1 - 4 \frac{p_2^2}{\Delta_2} (p_1^2 + p_1 \cdot p_2) R_2 + \\ &\quad (4 s p_1^2 p_2^2 / \Delta_2 + 16 m^2 - 8 p_1 \cdot p_2) C_0 + 8 R, \end{aligned} \quad (\text{C.2})$$

$$\begin{aligned} F_1(p_1, p_2) &= (-p_2^2 / p_1 \cdot p_2) F_3(p_1, p_2), \\ F_2(p_1, p_2) &= F_1(p_2, p_1), \end{aligned} \quad (\text{C.3})$$

$$\begin{aligned} F_3(p_1, p_2) &= F_3(p_2, p_1) \\ &= \left[-12p_1^2 p_2^2 (p_1^2 + p_1 \cdot p_2) / (\Delta_2)^2 + 4(3p_1^2 + 2p_1 \cdot p_2) / \Delta_2 \right] R_1 + \\ &\quad \left[-12p_1^2 p_2^2 (p_2^2 + p_1 \cdot p_2) / (\Delta_2)^2 + 4(3p_2^2 + 2p_1 \cdot p_2) / \Delta_2 \right] R_2 + \\ &\quad \left[-12p_1^2 p_2^2 ((p_1^2 + p_2^2) p_1 \cdot p_2 + 2p_1^2 p_2^2) / (\Delta_2)^2 + \right. \\ &\quad \left. 8((p_1^2 + p_2^2 + 2m^2) p_1 \cdot p_2 + 4p_1^2 p_2^2) / \Delta_2 - 8 \right] C_0 + 8 p_1 \cdot p_2 / \Delta_2 R, \end{aligned} \quad (\text{C.4})$$

$$\begin{aligned} F_4(p_1, p_2) &= F_4(p_2, p_1) \\ &= F_3(p_1, p_2) - 8 (p_1^2 + p_1 \cdot p_2) / \Delta_2 R_1 - 8 (p_2^2 + p_1 \cdot p_2) / \Delta_2 R_2 + \\ &\quad \left[-8((p_1^2 + p_2^2) p_1 \cdot p_2 + 2p_1^2 p_2^2) / \Delta_2 + 16 \right] C_0, \end{aligned} \quad (\text{C.5})$$

with

$$\begin{aligned} R_1 &= B_0(1) - B_0(2), \\ R_2 &= B_0(1) - B_0(0). \end{aligned} \quad (\text{C.6})$$

In the above, $R (= 1)$ is used as a flag to identify rational terms and $\Delta_2 = p_1^2 p_2^2 - (p_1 \cdot p_2)^2$. Note that all these coefficients are UV finite and they vanish in the decoupling limit. We see that, after taking out the overall factor of m^2 , the rational part of the amplitude is independent of the quark mass. Therefore, as we described in

Sec. 2.3.2, the rational part can be calculated utilizing the decoupling theorem even in amplitudes involving a Higgs boson. For the special case of $p_1^2 = p_2^2 = 0$,

$$\mathcal{M}^{\mu\nu}(p_1, p_2) = m^2 (g^{\mu\nu} - p_2^\mu p_1^\nu / p_1 \cdot p_2) [8 R + (16m^2 - 8p_1 \cdot p_2) C_0]. \quad (\text{C.7})$$

In the $m^2 \rightarrow \infty$ limit, this amplitude reduces to an effective ggH -vertex,

$$i\mathcal{M}_{ab}^{\mu\nu}(gg \rightarrow H)|_{m \rightarrow \infty} = \delta^{ab} \frac{\alpha_s}{3\pi v} (p_1 \cdot p_2 g^{\mu\nu} - p_2^\mu p_1^\nu), \quad (\text{C.8})$$

where we have also included the couplings and the color factor. This is only the leading effect, obtained by expanding C_0 up to $\mathcal{O}(1/m^4)$ term.

C.1.2 ggZ amplitude; $p_1^2 \neq 0, p_2^2 \neq 0$

Since the vector part of the amplitude vanishes due to Furry's theorem, the most general form of the amplitude, consistent with the vector current conservation, can be expressed as

$$\begin{aligned} \mathcal{M}^{\mu\nu\rho}(p_1, p_2) = & F_1(p_1, p_2) \left[p_1^\mu \varepsilon^{\nu\rho p_1 p_2} - p_1^2 \varepsilon^{\mu\nu\rho p_2} \right] + F_2(p_1, p_2) \left[p_2^\nu \varepsilon^{\mu\rho p_1 p_2} - p_2^2 \varepsilon^{\mu\nu\rho p_1} \right] \\ & + F_3(p_1, p_2) (p_1 + p_2)^\rho \varepsilon^{\mu\nu p_1 p_2} + F_4(p_1, p_2) (p_1 - p_2)^\rho \varepsilon^{\mu\nu p_1 p_2} \end{aligned} \quad (\text{C.9})$$

where, due to symmetry

$$F_4(p_1, p_2) = 0, \quad F_1(p_1, p_2) = -F_2(p_2, p_1). \quad (\text{C.10})$$

Here we are not concerned about the overall factors of coupling and color. To obtain these form factors, we need to calculate the linearly divergent triangle diagrams, shown in Fig. C.1, in the presence of γ^5 . We can use any of the n -dimensional γ^5 prescriptions, given in the next section, to perform the full calculation in $n = 4 - 2\epsilon$ dimensions. The form factors thus obtained are:

$$\begin{aligned} F_2(p_1, p_2) = & \left[-6p_1^2((p_1^2 + p_2^2)p_1 \cdot p_2 + 2p_1^2 p_2^2)/(\Delta_2)^2 + 10p_1^2/\Delta_2 \right] R_1 + \\ & \left[-6sp_1^2 p_2^2/(\Delta_2)^2 + 2(p_1^2 + s)/\Delta_2 \right] R_2 + \\ & \left[-6p_1^2 p_2^2(p_1^2(p_1^2 + 3p_2^2 + 3p_1 \cdot p_2) + p_2^2 p_1 \cdot p_2)/(\Delta_2)^2 + \right. \\ & \left. 4(p_1^2(p_1^2 + 4p_2^2 + 2p_1 \cdot p_2) + 2m^2(p_1^2 + p_1 \cdot p_2))/\Delta_2 \right] C_0 + \\ & 4(p_1^2 + p_1 \cdot p_2)/\Delta_2 R, \end{aligned} \quad (\text{C.11})$$

$$\begin{aligned}
F_3(p_1, p_2) &= F_3(p_2, p_1) \\
&= [6p_1^2 p_2^2 (p_1^2 + p_1 \cdot p_2) / (\Delta_2)^2 - 2p_1^2 / \Delta_2] R_1 + \\
&\quad [6p_1^2 p_2^2 (p_2^2 + p_1 \cdot p_2) / (\Delta_2)^2 - 2p_2^2 / \Delta_2] R_2 + \\
&\quad [6p_1^2 p_2^2 ((p_1^2 + p_2^2) p_1 \cdot p_2 + 2p_1^2 p_2^2) / (\Delta_2)^2 - \\
&\quad 8(p_1^2 p_2^2 + m^2 p_1 \cdot p_2) / \Delta_2] C_0 - 4p_1 \cdot p_2 / \Delta_2 R.
\end{aligned} \tag{C.12}$$

Once again, we see that the rational terms are independent of the quark mass, and the amplitude vanishes in the decoupling limit as a result of the cancellation between the rational part and the non-rational part of the amplitude. We can calculate the anomalous contribution to the axial-vector current by dotting the amplitude with $(p_1 + p_2)^\rho$,

$$\mathcal{M}^{\mu\nu\rho}(p_1, p_2)(p_1 + p_2)_\rho = (16m^2 C_0 + 8 R) \varepsilon^{\mu\nu p_1 p_2}. \tag{C.13}$$

The first term on the right side of the above equation, shows the explicit breaking of the chiral symmetry due the quark mass and therefore non-conservation of the axial-vector current. Nevertheless, it goes away in the massless quark limit. The second term is the anomalous contribution and it is independent of the quark mass. The flag R , confirms that the anomaly affects only the rational part of the amplitude. The non-conservation of the axial-vector current, even in the massless fermion limit, is the famous *chiral anomaly* of VVA -triangle diagrams [142, 143]. For on-shell gluons and the Z boson,

$$\begin{aligned}
\mathcal{M}^{\mu\nu\rho}(p_1, p_2) &= \frac{1}{p_1 \cdot p_2} (8m^2 C_0 + 4 R) \varepsilon^{\mu\nu p_1 p_2} (p_1 + p_2)^\rho, \\
\Rightarrow \mathcal{M}(Z \rightarrow gg) &\equiv \mathcal{M}^{\mu\nu\rho}(p_1, p_2) e_{1\mu} e_{2\nu} e_{3\rho} = 0.
\end{aligned} \tag{C.14}$$

Here $\{e_i\}$ are polarization vectors of the gauge bosons and we have used, $e_3 \cdot (p_1 + p_2) = -e_3 \cdot p_3 = 0$, for the Z boson. This is the statement of the Landau-Yang theorem, that is, a spin-1 massive particle cannot decay into two massless spin-1 particles [144, 145]. Although we have proved it in a one-loop calculation, the Landau-Yang theorem is an exact quantum mechanical statement and it should be valid to all orders in perturbation theory. In the above, if the Z boson is off-shell, the 4-current (j^ρ) attached to it can be treated, symbolically, as its polarization vector. Therefore, as long as this current is conserved, *i.e.*, $j^\rho(p_1 + p_2)_\rho = 0$, the ggZ -amplitude with on-shell gluons, but off-shell Z boson, will also vanish.

C.2 γ^5 in n dimensions

We discussed in Sec. 2.3.2 that the chiral anomaly, in linearly divergent fermion loop amplitudes, should be regulated by using an n -dimensional prescription for γ^5 in trace calculations, to ensure the conservation of vector currents and other symmetries of amplitudes. In 4 dimensions, γ^5 anticommutes with all other gamma-matrices, *i.e.*, $\{\gamma^5, \gamma^\mu\} = 0$. In n dimensions, the cyclic property of the trace of a string of gamma-matrices with a γ^5 is not compatible with this anticommutation relation [146]. Noting that, in n dimensions

$$\gamma^\alpha (\gamma^\mu \gamma^\nu \gamma^\rho \gamma^\sigma) \gamma_\alpha = 2\gamma^\nu \gamma^\rho \gamma^\sigma \gamma^\mu + 2\gamma^\mu \gamma^\sigma \gamma^\rho \gamma^\nu + (n-4)\gamma^\mu \gamma^\nu \gamma^\rho \gamma^\sigma, \quad (\text{C.15})$$

we can write

$$\begin{aligned} \text{tr} [\gamma^5 \gamma^\alpha (\gamma^\mu \gamma^\nu \gamma^\rho \gamma^\sigma) \gamma_\alpha] &= 2 \text{tr} [\gamma^5 \gamma^\nu \gamma^\rho \gamma^\sigma \gamma^\mu] + 2 \text{tr} [\gamma^5 \gamma^\mu \gamma^\sigma \gamma^\rho \gamma^\nu] \\ &\quad + (n-4) \text{tr} [\gamma^5 \gamma^\mu \gamma^\nu \gamma^\rho \gamma^\sigma]. \end{aligned} \quad (\text{C.16})$$

On the other hand, assuming the anticommuting property of γ^5 and using the cyclic property of the trace,

$$\text{tr} [\gamma^5 \gamma^\alpha (\gamma^\mu \gamma^\nu \gamma^\rho \gamma^\sigma) \gamma_\alpha] = -n \text{tr} [\gamma^5 \gamma^\mu \gamma^\nu \gamma^\rho \gamma^\sigma]. \quad (\text{C.17})$$

Here we have used $\gamma^\mu \gamma_\mu = n$. Combining the above two results, we get

$$(n-4) \text{tr} [\gamma^5 \gamma^\mu \gamma^\nu \gamma^\rho \gamma^\sigma] = 0, \quad (\text{C.18})$$

where we used, $\text{tr} [\gamma^\sigma \gamma^\rho \gamma^\nu \gamma^\mu \gamma^5] = \text{tr} [\gamma^5 \gamma^\mu \gamma^\nu \gamma^\rho \gamma^\sigma]$. The final result, clearly, makes sense only in 4 dimensions and therefore we must have a prescription for γ^5 in n dimensions. The two very common prescriptions, in the literature, are:

1. The 't Hooft-Veltman prescription: [147]

In this prescription, the n dimensional γ^μ -matrices are broken into 4-dimensional and $(n-4)$ -dimensional parts such that γ^5 anticommutes with the 4-dimensional part while it commutes with the $(n-4)$ -dimensional part, *i.e.*,

$$\{\gamma_{(4)}^\mu, \gamma^5\} = 0, \quad [\gamma_{(n-4)}^\mu, \gamma^5] = 0. \quad (\text{C.19})$$

where $\gamma_{(4)}^\mu = \gamma^\mu; \mu = 0, 1, 2, 3$ and $\gamma_{(n-4)}^\mu = \gamma^\mu; \mu = 4, 5, \dots, n$. Furthermore, all the external momenta and polarizations are taken in 4 dimensions. However, the loop momentum remains in n dimensions. Thus,

$$\gamma.l = \gamma^\mu l_\mu = \gamma_{(4)}^\mu l_{(4)\mu} + \gamma_{(n-4)}^\mu l_{(n-4)\mu}. \quad (\text{C.20})$$

2. The Larin's prescription: [113]

This prescription is very straightforward and one uses

$$\gamma^5 = -\frac{i}{4!} \varepsilon_{\mu\nu\rho\sigma} \gamma^\mu \gamma^\nu \gamma^\rho \gamma^\sigma, \quad (\text{C.21})$$

in the fermion loop trace calculation. In this way of writing γ^5 , its 4-dimensional nature is restricted to the fully antisymmetric ε -tensor, which can be multiplied after calculating the trace in n -dimensions. The trace expression gets very lengthy with the above γ^5 . We can use a simpler and more practical form,

$$\gamma_\mu \gamma^5 = -\frac{i}{3!} \varepsilon_{\mu\nu\rho\sigma} \gamma^\nu \gamma^\rho \gamma^\sigma. \quad (\text{C.22})$$

We have used both these prescriptions to calculate the ggZ -amplitude, discussed above. Both these prescriptions generate correct rational terms, consistent with the desired symmetries of the amplitude and the decoupling theorem. We would like to further comment that special prescriptions for γ^5 may be required, if there are odd number of γ^5 -matrices in the trace. The 4-dimensional anticommuting property of γ^5 can be used safely, in presence of even number of γ^5 -matrices in the trace.

Appendix D

D.1 Feynman rules

We have given here the ADD model Feynman rules for those vertices which appear in our processes considered in chapter 4; see Figs. D.1 and D.2. These are taken from the Ref. [48]. The tensor structures which appear in these rules are given by

$$C_{\mu\nu,\rho\sigma} = g_{\mu\rho}g_{\nu\sigma} + g_{\mu\sigma}g_{\nu\rho} - g_{\mu\nu}g_{\rho\sigma}, \quad (\text{D.1})$$

$$D_{\mu\nu,\rho\sigma}(k_1, k_2) = g_{\mu\nu}k_{1\sigma}k_{2\rho} - \left[g_{\mu\sigma}k_{1\nu}k_{2\rho} + g_{\mu\rho}k_{1\sigma}k_{2\nu} - g_{\rho\sigma}k_{1\mu}k_{2\nu} + (\mu \leftrightarrow \nu) \right], \quad (\text{D.2})$$

$$E_{\mu\nu,\rho\sigma}(k_1, k_2) = g_{\mu\nu}(k_{1\rho}k_{1\sigma} + k_{2\rho}k_{2\sigma} + k_{1\rho}k_{2\sigma}) - \left[g_{\nu\sigma}k_{1\mu}k_{1\rho} + g_{\nu\rho}k_{2\mu}k_{2\sigma} + (\mu \leftrightarrow \nu) \right]. \quad (\text{D.3})$$

Note that for the on-shell production of the KK-graviton, the terms proportional to $g_{\mu\nu}$ do not contribute due to the traceless condition of the graviton polarization tensor. The SM Feynman rules used in thesis are taken from [52].

$$\begin{aligned}
& \text{Diagram 1: Two solid lines with momenta } k_1 \text{ and } k_2 \text{ meeting at a vertex, with a zig-zag line (KK-graviton) extending from the vertex.} \\
& \quad : \quad -i\frac{\kappa}{8}[\gamma_\mu(k_1 + k_2)_\nu + \gamma_\nu(k_1 + k_2)_\mu - 2g_{\mu\nu}(\not{k}_1 + \not{k}_2 - 2m_f)] \\
& \text{Diagram 2: Two dashed lines with momenta } k_1 \text{ and } k_2 \text{ meeting at a vertex, with a zig-zag line (KK-graviton) extending from the vertex.} \\
& \quad : \quad -i\frac{\kappa}{2}[M_H^2 g_{\mu\nu} + C_{\mu\nu,\rho\sigma} k_1^\sigma k_2^\sigma] \\
& \text{Diagram 3: Two curly lines with momenta } k_1 \text{ and } k_2 \text{ meeting at a vertex, with a zig-zag line (KK-graviton) extending from the vertex.} \\
& \quad : \quad -i\frac{\kappa}{2} \delta^{ab} [(M_A^2 + k_1 \cdot k_2) C_{\mu\nu,\rho\sigma} + D_{\mu\nu,\rho\sigma}(k_1, k_2) + \frac{1}{\xi} E_{\mu\nu,\rho\sigma}(k_1, k_2)]
\end{aligned}$$

Figure D.1: Feynman rules for 3-point vertices in the ADD model. The zig-zag line denotes the KK-graviton. The dashed line is for the Higgs boson while the curly line may denote any gauge boson with mass M_A . $\kappa = \sqrt{16\pi G_N} = \sqrt{2}/M_P$, and ξ is the gauge-fixing parameter.

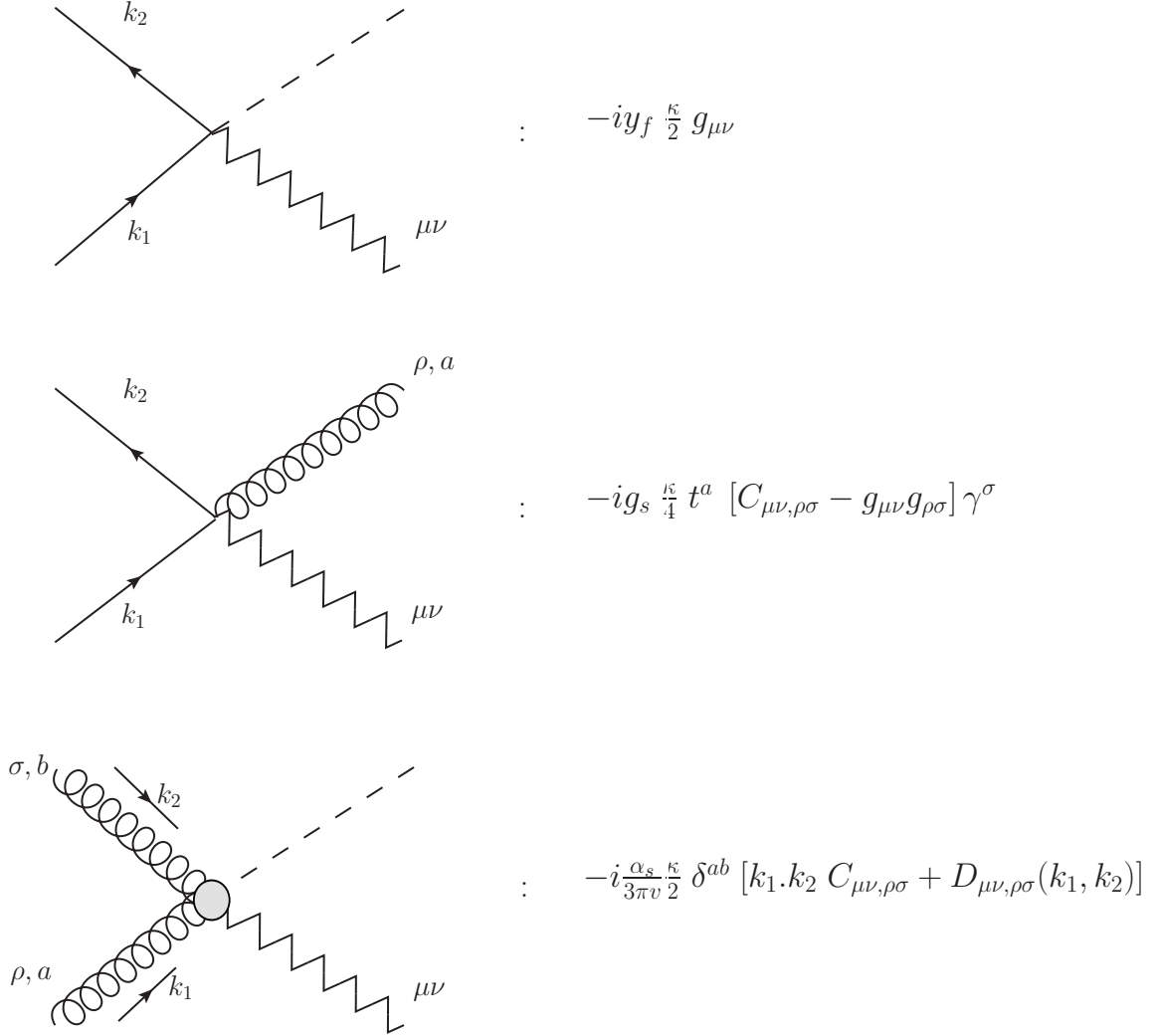


Figure D.2: Feynman rules for some of the 4-point vertices in the ADD model. The Yukawa coupling, $y_f = \frac{1}{2}g_w(m_f/M_W)$. The last vertex is derived in an effective theory of ggH coupling.

Bibliography

- [1] **CDF** Collaboration, T. Aaltonen *et al.*, “Evidence for a Mass Dependent Forward-Backward Asymmetry in Top Quark Pair Production,” *Phys.Rev.* **D83** (2011) 112003, [arXiv:1101.0034 \[hep-ex\]](#).
- [2] **Muon G-2** Collaboration, G. Bennett *et al.*, “Final Report of the Muon E821 Anomalous Magnetic Moment Measurement at BNL,” *Phys.Rev.* **D73** (2006) 072003, [arXiv:hep-ex/0602035 \[hep-ex\]](#).
- [3] **Particle Data Group** Collaboration, J. Beringer *et al.*, “Review of Particle Physics (RPP),” *Phys.Rev.* **D86** (2012) 010001. and references therein.
- [4] <http://www.fnal.gov/pub/tevatron/milestones/interactive-timeline.html>.
- [5] **TEVNPH (Tevatron New Phenomena and Higgs Working Group), CDF & D0** Collaboration, “Combined CDF and D0 Search for Standard Model Higgs Boson Production with up to 10.0 fb^{-1} of Data,” [arXiv:1203.3774 \[hep-ex\]](#).
- [6] **CMS** Collaboration, D. Green, “Rediscovering’ the standard model at CMS,” *Mod.Phys.Lett.* **A26** (2011) 309–317.
- [7] <http://press.web.cern.ch/press-releases/2012/07/cern-experiments-observe-particle-consistent-long-sought-higgs-boson>.
- [8] **ATLAS** Collaboration, G. Aad *et al.*, “Observation of a new particle in the search for the Standard Model Higgs boson with the ATLAS detector at the LHC,” *Phys.Lett.* **B716** (2012) 1–29, [arXiv:1207.7214 \[hep-ex\]](#).

- [9] **CMS** Collaboration, S. Chatrchyan *et al.*, “Observation of a new boson at a mass of 125 GeV with the CMS experiment at the LHC,” *Phys.Lett.* **B716** (2012) 30–61, [arXiv:1207.7235 \[hep-ex\]](#).
- [10] **ATLAS** Collaboration, G. Aad *et al.*, “Observation of a new χ_b state in radiative transitions to $\Upsilon(1S)$ and $\Upsilon(2S)$ at ATLAS,” *Phys.Rev.Lett.* **108** (2012) 152001, [arXiv:1112.5154 \[hep-ex\]](#).
- [11] **CMS** Collaboration, S. Chatrchyan *et al.*, “Observation of a new $\Xi(b)$ baryon,” *Phys.Rev.Lett.* **108** (2012) 252002, [arXiv:1204.5955 \[hep-ex\]](#).
- [12] K. Jakobs, “Physics at the LHC – From Standard Model measurements to Searches for New Physics,” [arXiv:1206.7024 \[hep-ex\]](#).
- [13] S. Nahn and D. Tsybychev, “Recent results from ATLAS and CMS on Higgs, supersymmetry and physics beyond the standard model searches,” *Int.J.Mod.Phys.* **A27** (2012) 1230020.
- [14] D. Adams, “Search for physics beyond the standard model at ATLAS and CMS,”. ATL-PHYS-PROC-2012-055, ATL-COM-PHYS-2012-337.
- [15] G. Rolandi, “LHC Results - Highlights,” [arXiv:1211.3718 \[hep-ex\]](#).
- [16] T.-P. Cheng and L.-F. Li, *Gauge Theory of Elementary Particle Physics*. Oxford University Press, Oxford, indian ed., 2007.
- [17] E. Abers and B. Lee, “Gauge Theories,” *Phys.Rept.* **9** (1973) 1–141.
- [18] P. W. Higgs, “Broken symmetries, massless particles and gauge fields,” *Phys.Lett.* **12** (1964) 132–133.
- [19] P. W. Higgs, “Broken Symmetries and the Masses of Gauge Bosons,” *Phys.Rev.Lett.* **13** (1964) 508–509.
- [20] F. Englert and R. Brout, “Broken Symmetry and the Mass of Gauge Vector Mesons,” *Phys.Rev.Lett.* **13** (1964) 321–323.
- [21] G. Guralnik, C. Hagen, and T. Kibble, “Global Conservation Laws and Massless Particles,” *Phys.Rev.Lett.* **13** (1964) 585–587.

- [22] P. W. Higgs, “Spontaneous Symmetry Breakdown without Massless Bosons,” *Phys.Rev.* **145** (1966) 1156–1163.
- [23] T. Kibble, “Symmetry breaking in nonAbelian gauge theories,” *Phys.Rev.* **155** (1967) 1554–1561.
- [24] **Super-Kamiokande** Collaboration, Y. Fukuda *et al.*, “Evidence for oscillation of atmospheric neutrinos,” *Phys.Rev.Lett.* **81** (1998) 1562–1567, [arXiv:hep-ex/9807003](#) [[hep-ex](#)].
- [25] M. Gonzalez-Garcia and M. Maltoni, “Phenomenology with Massive Neutrinos,” *Phys.Rept.* **460** (2008) 1–129, [arXiv:0704.1800](#) [[hep-ph](#)].
- [26] S. Glashow, “Partial Symmetries of Weak Interactions,” *Nucl.Phys.* **22** (1961) 579–588.
- [27] S. Weinberg, “A Model of Leptons,” *Phys.Rev.Lett.* **19** (1967) 1264–1266.
- [28] A. Salam, “in Elementary Particle Theory,” *The Nobel Symposium no. 8* (1968) 367.
- [29] G. ’t Hooft, “Renormalization of Massless Yang-Mills Fields,” *Nucl.Phys.* **B33** (1971) 173–199.
- [30] M. Kobayashi and T. Maskawa, “CP Violation in the Renormalizable Theory of Weak Interaction,” *Prog.Theor.Phys.* **49** (1973) 652–657.
- [31] T. Nakada, “Status and prospect of CP violation experiments,” *J.Phys.Conf.Ser.* **171** (2009) 012003.
- [32] S. Novaes, “Standard model: An Introduction,” [arXiv:hep-ph/0001283](#) [[hep-ph](#)].
- [33] L. Faddeev and V. Popov, “Feynman Diagrams for the Yang-Mills Field,” *Phys.Lett.* **B25** (1967) 29–30.
- [34] J. Callan, Curtis G., “Broken scale invariance in scalar field theory,” *Phys.Rev.* **D2** (1970) 1541–1547.

- [35] K. Symanzik, “Small distance behavior in field theory and power counting,” *Commun.Math.Phys.* **18** (1970) 227–246.
- [36] D. Gross and F. Wilczek, “Ultraviolet Behavior of Nonabelian Gauge Theories,” *Phys.Rev.Lett.* **30** (1973) 1343–1346.
- [37] H. D. Politzer, “Reliable Perturbative Results for Strong Interactions?,” *Phys.Rev.Lett.* **30** (1973) 1346–1349.
- [38] T. Muta, *Foundations of Quantum Chromodynamics*. World Scientific, Singapore, third ed., 2010.
- [39] **CTEQ** Collaboration, R. Brock *et al.*, “Handbook of perturbative QCD: Version 1.0,” *Rev.Mod.Phys.* **67** (1995) 157–248.
- [40] M. Bustamante, L. Cieri, and J. Ellis, “Beyond the Standard Model for Montaneros,” [arXiv:0911.4409 \[hep-ph\]](#).
- [41] I. Antoniadis, “A Possible new dimension at a few TeV,” *Phys.Lett.* **B246** (1990) 377–384.
- [42] N. Arkani-Hamed, S. Dimopoulos, and G. Dvali, “The Hierarchy problem and new dimensions at a millimeter,” *Phys.Lett.* **B429** (1998) 263–272, [arXiv:hep-ph/9803315 \[hep-ph\]](#).
- [43] I. Antoniadis, N. Arkani-Hamed, S. Dimopoulos, and G. Dvali, “New dimensions at a millimeter to a Fermi and superstrings at a TeV,” *Phys.Lett.* **B436** (1998) 257–263, [arXiv:hep-ph/9804398 \[hep-ph\]](#).
- [44] N. Arkani-Hamed, S. Dimopoulos, and G. Dvali, “Phenomenology, astrophysics and cosmology of theories with submillimeter dimensions and TeV scale quantum gravity,” *Phys.Rev.* **D59** (1999) 086004, [arXiv:hep-ph/9807344 \[hep-ph\]](#).
- [45] L. Randall and R. Sundrum, “A Large mass hierarchy from a small extra dimension,” *Phys.Rev.Lett.* **83** (1999) 3370–3373, [arXiv:hep-ph/9905221 \[hep-ph\]](#).

- [46] E. Ponton, “TASI 2011: Four Lectures on TeV Scale Extra Dimensions,” [arXiv:1207.3827 \[hep-ph\]](#). and references therein.
- [47] G. F. Giudice, R. Rattazzi, and J. D. Wells, “Quantum gravity and extra dimensions at high-energy colliders,” *Nucl.Phys.* **B544** (1999) 3–38, [arXiv:hep-ph/9811291 \[hep-ph\]](#).
- [48] T. Han, J. D. Lykken, and R.-J. Zhang, “On Kaluza-Klein states from large extra dimensions,” *Phys.Rev.* **D59** (1999) 105006, [arXiv:hep-ph/9811350 \[hep-ph\]](#).
- [49] E. A. Mirabelli, M. Perelstein, and M. E. Peskin, “Collider signatures of new large space dimensions,” *Phys.Rev.Lett.* **82** (1999) 2236–2239, [arXiv:hep-ph/9811337 \[hep-ph\]](#).
- [50] F. Close, “The quark parton model,” *Rep. Prog. Phys.* **42** (1979) 1285.
- [51] J. C. Collins, D. E. Soper, and G. F. Sterman, “Factorization of Hard Processes in QCD,” *Adv.Ser.Direct.High Energy Phys.* **5** (1988) 1–91, [arXiv:hep-ph/0409313 \[hep-ph\]](#). and references therein.
- [52] M. E. Peskin and D. V. Schroeder, *An Introduction to Quantum Field Theory*. Levant Books, Kolkata, paperback ed., 2005.
- [53] R. K. Ellis, W. J. Stirling, and B. R. Webber, *QCD and Collider Physics*. Cambridge University Press, UK, 2003. and references therein.
- [54] V. D. Barger and J. N. R. Phillips, *Collider Physics*. Westview Press, 1996.
- [55] D. Green, *High Pt Physics at Hadron Colliders*. Cambridge University Press, 2009.
- [56] D. Binosi, J. Collins, C. Kaufhold, and L. Theussl, “JaxoDraw: A Graphical user interface for drawing Feynman diagrams. Version 2.0 release notes,” *Comput.Phys.Commun.* **180** (2009) 1709–1715, [arXiv:0811.4113 \[hep-ph\]](#).
- [57] G. ’t Hooft and M. Veltman, “Scalar One Loop Integrals,” *Nucl.Phys.* **B153** (1979) 365–401.

- [58] W. van Neerven and J. Vermaseren, “Large Loop Integrals,” *Phys.Lett.* **B137** (1984) 241.
- [59] Z. Bern, L. J. Dixon, and D. A. Kosower, “Dimensionally regulated one loop integrals,” *Phys.Lett.* **B302** (1993) 299–308, [arXiv:hep-ph/9212308](#) [hep-ph].
- [60] Z. Bern, L. J. Dixon, and D. A. Kosower, “Dimensionally regulated pentagon integrals,” *Nucl.Phys.* **B412** (1994) 751–816, [arXiv:hep-ph/9306240](#) [hep-ph].
- [61] R. K. Ellis and G. Zanderighi, “Scalar one-loop integrals for QCD,” *JHEP* **0802** (2008) 002, [arXiv:0712.1851](#) [hep-ph]. and references therein.
- [62] G. Passarino and M. Veltman, “One Loop Corrections for e+ e- Annihilation Into mu+ mu- in the Weinberg Model,” *Nucl.Phys.* **B160** (1979) 151.
- [63] G. van Oldenborgh and J. Vermaseren, “New Algorithms for One Loop Integrals,” *Z.Phys.* **C46** (1990) 425–438.
- [64] J. Vermaseren, “New features of FORM,” [arXiv:math-ph/0010025](#) [math-ph].
- [65] A. Denner and S. Dittmaier, “Reduction of one loop tensor five point integrals,” *Nucl.Phys.* **B658** (2003) 175–202, [arXiv:hep-ph/0212259](#) [hep-ph].
- [66] R. K. Ellis, Z. Kunszt, K. Melnikov, and G. Zanderighi, “One-loop calculations in quantum field theory: from Feynman diagrams to unitarity cuts,” *Phys.Rept.* **518** (2012) 141–250, [arXiv:1105.4319](#) [hep-ph]. and references therein.
- [67] W. Beenakker, *Electroweak Corrections: Techniques and Applications*. Ph.d. thesis, University of Leiden.
- [68] T. Binoth, J. P. Guillet, and G. Heinrich, “Algebraic evaluation of rational polynomials in one-loop amplitudes,” *JHEP* **0702** (2007) 013, [arXiv:hep-ph/0609054](#) [hep-ph].

- [69] T. Kinoshita, “Mass singularities of Feynman amplitudes,” *J.Math.Phys.* **3** (1962) 650–677.
- [70] T. Appelquist and J. Carazzone, “Infrared Singularities and Massive Fields,” *Phys.Rev.* **D11** (1975) 2856.
- [71] P. Agrawal and A. Shivaji, “Multi Vector Boson Production via Gluon Fusion at the LHC,” *PoS RADCOR2011* (2012) 010, [arXiv:1201.0511 \[hep-ph\]](#).
- [72] P. Agrawal and A. Shivaji, “Di-Vector Boson + Jet Production via Gluon Fusion at Hadron Colliders,” *Phys.Rev.* **D86** (2012) 073013, [arXiv:1207.2927 \[hep-ph\]](#).
- [73] P. Agrawal and A. Shivaji, “Production of $\gamma Z g$ and associated processes via gluon fusion at hadron colliders,” *JHEP* **1301** (2013) 071, [arXiv:1208.2593 \[hep-ph\]](#).
- [74] D. A. Dicus, C. Kao, and W. Repko, “Gluon Production of Gauge Bosons,” *Phys.Rev.* **D36** (1987) 1570.
- [75] D. A. Dicus and S. S. Willenbrock, “Photon Pair Production and the Intermediate mass Higgs,”.
- [76] J. van der Bij and E. N. Glover, “Photon Z Boson Pair Production via Gluon Fusion,” *Phys.Lett.* **B206** (1988) 701.
- [77] E. N. Glover and J. van der Bij, “Z Boson Pair Production via Gluon Fusion,” *Nucl.Phys.* **B321** (1989) 561.
- [78] E. N. Glover and J. van der Bij, “Vector Boson Pair Production via Gluon Fusion,” *Phys.Lett.* **B219** (1989) 488.
- [79] J. M. Campbell, R. K. Ellis, and C. Williams, “Vector boson pair production at the LHC,” *JHEP* **1107** (2011) 018, [arXiv:1105.0020 \[hep-ph\]](#). and references therein.
- [80] J. M. Campbell, R. K. Ellis, and C. Williams, “Gluon-Gluon Contributions to $W^+ W^-$ Production and Higgs Interference Effects,” *JHEP* **1110** (2011) 005, [arXiv:1107.5569 \[hep-ph\]](#). and references therein.

- [81] D. de Florian and Z. Kunszt, “Two photons plus jet at LHC: The NNLO contribution from the $g g$ initiated process,” *Phys.Lett.* **B460** (1999) 184–188, [arXiv:hep-ph/9905283](#) [hep-ph].
- [82] P. Agrawal and G. Ladinsky, “Production of two photons and a jet through gluon fusion,” *Phys.Rev.* **D63** (2001) 117504, [arXiv:hep-ph/0011346](#) [hep-ph].
- [83] T. Melia, K. Melnikov, R. Rontsch, M. Schulze, and G. Zanderighi, “Gluon fusion contribution to $W+W^-$ + jet production,” [arXiv:1205.6987](#) [hep-ph].
- [84] A. van Hameren, “OneLOop: For the evaluation of one-loop scalar functions,” *Comput.Phys.Commun.* **182** (2011) 2427–2438, [arXiv:1007.4716](#) [hep-ph].
- [85] R. Kleiss, W. J. Stirling, and S. Ellis, “A New Monte Carlo Treatment of Multiparticle Phase Space at High-Energies,” *Comput.Phys.Commun.* **40** (1986) 359.
- [86] S. Veseli, “Multidimensional integration in a heterogeneous network environment,” *Comput.Phys.Commun.* **108** (1998) 9–19.
- [87] A. Geist *et al.*, *PVM: Parallel Virtual Machine*. MIT Press, Cambridge, MA, 1994.
- [88] P. M. Nadolsky, H.-L. Lai, Q.-H. Cao, J. Huston, J. Pumplin, *et al.*, “Implications of CTEQ global analysis for collider observables,” *Phys.Rev.* **D78** (2008) 013004, [arXiv:0802.0007](#) [hep-ph].
- [89] J. Alwall, M. Herquet, F. Maltoni, O. Mattelaer, and T. Stelzer, “MadGraph 5 : Going Beyond,” *JHEP* **1106** (2011) 128, [arXiv:1106.0522](#) [hep-ph].
- [90] J. M. Campbell, H. B. Hartanto, and C. Williams, “Next-to-leading order predictions for Z gamma+jet and Z gamma gamma final states at the LHC,” [arXiv:1208.0566](#) [hep-ph].

- [91] A. Denner and S. Dittmaier, “Reduction schemes for one-loop tensor integrals,” *Nucl.Phys.* **B734** (2006) 62–115, [arXiv:hep-ph/0509141](#) [[hep-ph](#)].
- [92] F. Campanario, “Towards $pp \rightarrow VVjj$ at NLO QCD: Bosonic contributions to triple vector boson production plus jet,” *JHEP* **1110** (2011) 070, [arXiv:1105.0920](#) [[hep-ph](#)].
- [93] A. Shivaji, S. Mitra, and P. Agrawal, “Associated Production of a KK-Graviton with a Higgs Boson via Gluon Fusion at the LHC,” *Eur.Phys.J.* **C72** (2012) 1922, [arXiv:1108.4561](#) [[hep-ph](#)].
- [94] S. Mitra, A. Shivaji, and P. Agrawal, “Production of a KK-graviton in association with a boson via gluon fusion at the LHC,” *PoS RADCOR2011* (2011) 045, [arXiv:1111.3785](#) [[hep-ph](#)].
- [95] A. Shivaji, V. Ravindran, and P. Agrawal, “Production of a KK-graviton and a Vector Boson in ADD Model via Gluon fusion,” *JHEP* **1202** (2012) 057, [arXiv:1111.6479](#) [[hep-ph](#)].
- [96] CMS Collaboration, S. Chatrchyan *et al.*, “Search for signatures of extra dimensions in the diphoton mass spectrum at the Large Hadron Collider,” [arXiv:1112.0688](#) [[hep-ex](#)].
- [97] CMS Collaboration, S. Chatrchyan *et al.*, “Search for large extra dimensions in dimuon and dielectron events in pp collisions at $\sqrt{s} = 7$ TeV,” *Phys.Lett.* **B711** (2012) 15–34, [arXiv:1202.3827](#) [[hep-ex](#)].
- [98] CMS Collaboration, S. Chatrchyan *et al.*, “Search for Dark Matter and Large Extra Dimensions in pp Collisions Yielding a Photon and Missing Transverse Energy,” *Phys.Rev.Lett.* **108** (2012) 261803, [arXiv:1204.0821](#) [[hep-ex](#)].
- [99] CMS Collaboration, S. Chatrchyan *et al.*, “Search for dark matter and large extra dimensions in monojet events in pp collisions at $\sqrt{s} = 7$ TeV,” *JHEP* **1209** (2012) 094, [arXiv:1206.5663](#) [[hep-ex](#)].

- [100] **ATLAS** Collaboration, G. Aad *et al.*, “Search for dark matter candidates and large extra dimensions in events with a photon and missing transverse momentum in pp collision data at $\sqrt{s} = 7$ TeV with the ATLAS detector,” [arXiv:1209.4625](#) [**hep-ex**].
- [101] **ATLAS** Collaboration, G. Aad *et al.*, “Search for dark matter candidates and large extra dimensions in events with a jet and missing transverse momentum with the ATLAS detector,” [arXiv:1210.4491](#) [**hep-ex**].
- [102] **ATLAS** Collaboration, G. Aad *et al.*, “Search for Extra Dimensions in diphoton events using proton-proton collisions recorded at $\sqrt{s} = 7$ TeV with the ATLAS detector at the LHC,” [arXiv:1210.8389](#) [**hep-ex**].
- [103] **ATLAS** Collaboration, G. Aad *et al.*, “Search for contact interactions and large extra dimensions in dilepton events from pp collisions at $\sqrt{s} = 7$ TeV with the ATLAS detector,” [arXiv:1211.1150](#) [**hep-ex**].
- [104] O. J. Eboli, T. Han, M. Magro, and P. Mercadante, “Diphoton signals for large extra dimensions at the Tevatron and CERN LHC,” *Phys.Rev.* **D61** (2000) 094007, [arXiv:hep-ph/9908358](#) [**hep-ph**].
- [105] K. M. Cheung and G. L. Landsberg, “Drell-Yan and diphoton production at hadron colliders and low scale gravity model,” *Phys.Rev.* **D62** (2000) 076003, [arXiv:hep-ph/9909218](#) [**hep-ph**].
- [106] P. Mathews, V. Ravindran, K. Sridhar, and W. van Neerven, “Next-to-leading order QCD corrections to the Drell-Yan cross section in models of TeV-scale gravity,” *Nucl.Phys.* **B713** (2005) 333–377, [arXiv:hep-ph/0411018](#) [**hep-ph**].
- [107] M. Kumar, P. Mathews, V. Ravindran, and A. Tripathi, “Diphoton signals in theories with large extra dimensions to NLO QCD at hadron colliders,” *Phys.Lett.* **B672** (2009) 45–50, [arXiv:0811.1670](#) [**hep-ph**].
- [108] S. Karg, M. Kramer, Q. Li, and D. Zeppenfeld, “NLO QCD corrections to graviton production at hadron colliders,” *Phys.Rev.* **D81** (2010) 094036, [arXiv:0911.5095](#) [**hep-ph**].

- [109] X. Gao, C. S. Li, J. Gao, J. Wang, and R. J. Oakes, “Next-to-leading order QCD predictions for graviton and photon associated production in the Large Extra Dimensions model at the LHC,” *Phys.Rev.* **D81** (2010) 036008, [arXiv:0912.0199 \[hep-ph\]](#).
- [110] M. Kumar, P. Mathews, V. Ravindran, and S. Seth, “Vector boson production in association with KK modes of the ADD model to NLO in QCD at LHC,” *J.Phys.G* **G38** (2011) 055001, [arXiv:1004.5519 \[hep-ph\]](#).
- [111] M. Kumar, P. Mathews, V. Ravindran, and S. Seth, “Graviton plus vector boson production to NLO in QCD at the LHC,” *Nucl.Phys.* **B847** (2011) 54–92, [arXiv:1011.6199 \[hep-ph\]](#).
- [112] M. Kumar, P. Mathews, V. Ravindran, and S. Seth, “Neutral triple electroweak gauge boson production in the large extra-dimension model at the LHC,” *Phys.Rev.* **D85** (2012) 094507, [arXiv:1111.7063 \[hep-ph\]](#).
- [113] S. Larin, “The renormalization of the axial anomaly in dimensional regularization,” *Phys.Lett.B* **303** (1992) 113–118.
- [114] G. van Oldenborgh, “FF: A Package to evaluate one loop Feynman diagrams,” *Comput.Phys.Comm.* **66** (1991) 1–15.
- [115] R. P. Kauffman, S. V. Desai, and D. Risal, “Production of a Higgs boson plus two jets in hadronic collisions,” *Phys.Rev.* **D55** (1997) 4005–4015, [arXiv:hep-ph/9610541 \[hep-ph\]](#).
- [116] S. Dawson, “Radiative corrections to Higgs boson production,” *Nucl.Phys.* **B359** (1991) 283–300.
- [117] A. Djouadi, M. Spira, and P. Zerwas, “Production of Higgs bosons in proton colliders: QCD corrections,” *Phys.Lett.* **B264** (1991) 440–446.
- [118] A. Pak, M. Rogal, and M. Steinhauser, “Finite top quark mass effects in NNLO Higgs boson production at LHC,” *JHEP* **1002** (2010) 025, [arXiv:0911.4662 \[hep-ph\]](#).

- [119] C. Anastasiou, *Two-loop integrals and QCD scattering*. Ph.d. thesis, University of Durham.
- [120] D. A. Kosower and K. J. Larsen, “Maximal Unitarity at Two Loops,” *Phys.Rev.* **D85** (2012) 045017, [arXiv:1108.1180 \[hep-th\]](#).
- [121] H. Johansson, D. A. Kosower, and K. J. Larsen, “Two-Loop Maximal Unitarity with External Masses,” [arXiv:1208.1754 \[hep-th\]](#).
- [122] P. Mastrolia, E. Mirabella, G. Ossola, T. Peraro, and H. van Deurzen, “The Integrand Reduction of One- and Two-Loop Scattering Amplitudes,” [arXiv:1209.5678 \[hep-ph\]](#). and references therein.
- [123] C. F. Berger, Z. Bern, L. J. Dixon, D. Forde, and D. A. Kosower, “On-shell unitarity bootstrap for QCD amplitudes,” *Nucl.Phys.Proc.Suppl.* **160** (2006) 261–270, [arXiv:hep-ph/0610089 \[hep-ph\]](#).
- [124] Z. Bern, L. J. Dixon, and D. A. Kosower, “On-Shell Methods in Perturbative QCD,” *Annals Phys.* **322** (2007) 1587–1634, [arXiv:0704.2798 \[hep-ph\]](#).
- [125] R. K. Ellis, W. Giele, and Z. Kunszt, “A Numerical Unitarity Formalism for Evaluating One-Loop Amplitudes,” *JHEP* **0803** (2008) 003, [arXiv:0708.2398 \[hep-ph\]](#). and references therein.
- [126] T. Binoth, J. P. Guillet, G. Heinrich, E. Pilon, and C. Schubert, “An Algebraic/numerical formalism for one-loop multi-leg amplitudes,” *JHEP* **0510** (2005) 015, [arXiv:hep-ph/0504267 \[hep-ph\]](#).
- [127] V. Hirschi, R. Frederix, S. Frixione, M. V. Garzelli, F. Maltoni, *et al.*, “Automation of one-loop QCD corrections,” *JHEP* **1105** (2011) 044, [arXiv:1103.0621 \[hep-ph\]](#). and references therein.
- [128] G. Cullen, N. Greiner, G. Heinrich, G. Luisoni, P. Mastrolia, *et al.*, “Automated One-Loop Calculations with GoSam,” *Eur.Phys.J.* **C72** (2012) 1889, [arXiv:1111.2034 \[hep-ph\]](#).

- [129] Z. Bern, K. Ozeren, L. J. Dixon, S. Hoeche, F. F. Cordero, *et al.*, “High multiplicity processes at NLO with BlackHat and Sherpa,” [arXiv:1210.6684 \[hep-ph\]](#).
- [130] M. Rodgers, *Automation of one-loop corrections for multi-particle processes*. Ph.d. thesis, University of Durham.
- [131] L. J. Dixon, “Calculating scattering amplitudes efficiently,” [arXiv:hep-ph/9601359 \[hep-ph\]](#).
- [132] Z. Bern, L. J. Dixon, and D. A. Kosower, “One loop amplitudes for $e^+ e^-$ to four partons,” *Nucl.Phys.* **B513** (1998) 3–86, [arXiv:hep-ph/9708239 \[hep-ph\]](#).
- [133] Z. Bern, A. De Freitas, and L. J. Dixon, “Two loop amplitudes for gluon fusion into two photons,” *JHEP* **0109** (2001) 037, [arXiv:hep-ph/0109078 \[hep-ph\]](#).
- [134] L. Lewin, *Polylogarithms and Associated Functions*. North-Holland, 1981.
- [135] L. Landau, “On analytic properties of vertex parts in quantum field theory,” *Nucl.Phys.* **13** (1959) 181–192.
- [136] R. J. Eden *et al.*, *The Analytic S-Matrix*. Cambridge University Press, UK, 2002.
- [137] C. Itzykson and J. B. Zuber, *Quantum Field Theory*. Dover Publications, Inc., N.Y., 2005.
- [138] G. F. Sterman, “Partons, factorization and resummation, TASI 95,” [arXiv:hep-ph/9606312 \[hep-ph\]](#).
- [139] S. Dittmaier, “Separation of soft and collinear singularities from one loop N point integrals,” *Nucl.Phys.* **B675** (2003) 447–466, [arXiv:hep-ph/0308246 \[hep-ph\]](#).
- [140] J. Collins, *Renormalization*. Cambridge University Press, UK, 1986.

- [141] G. Duplancic and B. Nizic, “Dimensionally regulated one loop box scalar integrals with massless internal lines,” *Eur.Phys.J.* **C20** (2001) 357–370, [arXiv:hep-ph/0006249](#) [hep-ph].
- [142] S. L. Adler, “Axial vector vertex in spinor electrodynamics,” *Phys.Rev.* **177** (1969) 2426–2438.
- [143] J. Bell and R. Jackiw, “A PCAC puzzle: $\pi_0 \rightarrow \gamma\gamma$; in the sigma model,” *Nuovo Cim.* **A60** (1969) 47–61.
- [144] L. Landau, “On the angular momentum of a two-photon system,” *Dokl.Akad.Nauk Ser.Fiz.* **60** (1948) 207–209.
- [145] C.-N. Yang, “Selection Rules for the Dematerialization of a Particle Into Two Photons,” *Phys.Rev.* **77** (1950) 242–245.
- [146] F. Jegerlehner, “Facts of life with gamma(5),” *Eur.Phys.J.* **C18** (2001) 673–679, [arXiv:hep-th/0005255](#) [hep-th].
- [147] G. ’t Hooft and M. Veltman, “Regularization and Renormalization of Gauge Fields,” *Nucl.Phys.* **B44** (1972) 189–213.